WISC

UNIVERSITY OF WISCONSIN • MADISON, WISCONSIN

PLASMA PHYSICS

45
2-8-96 PSC(2)

MAGNETOHYDRODYNAMIC SIMULATIONS OF NONINDUCTIVE HELICITY INJECTION IN THE REVERSED-FIELD PINCH AND TOKAMAK

Carl R. Sovinec

DOE/ER/53212-270

November 1995

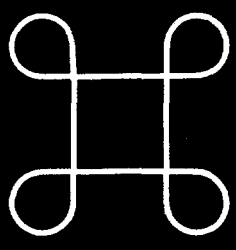

ONSIN

NOTICE

Printed in the United States of America
Available from
National Technical Information Service
U.S. Department of Commerce
5285 Port Royal Road
Springfield, VA 22161

NTIS Price codes
Printed copy: A06
Microfiche copy: A01

MAGNETOHYDRODYNAMIC SIMULATIONS OF NONINDUCTIVE HELICITY INJECTION IN THE REVERSED-FIELD PINCH AND TOKAMAK

by

Carl R. Sovinec

A dissertation submitted in partial fulfillment
of the requirements for the degree of

Doctor of Philosophy
(Physics)

at the

UNIVERSITY OF WISCONSIN-MADISON

1995

MAGNETOHYDRODYNAMIC SIMULATIONS OF NONINDUCTIVE HELICITY INJECTION IN THE REVERSED-FIELD PINCH AND TOKAMAK

Carl R. Sovinec

Under the supervision of Professor Stewart C. Prager

At the University of Wisconsin-Madison

ABSTRACT

Numerical computation is used to investigate resistive magnetohydrodynamic (MHD) fluctuations in the reversed-field pinch (RFP) and in tokamak-like configurations driven solely by direct current (DC) helicity injection. A Lundquist number (S) scan of RFP turbulence without plasma pressure produces the weak scaling of $S^{-0.18}$ for the root-mean-square magnetic fluctuation level for $2.5\times10^3 \le S \le 4\times10^4$. The temporal behavior of fluctuations and the reversal parameter becomes more regular as S is increased, acquiring a 'sawtooth' shape at the largest value of S. Simulations with plasma pressure and anisotropic thermal conduction demonstrate energy transport resulting from parallel heat fluctuations.

To investigate means of improving RFP energy confinement, three forms of current profile modification are tested. Radio frequency (RF) current drive is modeled with an auxiliary electron force, and linear stability calculations are used

to optimize parameters. Nonlinear simulations show that the magnetic fluctuation energy of internally resonant modes can be reduced by two or more orders of magnitude. The effective thermal diffusivity is locally reduced with the fluctuation energy, and global energy confinement increases by a factor of three. Simulations of DC helicity injection in RFPs extend earlier results to larger values of S and larger aspect ratios. It is found that the geometry of the injection system is important for determining whether fluctuations are suppressed or sustained through nonlinear coupling. The last form of RFP current profile modification is the transient, pulsed poloidal current drive (PPCD) technique. A simulation shows fluctuation suppression that is comparable to experimental observations on the Madison Symmetric Torus.

Simulations of DC helicity injection in tokamaks demonstrate net axial current without loop voltage and poloidal flux amplification resulting from an MHD dynamo. Hollow current profiles are generated self-consistently with a simplified axisymmetric injector configuration, and the current gradient leads to resistive instabilities that saturate at 1% of the axial magnetic field. An S-scan from 2.5×10^3 to 2×10^4 shows that the relaxation and fluctuation level increase with S in this range. A simple quasilinear power scaling is consistent with these results at low S and suggests that at larger S, the fluctuation level decreases.

ACKNOWLEDGMENTS

I would like to thank my advisor, Stewart Prager, for his guidance over the past four years. He has a genuine 'open door' policy that sets a fine example for all of us. I also want to express my sincere appreciation for his tireless efforts in Washington, which have played a crucial role in the battle for saving the U. S. magnetic fusion program.

I thank my committee members, Professors Clint Sprott and Donald Cox, and in particular, Professors Jim Callen and Paul Terry, for their careful review of my dissertation. I have also taken classes from my 'readers,' and I learned a great deal of plasma physics from them.

The research I have done here did not begin from 'scratch,' and I am grateful for the tremendous boost provided by Dalton Schnack, Bill Ho and Zoran Mikic of Science Applications International Corporation. They generously provided me with the DEBS code, the graphics post-processor, and lots of needed assistance. Along similar lines, I want to thank Chris Hegna for helping me understand the linear theory of resistive tearing modes.

I want to thank all who have been members of the MST group while I have been here at the University of Wisconsin. There is an uncommon spirit that is cooperative and enthusiastic. It is the most important element of our success, and I hope to take some of that spirit with me. I also want to acknowledge my plasma physics discussion pals: Miodrag Cekic, Brett Chapman, Gennady Fiksel, Hantao Ji, John Sarff, Matt Stoneking, and Andrew Ware. Our many conversations have been an important part of my education. In addition, I am very happy to have had the chance to work with a rising physics star, Pete Figliozzi, while he visited as a summer fellowship student.

Essential computer assistance has come from Larry Smith and Paul Wilhite; I appreciate their time and patience. Also, I owe many thanks to our wonderful secretary, Kay Shatrawka. In my opinion, she is the glue that holds our group together.

One last professional note: this work has been supported by the U. S. Department of Energy.

On the personal side, I want to express my thanks to our parents, Joyce and Richard Vigil and Cathleen and Richard Sovinec. Their love and support has provided stability during the difficult times. Friends are a critical ingredient, too. We could not have kept our sanity without the laughter we have had with our good friends, Jon and Darlene Henry and John and Jenny Petro.

Finally, and most important of all, I wish to thank my wife, Dawn. Those of us who have been married while in graduate school know how many sacrifices are asked of spouses. Dawn's contributions to my success have been galactic in proportion, and I appreciate every bit.

TABLE OF CONTENTS

1. INTRODUCTION

In recent years, magnetically confined plasmas produced in the conventional tokamak configuration have approached fusion reactor conditions, and the first experimental reactors will likely be tokamaks. However, the large toroidal magnetic field implies large construction and maintenance costs, which hamper economic competitiveness for commercial applications. Other magnetic configurations have relatively small fields, which may lead to a more practical reactor design. The reversed-field pinch (RFP) is among this group. With smaller fields, the discharge is more susceptible to relaxation via fluid-like motions. This relaxation is an inherent feature of ordinary RFPs. It permits reliable operation and is worth study on a scientific basis. However, the associated magnetic turbulence reduces particle and energy confinement, which are critical for achieving fusion conditions.

The issue of steady-state current drive is also important for fusion reactors, and it has not been settled for any toroidal configuration. Recent experiments have investigated an electrostatic approach for tokamaks, which is based on the same type of relaxation as that observed in RFPs (see Ono, 1987; Darrow, 1990; and Nelson, 1994). If this concept is successful, it will be a major advance towards the fusion reactor goal.

In this dissertation, I describe numerical simulations that investigate relaxation in RFPs and in tokamak configurations driven by an electrostatic potential. My objective for the RFP study is to demonstrate practical methods for improving confinement. The tokamak study is more basic; relaxation with this form of current drive has not been previously studied from first principles. 'Helicity injection' refers to a popular method of analysis for plasmas subject to relaxation. It is based on an energy minimization principle that has been adapted to describe continuous

operation. Magnetic helicity (defined below) is a constraint on the minimization, and this constraint becomes a balance for rates of helicity dissipation and injection in the steady-state description. RFPs and electrostatically-driven configurations are often analyzed in this context, so I devote the first section of this chapter to a brief review of helicity and helicity injection. Some of my results show that the helicity rate balance is not an adequate description, so I shall return to this topic while discussing simulation results and in the concluding chapter.

1.1 Magnetic Helicity and Helicity Injection

The notion of magnetic helicity as a useful concept for plasma physics probably originated with an astrophysical paper by Woltjer in the late 1950s (Woltjer, 1958). The objective of the paper is to justify a then frequently-assumed class of magnetohydrodynamic (MHD) equilibria where the current density is proportional to the magnetic field with a uniform constant of proportionality throughout ($\mathbf{J}=\lambda\mathbf{B}$). Woltjer found that the volume integral $\int \mathbf{A}\cdot\mathbf{B}d\mathbf{x}$, where $\mathbf{A}$ is the vector potential, is a conserved quantity in perfectly conducting plasmas within closed conducting containers. He used this as an invariant while minimizing the magnetic energy to find the state with the lowest possible potential energy. This results in the desired configuration, and the invariant integral later became known as magnetic helicity. In physical terms it is a measure of the linkage of magnetic flux tubes in a given configuration (Turner, 1987). The significance of the minimization principle lies in the stability properties of the resulting equilibrium. It has been shown that under certain conditions, this minimization implies a necessary and sufficient condition for stability to ideal, i.e. nonresistive, MHD perturbations (Finn, 1981). In general, it is sufficient but not necessary for ideal stability within a conducting container.

While Woltjer's result foreshadowed another significant and popular hypothesis, it is incomplete. An ideal conducting fluid conserves helicity not only globally but also locally for each and every flux tube (Taylor, 1974). Thus, the relaxation of a given initial magnetic field configuration is subject to not one but an infinite number of constraints. This fact was recognized by Kruskal and Kulsrud, although they did not address magnetic helicity directly (Kruskal, 1958). The impasse was broken by Taylor when he hypothesized that a small amount of resistivity will relax the constraint on individual flux tubes, while leaving intact the constraint for the entire volume (Taylor, 1974). If this hypothesis is correct, it substantiates Woltjer's approach when applied to the problem of magnetic field relaxation in resistive plasmas.

The Taylor hypothesis gained a large degree of popularity among researchers studying the RFP, as it produced the first quantitative model for field reversal. However, the toroidal containers that surround RFPs are not closed, and the magnetic helicity defined above is not gauge-invariant (Reiman, 1980). A conducting chamber requires a poloidal slice (at constant toroidal angle) in order to apply toroidal electric field for current drive. The slice effectively renders the torus into a bent cylinder with two ends, and it may be shown that the original helicity definition is not gauge invariant whenever magnetic field penetrates the surface of the container. The difficulty for normal toroidal configurations, where magnetic field only pierces the ends of the bent cylinder, is avoided with the relative helicity defined by Bevir and Gray (Bevir, 1981),

$$K = \int \mathbf{A}\cdot\mathbf{B}d\mathbf{x} - \oint A_\theta d\theta \oint A_z dz \,. \qquad (1.1)$$

The second term of this equation subtracts the linkage of the toroidal flux within the torus and the poloidal flux that passes externally through the center of the 'doughnut hole.' A more general definition that is suitable for arbitrarily shaped fields and containers is

$$K = \int \mathbf{A}\cdot\mathbf{B}d\mathbf{x} - \int \mathbf{A}_v\cdot\mathbf{B}_v d\mathbf{x} \,, \qquad (1.2)$$

where the 'v' subscripts denote vacuum fields. Inside the container, $\nabla\times\mathbf{B}_v = 0$, and at the surface, the normal components of $\mathbf{B}_v$ and $\mathbf{B}$ are the same for all time (Berger and Field, 1984 and Jensen and Chu, 1984). The second term subtracts any linkage between internal and external fields.

The relative helicity defined by Eq. 1.2 conveniently leads to the idea of helicity injection. Upon application of a temporal derivative and the use of Faraday's law, Eq. 1.2 becomes (Jarboe, 1994)

$$\frac{dK}{dt} = -2\int \mathbf{E}\cdot\mathbf{B}\,d\mathbf{x} + 2\int \mathbf{E}_v\cdot\mathbf{B}_v\,d\mathbf{x} \,. \qquad (1.3)$$

For the parallel component of electric field, Ohm's law gives $E_\parallel = \eta J_\parallel$, where η is the plasma resistivity; thus, helicity dissipation results from the first term on the right side of Eq. 1.3. To maintain a steady state then requires the injection of helicity through the second term.

The helicity injection term can be put into practical forms for ordinary inductive drive and for electrostatic injection. The inductive relation is derived assuming that the configuration is in steady-state and that the magnetic field is independent of toroidal angle (ϕ). The integration over this direction, $2\oint \mathbf{E}_v\cdot\mathbf{B}_v R d\phi$, is then $2V_l B_Z(r,\theta)$ for any poloidal position, where V_l is the toroidal 'loop' voltage. When

the poloidal integrations are carried out, the result is $2V_l\Phi$, with Φ being the toroidal flux. Other configurations allow the application of electrostatic fields parallel to magnetic field. In these cases, $\mathbf{E}_v = -\nabla\chi$, where χ is the electrostatic potential. Gauss' law gives $-2\int \mathbf{B}_v \cdot \nabla\chi d\mathbf{x} = -2\int \nabla\cdot(\chi\mathbf{B}_v)d\mathbf{x}$ or $-2\int \chi\mathbf{B}\cdot\mathbf{n}dS$ after using the divergence theorem. Configurations such as spheromaks have used this form of helicity injection for decades (see Jarboe, 1994, for a review).

The dissipation of helicity from a small amount of resistivity provides support for Taylor's hypothesis. As Taylor himself points out in a later paper (Taylor, 1986), the decay of helicity and the decay of magnetic energy may be compared after transforming to spatial eigenfunctions. Ignoring any possible injection,

$$\frac{dK}{dt} \sim -2\eta\sum_n k_n B_n^2 \text{ , and}$$

$$\frac{dW}{dt} \sim -\eta\sum_n k_n^2 B_n^2 ,$$

where W is the magnetic energy, and B_n and k_nB_n are the transformed components of magnetic field and current density, respectively. At wavenumbers (k_n) of order $\eta^{-1/2}$, the magnetic energy dissipation rate is of order unity while the helicity decay rate is of order $\eta^{1/2}$—small when η is very small. Thus, fine-scale relaxation tends to dissipate magnetic energy at a larger rate than helicity. However, for driven/damped systems considered over time scales on the order of the global energy and helicity turnover rates, relaxation arguments are not appropriate.

1.2 Reversed-field Pinch and Tokamak

The RFP and tokamak are toroidal magnetic configurations, and the difference between them lies primarily in the magnitude of the toroidal field component. In the RFP, the small toroidal component allows plasma current to shear the field in the azimuthal direction, so that it is purely azimuthal at the point denoted the reversal surface. Between this point and the wall, the direction of the axial component is reversed. In contrast, the large toroidal component in the tokamak shears the field in the opposite direction. These features are evident in the comparison of typical safety factor profiles shown in Fig. 1.1. The safety factor is the number of toroidal passes that a magnetic field line makes within the torus for each poloidal pass that it completes. Using a geometric approximation where the torus is treated as a periodic cylinder, the safety factor reduces to $q(r)=rB_z(r)/RB\theta(r)$ (R is the axial period length over 2π). [Fundamentals for the RFP and tokamak are reviewed in Bodin, 1980 and Mukhovatov, 1971, respectively.]

MHD dynamics in the two configurations are remarkably different. Potentially unstable MHD modes arise at resonance surfaces where the perturbation does not bend the equilibrium field and thereby avoids a restoring force. Using the periodic cylinder approximation allows a Fourier series representation:

$$f(r,\theta,z) = \sum_{m,n} f_{m,n}(r)e^{-i(m\theta+nz/R)} , \qquad (1.4)$$

where $f_{-m,-n}(r) = f^*_{m,n}(r)$, and the resonance surface (r_s) for a particular mode occurs where $q(r_s)=-m/n$. In general, as the poloidal mode number, m, is increased, ideal perturbations become more stable (Newcomb, 1960). Therefore, the most dangerous modes are usually those with small m-numbers. [Localized 'ballooning' modes in tokamaks are an exception that result from toroidal effects.]

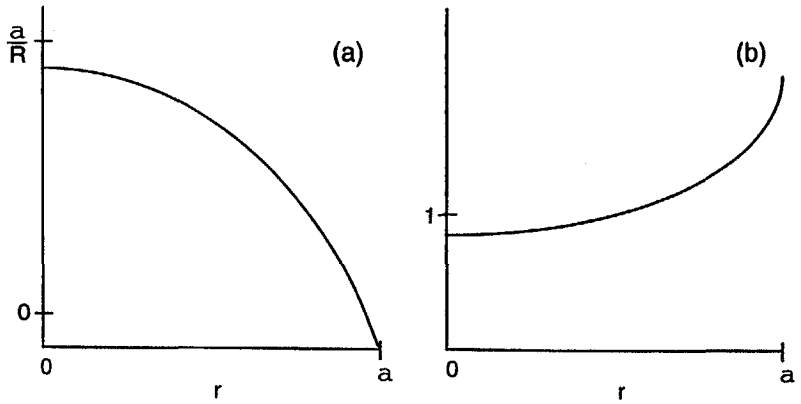

Figure 1.1. Typical safety factor profiles for the RFP (a) and the tokamak (b).

The tokamak has a rather limited number of resonant, low-m modes in comparison with the RFP, which has an infinite number of modes accumulating near the reversal surface (Caramana, 1983). Though some of the RFP modes are unstable, many are not, and nonlinear interactions help prevent disruption (Schnack, 1985). Unfortunately, RFP fluctuations are large enough to make the magnetic field stochastic over much of the plasma volume, so particles and thermal energy easily leak towards the wall. Modern tokamaks do not suffer from large magnetic fluctuation levels, but isolated MHD activity can detract from confinement and may even lead to major disruption.

Where possible, I compare RFP results with the Madison Symmetric Torus (MST—Prager, 1990). The device is a large RFP with a minor radius of 0.52 m and a major radius of 1.5 m. Typical plasma conditions are temperatures of 250 eV and particle densities on the order of 1×10^{19} m^{-3}. The magnetic inductance is

approximately 0.1 T, and current densities range from 125 to 600 kA. Many of the topics discussed here have been investigated to support this experimental effort.

1.3 Preview

The unifying theme of this research is the investigation of noninductive helicity injection in RFPs and tokamaks through MHD simulation. For the RFP, the objective is to improve energy confinement by modifying the parallel current profile to reduce the magnetic fluctuation level. Simulations are used to investigate three approaches. In the first approach, a generic form of helicity injection is applied directly to the mean current to capture the MHD impact of radio-frequency (RF) current drive (Uchimoto, 1994). Results from three forms of modeling are reported: 1) A linear eigenvalue analysis (following the work of Robinson, 1978) is used to optimize current drive profiles. 2) Nonlinear, pressureless MHD simulations show that the region of stochastic magnetic field can be reduced without complete stabilization. 3) Nonlinear simulations with self-consistently modeled pressure and anisotropic thermal conduction demonstrate reduced thermal energy transport.

The second approach is direct current (DC) helicity injection as envisioned by Jensen and Chu (Jensen, 1984). An initial investigation of this concept was conducted by Ho for two injector configurations in small aspect ratio (R/a), low Lundquist number (S) simulations (Ho, 1991). Here the study is extended to larger R/a and S and to other geometries. It is determined that non-axisymmetric systems tend to produce harmful couplings with the resonant modes. A new injector geometry, based on the findings, is proposed and tested.

The final approach is the pulsed poloidal current drive (PPCD) technique, which has been investigated in MST experiments (Sarff, 1994). This is not a form of helicity injection, but the current profile modification is similar though transient. It

provides existing experiments with a method of testing the impact of noninductive helicity injection without hardware modifications. Nonlinear MHD simulations presented here do indeed show beneficial effects on the fluctuation level as the pulse propagates across the cylinder radius. These numerical results compare favorably with experimental results.

Helicity injection in tokamaks is intended to serve the purpose of toroidal current drive. The concept is currently under experimental investigation in the Current Drive Experiment (CDX) at Princeton University (Ono, 1987), the Continuous Current Tokamak at the University of California, Los Angeles (Darrow, 1990) and the Helicity Injected Tokamak at the University of Washington (Nelson, 1994). The MHD simulations presented here are the first solutions from basic equations for this concept. An axisymmetric injection system, similar to the HIT configuration, is modeled in a periodic cylinder. The simulations reproduce the important experimental features of axial (toroidal) current without 'loop' voltage and poloidal flux amplification resulting from an MHD dynamo. However, the current profile relaxation is weak, and the magnetic fluctuation level is large.

This work is organized in the following manner: Chapter 2 is devoted to describing the two numerical tools that are used throughout. Chapter 3 presents information on MHD activity in RFPs, including a review of power flow, modeling of energy transport, and a pressureless Lundquist number scaling of the fluctuation level. Chapter 4 addresses the helicity injection concept for RFPs, covering the approaches discussed above. The tokamak injection study is presented in Chapter 5, and Chapter 6 provides a summary and concluding remarks.

References

M. A. Berger and G. B. Field, "The Topological Properties of Magnetic Helicity," J. Fluid Mech. **147**, 133 (1984).

M. K. Bevir and J. W. Gray, "Relaxation, Flux Consumption and Quasi Steady State Pinches," in *Proceedings of Reversed Field Pinch Theory Workshop*, Los Alamos National Laboratory Report, LA 8944-C (1981).

H. A. B. Bodin and A. A. Newton, "Reversed-field Pinch Research," Nucl. Fusion **20**, 1225 (1980).

E. J. Caramana, R. A. Nebel, and D. D. Schnack, "Nonlinear, Single-helicity Magnetic Reconnection in the Reversed-field Pinch," Phys. Fluids **26**, 1305 (1983).

D. S. Darrow, M. Ono, C. B. Forest, G. J. Greene, Y. S. Hwang, H. K. Park, R. J. Taylor, P. A. Pribyl, J. D. Evans, K F. Lai, and J. R. Liberati, "Properties of DC Helicity Injected Tokamak Plasmas," Phys. Fluids B **2**, 1415 (1990).

J. M. Finn and W. M. Manheimer, "Spheromak Tilting Instability in Cylindrical Geometry," Phys. Fluids **24**, 1336 (1981).

Y. L. Ho, "Numerical Simulation of Fluctuation Suppression via DC Helicity Injection in a Reversed-field Pinch," Nucl. Fusion **31**, 341 (1991).

T. R. Jarboe, "Review of Spheromak Research," Plasma Phys. Control. Fusion **36**, 945 (1994).

T. H. Jensen and M. S. Chu, "Current Drive and Helicity Injection," Phys. Fluids **27**, 2881 (1984).

M. D. Kruskal and R. M. Kulsrud, "Equilibrium of a Magnetically Confined Plasma in a Toroid," Phys. Fluids **1**, 265 (1958).

V. S. Mukhovatov and V. D. Shafranov, "Plasma Equilibrium in a Tokamak," Nucl. Fusion **11**, 605 (1971).

B. A. Nelson, T. R. Jarboe, D. J. Orvis, L. A. McCullough, J. Xie, C. Zhang, and L. Zhou, "Formation and Sustainment of a 150 kA Tokamak by Coaxial Helicity Injection," Phys. Rev. Lett. **72**, 3666 (1994).

W. A. Newcomb, "Hydromagnetic Stability of a Diffuse Linear Pinch," Ann. Phys. **10**, 232 (1960).

M. Ono, G. J. Greene, D. Darrow, C. Forest, H. Park, and T. H. Stix, "Steady-state Tokamak Discharge via DC Helicity Injection," Phys. Rev. Lett. **59**, 2165 (1987).

S. C. Prager, A. F. Almagri, S. Assadi, J. A. Beckstead, R. N. Dexter, D. J. Den Hartog, G. Chartas, S. A. Hokin, T. W. Lovell, T. D. Rempel, J. S. Sarff, W. Shen, C. W. Spragins, and J. C. Sprott, "First Results from the Madison Symmetric Torus Reversed Field Pinch," Phys. Fluids B **2**, 1367 (1990).

A. Reiman, "Minimum Energy State of a Toroidal Discharge," Phys. Fluids **23**, 230 (1980).

D. C. Robinson, "Tearing-mode-stable Diffuse-pinch Configurations," Nucl. Fusion **18**, 939 (1978).

J. S. Sarff, S. A. Hokin, H. Ji, S. C. Prager, and C. R. Sovinec, "Fluctuation and Transport Reduction in a Reversed-field Pinch by Inductive Poloidal Current Drive," Phys. Rev. Lett. **72**, 3670 (1994).

D. D. Schnack, E. J. Caramana, and R. A. Nebel, "Three-dimensional Magnetohydrodynamic Studies of the Reversed-field Pinch," Phys. Fluids **28**, 321 (1985).

J. B. Taylor, "Relaxation of Toroidal Plasma and Generation of Reverse Magnetic Fields," Phys. Rev. Lett. **33**, 1139 (1974).

J. B. Taylor, "Relaxation and Magnetic Reconnection in Plasmas," Rev. Mod. Phys. **58**, 741 (1986).

L. Turner, "Magnetic Helicity for Pedestrians," Los Alamos National Laboratory Report LA-UR 87-996 (1987).

E. Uchimoto, M. Cekic, R. W. Harvey, C. Litwin, S. C. Prager, J. S. Sarff, and C. R. Sovinec, "Lower-hybrid Poloidal Current Drive for Fluctuation Reduction in a Reversed-field Pinch," Phys. Plasmas **1**, 3517 (1994).

L. Woltjer, "A Theorem on Force-free Magnetic Fields," Proc. Nat. Acad. Sci. **44**, 489 (1958).

2. NUMERICAL TOOLS

Modeling a plasma with the MHD equations treats the plasma as a single, conducting fluid. This approach is strictly valid when electron inertia, kinetic effects, particle orbit effects, and high frequency phenomena are not important (Krall, 1986), but it is often applied to plasmas where these conditions are not satisfied. The philosophy behind the MHD studies presented here is not to provide a comprehensive model for all phenomena in the RFP and tokamak. Rather, it is to examine one class of phenomena—long wavelength, low frequency modes, which are important in both devices and are well-described by the equations of MHD. When plasma pressure is small, the equations in MKS units are

$$\frac{\partial \rho}{\partial t} + \nabla \cdot (\rho \mathbf{V}) = 0 \tag{2.1}$$

$$\rho \frac{\partial \mathbf{V}}{\partial t} + \rho \mathbf{V} \cdot \nabla \mathbf{V} = \mathbf{J} \times \mathbf{B} \tag{2.2}$$

$$\mathbf{E} = -\mathbf{V} \times \mathbf{B} + \eta \mathbf{J} \tag{2.3}$$

$$\mathbf{J} = \frac{1}{\mu_0} \nabla \times \mathbf{B}, \tag{2.4}$$

where $\mathbf{V}$ is the fluid velocity, and ρ is the mass density. Equation 2.1 is a statement of mass continuity, Eq. 2.2 is Newton's law with a Lorentz force, Eq. 2.3 is the generalized Ohm's law, and Eq. 2.4 is Ampere's law in the absence of displacement current.

In both the RFP and the tokamak, MHD activity is usually characterized as small perturbations or fluctuations about an equilibrium configuration. The activity is then

classified as nonlinear or linear depending on the significance of interactions among the perturbations. In all of the topics addressed here, nonlinear interactions are important. To obtain numerical solutions for the nonlinear MHD system, the 3-dimensional DEBS code is used; it is described in Section 2.1. To discern the impact of current profile modification on the linear stability of the fluctuations, a linear eigenvalue approach is used. This approach is embodied in the RESTER code, which is described in Section 2.2.

2.1 DEBS

The DEBS code solves initial value problems with a prescribed set of boundary conditions in the geometry of a periodic cylinder (Schnack, 1987). The algorithm uses the pseudo-spectral approach, where linear operators such as spatial and temporal derivatives are treated in the Fourier representation of Eq. 1.4. Nonlinear products, such as the Lorentz force in the momentum equation, are generated with a discrete representation of physical space to avoid summing over a large number of modes. An efficient Fast Fourier Transform (FFT) translates from the physical space representation to the Fourier space representation and vice versa. A discrete mesh is also used for the radial dependencies; radial derivatives are approximated by finite differences.

DEBS has been applied to many different nonlinear plasma problems over the past decade, and users constantly modify the algorithms and equations as new applications or new phenomena are studied. Presently, there are several distinct codes. Among them is a pressureless code that I have used for most of the DC helicity injection studies and all of the PPCD simulations. The version with which I started was previously modified by Yung-Lung Ho to model a resistive wall (Ho, 1991a) and DC helicity injection (Ho, 1991b). The essential aspects of DEBS and

the DC helicity injection boundary conditions are described in Section 2.1.1. Some results from a typical RFP simulation are also presented. [Additional details on the boundary conditions for all situations are discussed in the later chapters with the simulation results.]

To make high-S simulations practical, I modified the pressureless code to include hyper-dissipation terms in both Ohm's law and the momentum equation. These modifications and their numerical properties are discussed in Section 2.1.2. Along a separate line of development, Dalton Schnack implemented finite-pressure effects including anisotropic thermal conduction. This finite-pressure code is distinct from Ho's code and my version with hyper-dissipation. I have used the finite-pressure code to produce quantitative information on thermal energy transport in RFPs with and without current profile modification. During the course of that research, I further developed the thermal conduction algorithm to improve its accuracy. The pressure equation and the numerical properties of the new thermal conduction algorithm are described in Section 2.1.3.

2.1.1 Pressureless Code

The basic pressureless version of the code solves two coupled, partial differential equations, the momentum equation and Ohm's law. In the code's units, they are

$$(1-\alpha\Delta t\nabla^2)\frac{\partial \mathbf{V}}{\partial t} = -S\mathbf{V}\cdot\nabla\mathbf{V} + S\mathbf{J}\times\mathbf{B} + \upsilon\nabla^2\mathbf{V} \tag{2.5}$$

$$\frac{\partial \mathbf{A}}{\partial t} = -\mathbf{E} = S\mathbf{V}\times\mathbf{B} - \eta\mathbf{J}, \tag{2.6}$$

where the following normalizations have been applied: Resistivity is normalized by η_0/μ_0, the diffusivity at the cylinder axis. Lengths are normalized by the cylinder radius, a. Time is in units of the resistive diffusion time, $\tau_r=\mu_0 a^2/\eta_0$. The magnetic field is normalized by a reference magnitude, B_0, and the velocity is in units of the Alfven speed, $v_a=B_0/(\mu_0\rho)^{1/2}$. The constant preceding each nonlinear term is the Lundquist number, $S=\tau_r/\tau_a$, where $\tau_a=a/v_a$ is the Alfven time. After initiation with an equilibrium configuration, temporal behavior is determined by advancing the equations in discrete time-steps. The marching is done with a leapfrog method, where the discrete representations of **A** and **V** are staggered by half of the temporal increment ($\Delta t/2$). The viscous and resistive dissipation terms are linear in Fourier space, and they are evaluated at the new time step (fully implicit). Nonlinear terms are evaluated explicitly, though **V** in the advective force and **B** in the ideal electric field are predicted with an additional numerical step. Note that a gauge choice is made in Eq. 2.6 such that the scalar potential vanishes everywhere.

The code does not evolve density and assumes it is a uniform constant. Compressible flow is allowed, however, and this seems to be more significant for the RFP (Aydemir, 1985) than it is for the tokamak (Charlton, 1990). The omission of density evolution implies that particle transport is not calculated, and the radial distribution of the local Alfven speed may not be accurate. This is not expected to have a major impact on the results.

There are two terms in Eq. 2.5 that are not in the original momentum equation, Eq. 2.2. On the left side, the operator $\alpha\Delta t\nabla^2$ acts on the temporal derivative of the velocity. This is a semi-implicit term designed to allow time-steps that are long compared to the time that it takes for Alfven waves to cross a computational cell (Harned, 1985 and Schnack, 1987). The term effectively adds a wavenumber-

dependent inertia to the fluid and slows the propagation of the large wavenumber waves. The emphasis here is on resistive fluctuations that act on a hybrid time-scale between τ_r and τ_a. The constant α and the time-step are chosen such that the semi-implicit term has little effect on resistive modes. In fact, for all but the smallest spatial scales, Alfven waves are also modeled accurately.

On the right side of Eq. 2.5, an isotropic viscous term has also been added for numerical purposes. The leapfrog scheme introduces dispersive errors but not dissipative errors for linear waves, and it requires some viscosity to keep nonlinear waves numerically stable (Anderson, 1984). The magnitude of the normalized viscosity that is used ($\upsilon \cong 1$) is typically larger than realistic values of cross-field viscosity coefficients (Sidikman, 1990). However, power dissipated by the viscous term is monitored and is usually much less than ohmic dissipation. If this is not the case, a detailed investigation is warranted.

The boundary conditions on the vector potential allow the DEBS code to simulate a wide variety of helicity injection schemes. For a normal RFP configuration, the temporal derivative of $\langle A_z \rangle$ at the wall (r=1 after normalization) applies an axial electric field to drive current, and the derivative of $\langle A_\theta(r=1) \rangle$ is zero to conserve axial flux. [The $\langle\ \rangle$ symbol indicates the (m=0, n=0) or 'mean' Fourier component, and small case letters are used to denote nonsymmetric components or modes.] For the PPCD simulations, a transient poloidal electric field is applied with nonzero $\langle E_\theta(r=1) \rangle = -\partial \langle A_\theta(r=1) \rangle / \partial t$. Simulations of tokamak helicity injection use the nonsymmetric components of **A** to apply a divertor field and an electrostatic potential at the plasma surface. This generates the electrostatic helicity injection, $-2\int \chi \mathbf{B} \cdot \mathbf{n} dS$, where χ is the electrostatic potential in the Coulomb gauge. For the RFP simulations with DC helicity injection, b_r and j_r are specified at the wall, and the latter indirectly enforces an electrostatic potential.

The plasma behavior is insensitive to the velocity boundary conditions when the resistivity near the wall is large. When such a profile is chosen, all components of **V**(r=1) are usually set to zero for RFP simulations. In fact, a sharply rising resistivity profile is not unrealistic. Impurities and wall fueling tend to make the exterior a relatively resistive region in RFP experiments. For these simulations, the normalized profile $\eta(r)=(1+9r^{30})^2$ is a common choice.

The tokamak helicity injection simulations require different boundary conditions. The applied electrostatic fields are mostly perpendicular to the magnetic field, and specifying j_r in these simulations produces unresolved gradients in **A**. Instead, electrostatic fields are applied directly through the nonsymmetric part of $\partial \mathbf{A}(r=1)/\partial t$. The resulting hollow current profiles are strongly dependent on the resistivity near the wall (see Section 5.3.2), and most cases have $\eta(r)=1$. Without large edge resistivity, the plasma is sensitive to the velocity boundary conditions. The radial and axial components of **V**(r=1) are set to the local $\mathbf{E}\times\mathbf{B}$ drift from the applied electric field and the local magnetic field. The azimuthal component is then adjusted so that $(\nabla \times \mathbf{V})_z = 0$. The radial and axial components prevent the formation of a surface current which would dominate other behavior, and the azimuthal part avoids a large viscous decay that is generated when all components are set to $\mathbf{E}\times\mathbf{B}$. This particular combination injects parallel current without inducing perpendicular surface current for the vertical **E** configuration described in Chapter 5. It may not be applicable to other field configurations.

A series of simulations is usually initiated as an equilibrium configuration with small amplitude perturbations. Equilibria without plasma pressure have current density that is strictly parallel to the magnetic field, $\langle \mathbf{J}(r) \rangle \times \langle \mathbf{B}(r) \rangle = 0$, and one may freely choose a 'parallel current' profile,

$$\lambda(r) = \frac{\langle \mathbf{J}(r) \rangle \cdot \langle \mathbf{B}(r) \rangle}{\langle B(r) \rangle^2}.$$

An additional choice of $\langle B_z(r=0) \rangle$ then determines the configuration. The azimuthal and axial components of Ampere's law (Eq. 2.4) form a set of coupled, first-order differential equations for $\langle B_\theta(r) \rangle$ and $\langle B_z(r) \rangle$, which are integrated from the origin to the wall with a simple numerical scheme. Two equilibria commonly used for initial conditions are the modified Bessel function model (MBFM—Johnson, 1981) and the paramagnetic equilibrium (Bickerton, 1958). In the MBFM, the λ-profile is flat from r=0 to some break point beyond which $\lambda(r)$ drops linearly to zero at r=1 (see Fig. 2.1a). In the paramagnetic equilibrium, a uniform axial electric field is assumed, and the magnitude of the current density is related to the electric field through the parallel component of Ohm's law:

$$\lambda(r) = \frac{\langle E_z \rangle \langle B_z(r) \rangle}{\eta(r) \langle B(r) \rangle^2}.$$

A typical $\lambda(r)$ profile for this model is shown in Fig. 2.1c. The resulting safety factor profiles for both models are also plotted in Fig. 2.1. The most significant difference is that the MBFM can produce the reversed field of an RFP near the wall (q<0), while the paramagnetic model can not. However, the MBFM is subject to resistive diffusion in the presence of nonzero resistivity.

A simulation run from the paramagnetic equilibrium in Fig. 2.1 demonstrates typical DEBS results. The aspect ratio (R/a) is three in this sample case, and the Lundquist number is 10^4. The simulation has 125 radial cells and resolves poloidal modes $0 \le m \le 2$ and axial modes $-42 \le n \le 42$. Figure. 2.2 shows the energy

histories for a selected group of modes. They grow linearly at very early times, and at t=0.01, the largest mode saturates. Over the next 0.04 τ_r, there is a transition to a turbulent, nonlinear state. The mean axial magnetic field at the wall reverses at t=0.02 τ_r, as evident in the time history of the reversal parameter

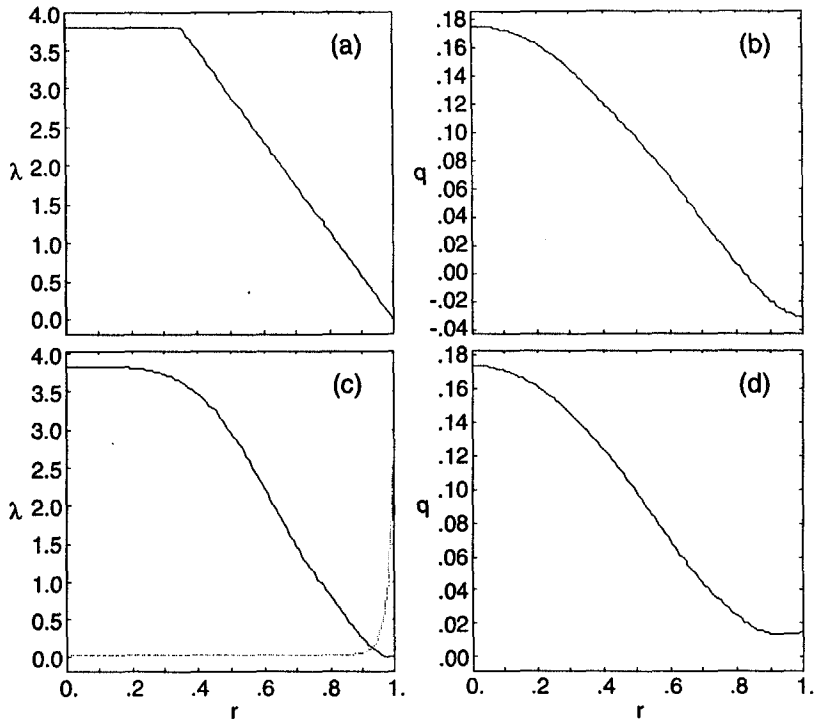

Figure 2.1 Equilibrium profiles of the MBFM (a) parallel current and (b) safety factor and of the paramagnetic equilibrium (c) parallel current and (d) safety factor. The dotted trace in (c) shows the shape of the resistivity profile. Parameters are chosen to produce profiles that are similar to RFP profiles.

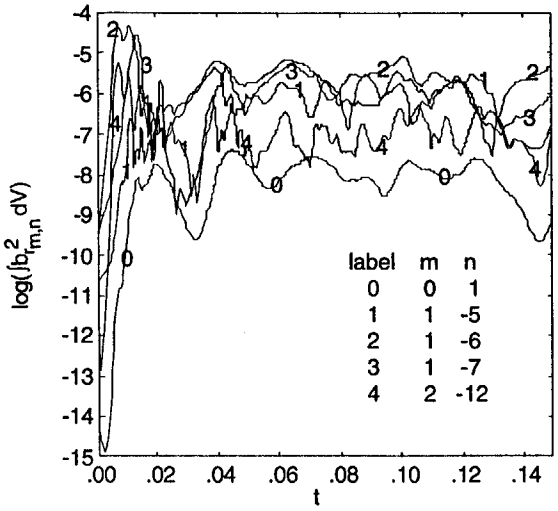

Figure 2.2 Time histories of modal magnetic energy (radial contributions only) for a selected group of modes from the sample RFP simulation. At t=0, the mean fields are the paramagnetic equilibrium shown in Fig. 2.1. The traces shown are missing a factor of 2^{10} due to a programming error.

($F = \pi\langle B_z(r=1)\rangle/\Phi$, where Φ is the axial magnetic flux), shown in Fig. 2.3a. The applied axial electric field is constant, and the net axial current varies only slightly (Fig 2.3b shows the pinch parameter $\Theta = I_z/2\Phi$ vs. time). The simulation is continued for an additional 0.15 τ_r to obtain time-averaged information on the quasi-steady configuration. The average parallel current and safety factor profiles are shown in Fig. 2.4, and the level of temporal fluctuation is shown by the dotted traces. The action of the MHD dynamo flattens the parallel current in the interior (compare Fig 2.1c and Fig 2.4a), and a reversed state is maintained (Fig. 2.4b). Details of the MHD dynamo are discussed in Chapter 3.

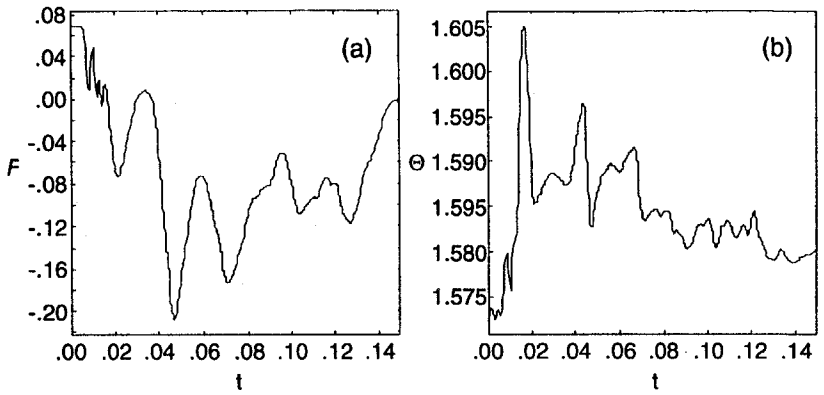

Figure 2.3 Time histories of (a) reversal parameter and (b) pinch parameter from the sample RFP simulation.

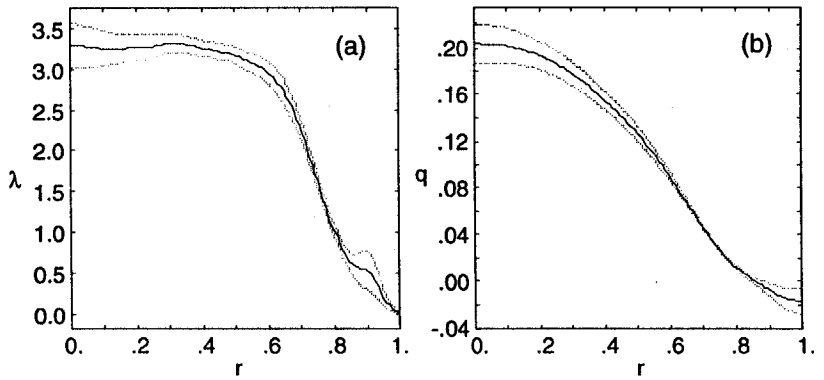

Figure 2.4 Radial profiles of (a) parallel current and (b) safety factor in the quasi-steady RFP state. The solid traces show the time average for 0.15≤t≤0.30, and the dotted lines indicate a standard deviation above and below the average. These results are from a continuation of the simulation shown in Figs. 2.2 and 2.3.

2.1.2 Hyper-dissipation

Since the leapfrog algorithm does not induce numerical dissipation, a simulation must have sufficient resolution so that all power is damped explicitly through terms in the equations. In the basic version of the code, the dissipation mechanisms are the resistive term in Eq. 2.6 and the viscous term in Eq. 2.5; they are faithful representations of the collisional dissipation that occurs in physical systems. The resolution requirements are not restrictive for S up to 10^4, where it is sufficient to divide the minor radius into 125 computational cells plus a 'ghost' cell on each side of the domain. However, increasing S (reducing dissipation) without increasing resolution leads to numerical aliasing errors on the radial grid as power attempts to flow into wavenumbers that are above the Nyquist 'frequency,' $\pi/\Delta r$ (Ferziger, 1983). In RFP simulations, the resolution requirements become prohibitive well below the experimental S-values of 10^6.

It has been observed that while the smallest-resolved scale lengths (largest wavenumbers) are necessary for numerical stability, they do not contribute significantly to global performance parameters such as reversal and average modal energy. RFPs tend to be dominated by a few large tearing modes, and as long as the resistive layers of these modes are adequately resolved, a simulation produces accurate results. A related numerical challenge in neutral-fluid turbulence modeling led to the use of hyper-viscosity (McWilliams, 1984). Hyper-viscosity produces dissipation that is proportional to the fourth power of wavenumber. It has little effect on small, physically important wavenumbers, while strongly damping large wavenumbers. Borrowing this idea to allow high-S computations, hyper-viscosity and hyper-resistivity have been added to Eqs. 2.5 and 2.6:

$$(1-\alpha\Delta t\nabla^2)\frac{\partial \mathbf{V}}{\partial t} = -S\mathbf{V}\cdot\nabla\mathbf{V} + S\mathbf{J}\times\mathbf{B} + \upsilon\nabla^2\mathbf{V} - \zeta(\Delta t,\Delta r)\nabla^4\mathbf{V} \tag{2.7}$$

$$\frac{\partial \mathbf{A}}{\partial t} = -\mathbf{E} = S\mathbf{V}\times\mathbf{B} - \eta\mathbf{J} - \zeta(\Delta t,\Delta r)\nabla\times\nabla\times\mathbf{J}. \tag{2.8}$$

The hyper-viscosity and hyper-resistivity are both represented by the same coefficient ζ. [Using separate coefficients has not yet been explored.] Its magnitude is parameterized by the time-step and the grid size, so that it decreases with increasing resolution to ensure consistency with the original equations.

The hyper-dissipation terms have been added to the DEBS code in a fully implicit scheme. This is similar to the implementation of the other dissipation terms, except the numerical stencil for the spatial operator covers five radial grid points instead of three. For each equation, the normal dissipation and the hyper-dissipation are both included in a single matrix that acts on the vector field at the new time-step. Thus, each equation still requires only one matrix inversion to advance to the next time-step. The additional operations add less than 20% to the per-cycle CPU time in comparison with simulations run without hyper-dissipation.

The approach is successful if a set of physical conditions can be accurately simulated with a net savings in CPU time. I have tested it with a series of RFP simulations that have varied amounts of resolution and hyper-dissipation. The simulations are similar to the one described in Section 2.1.1; however, the resistivity profile is flat, and the boundary condition on the mean flow is the $\langle\mathbf{E}\rangle\times\langle\mathbf{B}\rangle$ inward pinch from the applied electric field. [These are not typical choices for an RFP simulation, but there is little impact.] These simulations also have R/a=2, so that fewer axial modes ($-21\le n\le 21$) are needed.

Global results averaged over 0.2 τ_f of the quasi-steady state are presented in Table 2.1 for eight simulations. The first three have no hyper-dissipation but have

varied levels of temporal and spatial resolution. There is sufficient agreement to consider case A converged in both time and space. The next three simulations have half the spatial resolution of A with varied levels of hyper-dissipation. The root-mean-square (rms) magnetic fluctuation levels are all within 3% of case A, and the pinch parameters are within 0.4%. The average reversal parameters are within 8%. The larger discrepancy on F is not surprising, because the hyper-dissipation does affect the temporal behavior, and F oscillates by half its average value for these physical parameters. With different values of ζ, the 0.2 τ_r does not cover

Table 2.1. Time-averaged results from RFP simulations with and without hyper-dissipation. The reversal and pinch parameters also indicate the standard deviation of the temporal fluctuations. The time-step for all but case B is 0.1/S, and $\text{rms(b)} = \sqrt{2\sum_{m,n}\int_0^1 b_{m,n}^2 r dr}$.

case	ζ	Δr	F	Θ	rms(b)
A	0	8×10^{-3}	-0.095±0.049	1.625±0.005	0.0341
B[a]	0	8×10^{-3}	-0.090±0.048	1.625±0.005	0.0338
C	0	4×10^{-3}	-0.096±0.043	1.626±0.004	0.0341
D	5.5×10^{-4}	1.6×10^{-2}	-0.079±0.044	1.620±0.005	0.0335
E	2.8×10^{-4}	1.6×10^{-2}	-0.094±0.044	1.623±0.005	0.0345
F	1.1×10^{-4}	1.6×10^{-2}	-0.088±0.044	1.623±0.005	0.0351
G	2.2×10^{-3}	3.4×10^{-2}	-0.061±0.026	1.612±0.003	0.0314
H[b]	1.1×10^{-4}	1.6×10^{-2}	-0.109±0.043	1.623±0.004	0.0346

[a]The time step (Δt) reduced by a factor of two in this case.
[b]No normal viscosity, ν=0.

the exact same number of oscillations. A simulation without hyper-dissipation that is not listed in the table also has $\Delta r=1.6\times10^{-2}$, and it suffers from obvious radial aliasing errors. Therefore, hyper-dissipation maintains numerical stability in cases D-F. Case G has one-fourth of the spatial resolution of A and just enough hyper-dissipation to avoid aliasing errors. The general behavior remains similar, but there are substantial discrepancies in F and rms(b), relative to the other cases. From this I conclude that the hyper-dissipation allows a factor of two reduction of radial resolution while preserving accuracy for average, global information.

The hyper-dissipation may be viewed as a means of modifying the numerical behavior of the normal dissipation algorithms. To show this, consider the decay of a flow-field under the influence of viscosity and hyper-viscosity. The coefficient of the j-th eigenfunction of the spatial operator ∇^2 evolves according to

$$\frac{\partial V_j}{\partial t} = -\left(\upsilon p_j^2 + \zeta p_j^4\right) V_j ,$$

where $-p_j^2$ is the j-th eigenvalue of ∇^2. The fully-implicit, finite difference form of this equation is

$$\frac{V_j^{n+1} - V_j^n}{\Delta t} = -\left(\upsilon \bar{p}_j^{-2} + \zeta \bar{p}_j^{-4}\right) V_j^{n+1} ,$$

where the superscripts on velocity indicate the temporal index, and $-\bar{p}_j^{-2}$ is the numerical approximation of $-p_j^2$. The amplification factor (G_N) is

$$\frac{V_j^{n+1}}{V_j^n} = \frac{1}{1 + \upsilon \Delta t \bar{p}_j^{-2} + \zeta \Delta t \bar{p}_j^{-4}} , \qquad (2.9)$$

which reduces to the well-known amplification factor for implicit diffusion when ζ=0.

The accuracy of the numerical dissipation can be investigated by comparing Eq. 2.9 with the analytic decay of normal dissipation, $G_A \equiv e^{-\upsilon\Delta t p^2}$. This comparison requires a relation between $-\bar{p}_j^2$ and $-p_j^2$, which is determined by the properties of the numerical spatial difference operator. The important feature of the finite-difference approximation is that it is accurate for scale-lengths that are large compared to the grid spacing. This is independent of the coordinate system, so I will use the relation $-\bar{p}_j^2 = 2\left[\cos\left(p_j\Delta x\right)-1\right]/(\Delta x)^2$ for Cartesian eigenfunctions e^{-ipx}, where Δx is the grid spacing, and $p \le \pi/\Delta x$. Using this in Eq. 2.9 and dividing by G_A produces the relation

$$\frac{G_N}{G_A} = \frac{e^{\upsilon\Delta t p^2}}{1+\upsilon\Delta t\dfrac{2[1-\cos(p\Delta x)]}{(\Delta x)^2}+\zeta\Delta t\left\{\dfrac{2[1-\cos(p\Delta x)]}{(\Delta x)^2}\right\}^2}. \qquad (2.10)$$

The degree of inaccuracy is then determined by the difference between this ratio and unity.

The dissipation accuracy resulting from the different numerical parameter sets in Table 2.1 are compared in Fig. 2.3, where the logarithm of the ratio defined in Eq. 2.10 is plotted as a function of radial wavenumber for six cases. [Cylindrical effects are ignored and $\Delta r \rightarrow \Delta x$.] The cases without hyper-dissipation show that the implicit scheme for normal dissipation provides less than analytic damping at large wavenumbers. For A-C, the numerical error is small, supporting the conclusion that case A is adequately resolved. However, when the resolution is reduced (case Z, not in Table 2.1), damping is inadequate and aliasing results. Adding hyper-dissipation remedies this problem. Case E has more damping than

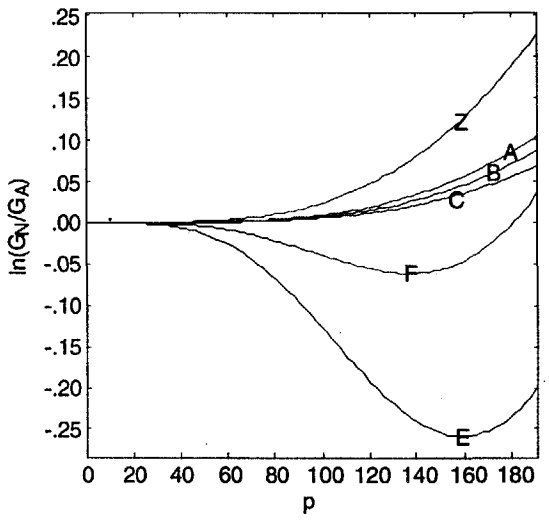

label	Δx	SΔt	ζ
A	.008	.1	0
B	.008	.05	0
C	.004	.1	0
Z	.016	.1	0
E	.016	.1	2.8×10^{-4}
F	.016	.1	1.1×10^{-4}

Figure 2.5 Ratios of numerical to analytic damping (Eq. 2.10) as a function of wavenumber for conditions relevant to the simulations in Table 2.1. The horizontal axis is the wavenumber domain that is resolved with a grid spacing of 0.016. The trace labeled B is for two time-steps to cover the same time increment as the other cases.

the analytic decay at high wavenumbers, but the hyper-dissipation essentially compensates the numerical error of the normal dissipation algorithm for case F

There are errors at large wavenumbers for all of the parameter choices, so an important issue is what wavenumbers are physically important. To estimate, the net power going into the fluctuations in case A is approximately 10 in the normalized units, while the magnetic fluctuation energy is approximately 0.05.

Dividing the latter by the former gives a fluctuation energy turnover time of 5×10^{-3}. With the resistivity normalization, this implies that all wavenumbers larger than 14 are highly damped. Thus, the physical dissipation begins in the low wavenumber region of Fig. 2.3, where the numerical schemes are accurate. This is also confirmed by the fact that in case E, the power dissipated by hyper-resistivity and hyper-viscosity is approximately 2, while in F it is approximately 1. These are small relative to the net power going into the fluctuations and much smaller than the total input power, which is approximately 100.

An additional simulation, case H in Table 2.1, has the normal viscosity set to zero, so that stabilization of small-scale velocity oscillations depends on the hyper-viscosity alone. There are only modest changes in the global performance parameters, so the normal viscosity also does not affect the MHD solutions significantly.

The three cases with hyper-dissipation and half the resolution of case A ran in approximately half of the CPU time with much less memory, so there is a substantial net savings in computational resources. This approach has made possible the largest S simulations of the scaling study presented in Chapter 3.

2.1.3 Finite Pressure

The pressureless versions of DEBS produce accurate information on MHD tearing mode behavior for low-β plasmas ($\beta \equiv 2\mu_0 P/B^2$), but they do not produce quantitative information on the important issue of thermal energy transport. To examine this issue, the finite-pressure code solves the pressure evolution equation

$$\left(1-\Delta t\nabla\cdot\underline{\underline{\kappa}}_{si}\cdot\nabla\right)\frac{\partial P}{\partial t} = -S\nabla\cdot(P\mathbf{V}) - S(\gamma-1)P\nabla\cdot\mathbf{V} + \frac{2(\gamma-1)}{\beta_0}\eta J^2 - \nabla\cdot\mathbf{q}\ , \qquad (2.11)$$

where P is normalized by its initial value on axis, and β_0 is the initial β on axis. The first two terms on the right side are advective and compressive terms from hydrodynamics. The third term is the ohmic heating from electron-ion collisions, which is transferred from magnetic energy. The resistivity is again a function of radius, but it is based on the Spitzer formula such that $\eta \sim \langle T\rangle^{-3/2}$, where T is the temperature. [Without density evolution, T=P in the normalized units.] The fourth term is the divergence of heat flux from anisotropic thermal conduction, $\mathbf{q} = -\underline{\underline{\kappa}}\cdot\nabla T$, and $\underline{\underline{\kappa}}$ is the local conductivity matrix. For the RFP simulations discussed later, the boundary conditions are selected to fix the pressure at the wall to be 1/10 of the initial pressure on axis. This allows thermal conduction out of the system, so that a quasi-steady state can be achieved. The momentum equation (Eq. 2.5) is also modified to include the pressure force,

$$(1-\alpha\Delta t\nabla^2)\frac{\partial \mathbf{V}}{\partial t} = -S\mathbf{V}\cdot\nabla\mathbf{V} + S\mathbf{J}\times\mathbf{B} - S\frac{\beta_0}{2}\nabla P + \nu\nabla^2\mathbf{V}\ . \qquad (2.12)$$

Dissipative heating from the viscous term in Eq. 2.12 is not included in Eq. 2.11, because it is not an accurate representation of the viscous damping in real plasmas, which is very anisotropic.

With two minor exceptions, the transport of energy through the system is modeled self-consistently. It enters through the applied electric field and resulting currents and is eventually transferred from the magnetic field to internal energy through ohmic dissipation. The internal energy then escapes to the wall with the aid of the magnetic fluctuations—details of this transport process are discussed in Chapter 3. One inconsistency is the viscous damping, mentioned above. The other stems from the lack of a continuity equation, which implies that the kinetic energy density evolution effectively has an extra factor of $(\nabla\cdot\mathbf{V})\left[\rho V^2/2 - P/(\gamma-1)\right]$.

This is usually negligible for tearing-mode dynamics. Even with the discrepancies, total power is conserved to better than 1%, and the error is mostly numerical truncation error, which can be reduced by using smaller time steps.

In the numerical leap-frog scheme, the pressure is time-centered with the vector potential, which has no explicit dependence on pressure and is advanced separately. The ohmic heating term in Eq. 2.11 is therefore based on the fully advanced current density. The hydrodynamic terms in Eq. 2.11 employ the predictor-corrector advance, which is fairly standard in computational fluid dynamics.

The real numerical challenge is the anisotropic thermal conduction for magnetized, fully ionized hydrogen. The electrons dominate the parallel conductivity with a $T^{5/2}$ temperature dependence, and the ions dominate the perpendicular conductivity, which is proportional to $\rho^2/B^2T^{1/2}$ (NRL Formulary, 1994). The parallel and perpendicular conductivities differ by many orders of magnitude, even in relatively low temperature plasmas, and an explicit time-step is far smaller than what is practical for evolving MHD tearing modes. Implicit methods are also not practical, due to the form of the conductivity matrix,

$$\underline{\kappa} = \kappa_\perp \mathbf{I} + (\kappa_\parallel - \kappa_\perp)\hat{\mathbf{b}}\hat{\mathbf{b}} ,$$

where $\mathbf{I}$ is the identity matrix, and $\hat{\mathbf{b}}$ is the local magnetic field direction vector. [I have implicitly assumed that the electron and ion temperatures are equivalent, so the $\hat{\mathbf{b}}\times\nabla$ terms from the two constituents cancel.] In general, and especially in RFPs, $\hat{\mathbf{b}}$ is composed of many Fourier modes. The thermal conduction operator $\nabla\cdot\underline{\kappa}\cdot\nabla$ is therefore a very complicated spatial operator—in either analytic or numerical form, and it is very difficult to invert.

The approach taken in DEBS is to use a semi-implicit operator (second term on the left side of Eq. 2.11) to stabilize the heat flux that is calculated with the old temperature. This is similar to the semi-implicit approach used for the momentum equation. The explicit $\nabla\cdot\mathbf{q}$ on the right side of Eq. 2.11 is found by the following sequence of steps: First, the parallel and perpendicular conductivities are found at each radius, based on the magnitudes of $\langle T\rangle$ and $\langle B\rangle$. [The θ-z variations in T and the magnitude of B are relatively small and are suppressed.] Second, a matrix rotation is carried out in physical space at each computational cell to find the conductivity matrix in cylindrical coordinates as a function of position. Third, the inner product between the local conductivity matrix and the local temperature gradient (transformed from the gradient in Fourier space) is computed to find the heat flux as a function of position. Finally, the heat flux is transformed to Fourier space, where its divergence is easily calculated.

The semi-implicit operator for the pressure has been modified during the course of this research, so a discussion of its accuracy is necessary. Considering the thermal conduction alone, the semi-implicit term produces the following partial differential equation:

$$(1-\chi\Delta t\mathbf{G})\frac{\partial T}{\partial t} = \mathbf{K}T , \qquad (2.13)$$

where $\mathbf{K} = \nabla\cdot\underline{\kappa}\cdot\nabla$, $\mathbf{G}$ is the semi-implicit operator, and χ is a constant whose value is determined by numerical stability conditions. The linear analysis of this equation is very similar to the analysis of the semi-implicit advance of the momentum equation, which is thoroughly described in Schnack, 1987. First, the temperature dependence of the conductivities is suppressed to make Eq. 2.13 linear. Then, the operators $\mathbf{K}$ and $\mathbf{G}$ are assumed to have complete sets of orthonormal

eigenfunctions, $\{\xi_k\}$ and $\{\zeta_l\}$, respectively. In analogy to Eq. 20 of Schnack, the coefficients of the **K** eigenfunctions then evolve according to

$$\frac{\partial a_k}{\partial t} = -\frac{\omega_k^2 a_k + \chi\Delta t \sum_{m\neq k} \frac{\partial a_m}{\partial t} \sum_l \sigma_l^2 b_{ml} b_{kl}^*}{1+\chi\Delta t \sum_l \sigma_l^2 \left|b_{kl}\right|^2}, \qquad (2.14)$$

where $-\omega_k^2$ is the eigenvalue associated with ξ_k for the operator **K**, $-\sigma_l^2$ is the eigenvalue associated with ζ_l for the operator **G**, and b_{kl} is the inner product of ζ_l and ξ_k.

As pointed out by Schnack, the semi-implicit modification leads to two sources of error. First, if **G** and **K** do not commute, the sum in the numerator on the right side of the Eq. 2.14 leads to unphysical coupling of the **K** eigenfunctions. The prescription for minimizing this error is to choose an operator **G** that closely approximates **K**; however, it must be more easily inverted than **K** to realize any benefit over implicit methods. The choice that is currently in DEBS is $\nabla\cdot\underline{\underline{\kappa}}_{si}\cdot\nabla$, where the elements of $\underline{\underline{\kappa}}_{si}$ are the θ-z averages of the diagonal elements and the θ-z off-diagonal element of the real conductivity matrix at each radial position. The semi-implicit conductivity elements are therefore functions of r, but the operator does not couple different Fourier modes. This is a reasonable choice in terms of the first type of error; as the magnetic field perturbations go to zero, **G** and **K** become identical. The second type of error results from the second term in the denominator of Eq. 2.14. This can be minimized only by ensuring that $\chi\Delta t\sigma_l^2 << 1$ for the modes of interest.

The finite difference form of the modified thermal conduction equation is

$$(1-\chi\Delta t\mathbf{G})\left(\mathbf{T}^{n+1}-\mathbf{T}^n\right) = \Delta t\mathbf{K}\mathbf{T}^n .$$

If we again resort to the use of the eigenfunctions of **K** and make the further approximation that **G** and **K** commute, the amplification factor becomes

$$\frac{a_k^{n+1}}{a_k^n} = \frac{1-\Delta t\omega_k^2+\chi\Delta t\sigma_k^2}{1+\chi\Delta t\sigma_k^2} .$$

The basic stability requirement is that $-1\le(a_k^{n+1}/a_k^n)\le 1$ for all k, because any error may be expanded in terms of the eigenfunctions of **K**, and a coefficient of error will grow in time if this condition is not met. The requirement is satisfied if

$$\chi\sigma_k^2 \ge \frac{\omega_k^2}{2}-\frac{1}{\Delta t}, \text{ and } \chi\sigma_k^2 \ge 0, \qquad (2.15)$$

for all k. As Δt becomes small with respect to $2/\omega_k^2$, χ may be reduced to zero, and the finite difference equation reverts to a simple explicit scheme. This ensures consistency with the original partial differential equation for T. In practice the actual eigenvalues are not found for either operator. The largest eigenvalues are approximated by multiplying $(\pi/\Delta r)^2$, $(m_{max}/r)^2$, and $(n_{max}/R)^2$ by the corresponding diagonal conductivity-matrix elements at each radius and then finding the maximum product over the entire radius. This approximation is then used to determine χ.

The algorithm has been tested in problems that compute only thermal conduction and in full-scale RFP simulations. Among the first group is a qualitative test that provides motivation for using the semi-implicit method. In this test, the perpendicular conduction coefficient is set to zero, so that heat should only flow

along the magnetic field lines. The field configuration is generated with a separate simulation that evolves the MHD without pressure. That simulation is started from a paramagnetic equilibrium with R/a=0.7 and $0 \le m \le 1$ and $-2 \le n \le 2$, so that the (m=1,n=-2) mode is the only resolved mode with a resonance surface. It grows until saturating quasilinearly by modifying the parallel current profile. The final b_r profile peaks at r=0.4—near the resonance surface, and this generates the large island structure displayed in the magnetic field-line puncture plot, Fig. 2.6a. With this field configuration fixed, the thermal conduction algorithm is then run for ten time-steps from a $\langle T \rangle = 1 - 0.9r^3$ profile. Additional modes are included ($0 \le m \le 5$ and $-10 \le n \le 10$) to capture the inherent coupling in the anisotropic conductivity matrix. The time-steps are 1.6×10^{-5}, and the normalized parallel conductivity is 1.7×10^5 (parameters similar to those used in full RFP simulations). The final temperature distribution should be constant along field lines, and Fig. 2.6b clearly shows the island structure. The thermal conduction algorithm therefore produces qualitatively correct results with a time-step that is nearly 1000 times larger than the explicit stability limit, yet it adds only 30% to the CPU time for a full simulation.

Quantitative tests of the thermal conduction algorithm have also been run with other dynamics suppressed. One suitable anisotropic conduction problem with an analytic solution has a uniform axial magnetic field and a vertical (1,0) field that is 100 times smaller. The temperature is initially unity throughout, and a (2,0) temperature perturbation of magnitude 0.1 is applied at the boundary. The phase of the perturbation is set so that the vertical field connects the cold surfaces at the top and bottom of the poloidal cross-section, and the perpendicular conductivity is again set to zero. Analytically, each vertical-axial plane is independent of all others, and the thermal conduction operator in Cartesian coordinates reduces to $\sin^2(\gamma)\kappa_\parallel \partial^2/\partial y^2$, where γ is the angle between the magnetic field and the $\hat{\mathbf{z}}$

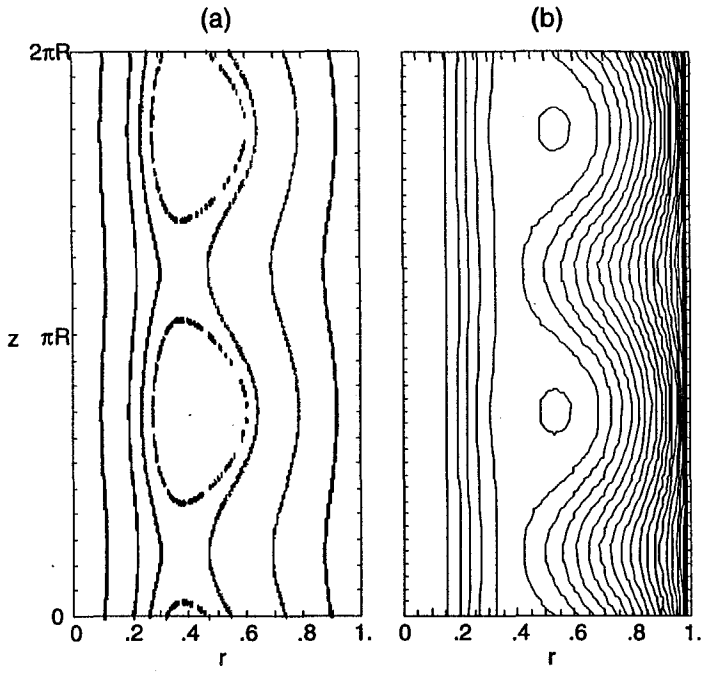

Figure 2.6 (a) Magnetic field puncture plot of the frozen field configuration, and (b) constant temperature contours after 10 time-steps with the semi-implicit algorithm.

direction, and y is the vertical coordinate. The steady-state temperature for a particular horizontal position x is

$$T = T_0 + \tilde{T}\left(2x^2 - 1\right),$$

where T_0 is the initial temperature and $\tilde{T}$ is the perturbation magnitude, or

$$T = \left[T_0 + \tilde{T}\left(r^2 - 1\right)\right] + \left[\frac{\tilde{T}r^2}{2} e^{-i2\theta} + \text{c.c.}\right] \tag{2.16}$$

in polar coordinates, where c.c. refers to the complex conjugate of the previous term. The time-dependent solution for a given x has the series form,

$$T = T_0 + \tilde{T}(2x^2 - 1)\left\{1 - \sum_{j=0}^{\infty}(-1)^j e^{-\alpha_j t} \frac{4}{(2j+1)\pi} \cos\left[\frac{(2j+1)\pi y}{2\sqrt{1-x^2}}\right]\right\}, \tag{2.17}$$

where $\alpha_j = \sin^2(\gamma)\kappa_{\parallel}\left[(2j+1)\pi / 2\sqrt{1-x^2}\right]^2$.

To verify the spatial accuracy of the algorithm, three simulations were run for 200 time-steps with varied levels of radial and poloidal resolution. The parallel conductivity is 1×10^4 and the time-steps are large, $\Delta t=1$, so the final temperature is in steady state and may be compared with Eq. 2.16. Figure 2.7 shows the errors associated with the (0,0), (2,0), and (4,0) modes for the different cases. Errors in other modes are much smaller. The largest error is five orders of magnitude smaller than the temperature perturbation, and this is improved with increased radial resolution. Increasing the poloidal resolution has little effect. This test shows that the spatial part of the algorithm—the seemingly complex procedure for finding $\nabla \cdot \mathbf{q}$—is quite accurate for typical resolution levels used in the simulations.

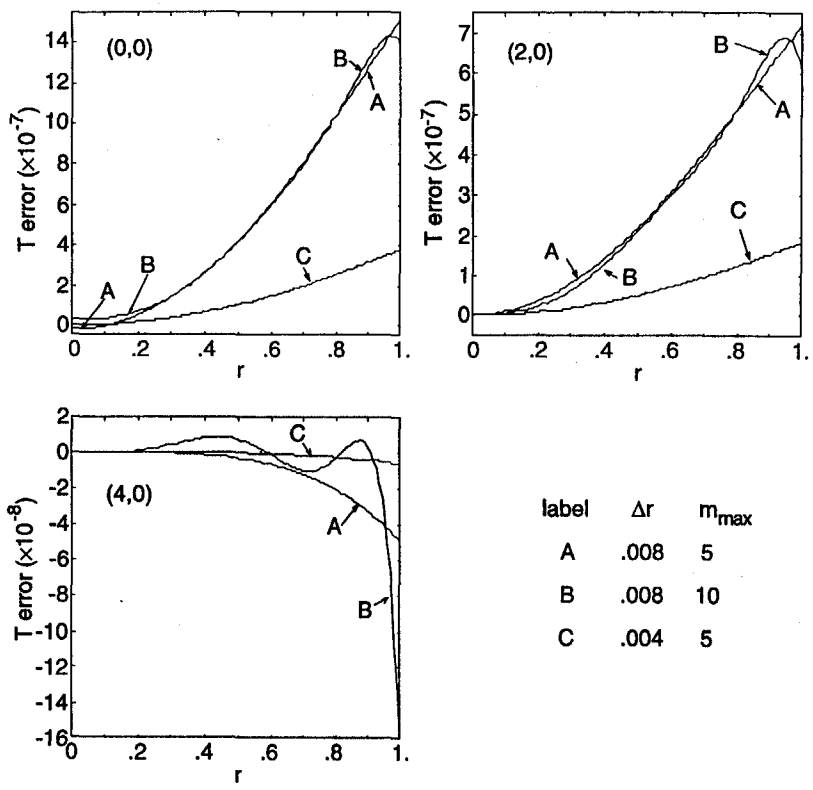

label	Δr	m_{max}
A	.008	5
B	.008	10
C	.004	5

Fig 2.7 Temperature errors in the steady-state solutions of three test cases (labeled A, B and C) with varied spatial resolution. The separate plots show the errors in the (0,0), (2,0), and (4,0) Fourier components. The magnitude of the imposed temperature perturbation is 0.1.

The temporal accuracy is examined by plotting the temperature as a function of time and comparing with the analytic solution. This is done in Fig. 2.8 for two different positions in four simulations. The first position is near the origin, where the θ-dimension of the computational cells is smallest, placing the most severe restriction on an explicit time-step. At this position, an e-folding decay of the largest term in the series of Eq. 2.17 occurs after 0.4 time units. The other location is near the wall in the horizontal midplane. Here the physical scale length is smaller, and the characteristic decay time is 0.04. Thus, the time-steps used in the tests are comparable to or even larger than the characteristic times. At both locations, the behavior of the algorithm is acceptable. As the time-step is decreased, the numerical solution converges to the analytic solution. In addition, the position near the wall shows that significant diffusion can occur in a single time-step.

The three cases with varied time-steps have χ set to twice the minimum value required by Eq. 2.15 (χ is replaced by $\chi_0\chi_1$, where χ_0 is the minimum that satisfies Eq. 2.15). Smaller values lead to numerical instabilities in this problem, and the unstable eigenfunctions distinctly show coupling of different Fourier modes. This appears to be a shortcoming of the choice of semi-implicit operator, which is linear in the Fourier representation and therefore does not respond to heat that is transferred from one mode to another. Fortunately, using $\chi_1>1$ maintains numerical stability, but the minimum necessary χ_1 is somewhat problem dependent. Full RFP simulations require χ_1 as large as 16. The impact of increasing χ_1 to 8 in the test case with $\Delta t=0.1$ is shown in Fig. 2.8 (compare traces C and E). The decay is slowed, and the error diminishes as the steady state is approached.

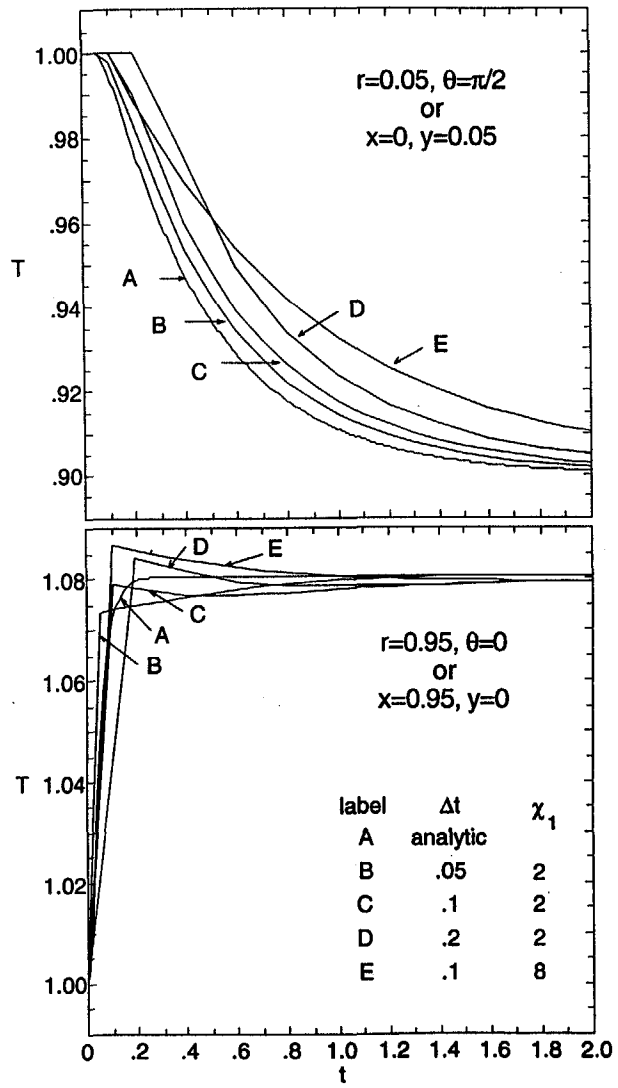

Fig. 2.8 Comparison of the temporal behavior of the thermal conduction algorithm with varied time-step and semi-implicit multiplier at the positions indicated.

Full RFP simulations use time-steps that are based on the MHD activity which is slow relative to parallel conduction along magnetic fluctuations, so the thermal transport process is quasi-steady on this time scale. As the magnetic fluctuations change over hundreds of time-steps, the computed parallel conduction has no problem with temporal accuracy. In this sense, the thermal transport at any given time is essentially an elliptic problem. The simulations in Chapter 3 conserve power to within 1%, and the heat flux results from parallel conduction along the fluctuations.

2.2 RESTER

While RFPs are best described by a nonlinear treatment, linear stability is an important component of the MHD model. It determines which modes access 'free' energy from the equilibrium field configuration, and these modes are large in the saturated state. Helicity injection for fluctuation suppression changes the mean-field distribution, and if successful, reduces available free energy. I therefore use linear calculations to guide current profile modification efforts.

The original analytic theory of resistive MHD stability is due to Furth, Killeen and Rosenbluth and uses planar geometry (Furth, 1963). Coppi, Greene and Johnson later revised this theory for the periodic cylinder (Coppi, 1966). A scalar equation is derived for the perturbed flux function that is associated with an individual Fourier mode. The radial domain is divided into a small 'inner' region at r_s and adjacent 'outer' regions. The resistivity is used as a small parameter, so that the resistive term in Eq. 2.3 is negligible everywhere except in the inner region, where large gradients exist. In the outer regions, neither resistivity nor inertia are important, and the displacement is essentially force-free and ideal. The solutions in the different regions are solved separately and matched at the interfaces, which defines an

eigenvalue problem. A positive growth rate results in the pressureless case if the eigenfunction has a positive jump in slope at r_s. Therefore, to determine stability, one needs to find the eigenfunction by solving the outer region equation.

In configurations without plasma pressure, the perturbed 'flux' associated with the (m,n) mode satisfies

$$\frac{d^2\psi}{dr^2} = -A\psi \tag{2.18}$$

in the outer regions, where $\psi = r^{3/2}b_r \Big/ \left(m^2 + k^2r^2\right)^{1/2}$,

$$-A = \frac{m^2 + k^2r^2}{r^2} - \lambda^2 + \frac{d\lambda}{dr}\frac{\left(m\langle B_z\rangle - kr\langle B_\theta\rangle\right)}{m\langle B_\theta\rangle + kr\langle B_z\rangle} - \frac{2\lambda mk}{m^2 + k^2r^2} - \frac{\left(m^4 + 10m^2k^2r^2 - 3k^4r^4\right)}{4r^2\left(m^2 + k^2r^2\right)^2} \tag{2.19}$$

and k=n/R (Robinson, 1978). This is derived from

$$\mathbf{j}\times\langle\mathbf{B}\rangle + \langle\mathbf{J}\rangle\times\mathbf{b} = 0 \quad \text{and} \quad \frac{\partial\mathbf{b}}{\partial t} = \nabla\times\left(\mathbf{v}\times\langle\mathbf{B}\rangle\right),$$

the linear versions of Eq. 2.2 and Faraday's law with the ideal part Eq. 2.3. There is no resistivity, no inertia, $\langle\mathbf{V}\rangle$ is negligible, and $\nabla\cdot\mathbf{v} = 0$ is used to give the least-stable displacement (Newcomb, 1960). Equation 2.18 is a linear, homogeneous, ordinary differential equation, but it is singular at the origin and at r_s. [For now it is assumed that there is only one resonance surface for a given mode. The problem of multiple resonance surfaces is discussed later in this section.] A simple

numerical integration can be used to determine the linearly independent solutions away from the singularities. However, as these points are approached, the asymptotic behavior must be incorporated. Robinson did this by using a comparison equation (Robinson, 1978), and I have implemented this approach in RESTER.

Assuming that the wall is a perfect conductor, the eigenfunction is zero at r=1, and proper behavior at the origin is determined by the regularity conditions, $\psi \sim r^{m+1/2}$ for m>0 and $\psi \sim r^{3/2}$ for m=0. The numerical integration starts with the correct behavior at the origin and marches outward in radius. The comparison equation is used to integrate through the singularity at r_s, which produces a solution that has no slope discontinuity. This solution is denoted ψ_0 and does not satisfy the boundary condition $\psi(1)=0$. To construct the eigenfunction, another linearly independent solution is needed. After computing this solution, the eigenfunction in $r_s \le r \le 1$ is the linear combination that satisfies the boundary condition at r=1 and matches ψ_0 at r_s. [The matching at r_s satisfies the restriction of the 'constant ψ' approximation that is used in the inner region analysis. This implies that the modes must not be close to ideal instability (Furth, 1963 and Coppi, 1966).] The eigenvalue,

$$\Delta' \equiv \lim_{\varepsilon \to 0} \frac{\left.\frac{d\psi}{dr}\right|_{r_s+\varepsilon} - \left.\frac{d\psi}{dr}\right|_{r_s-\varepsilon}}{\left.\psi\right|_{r_s}}, \tag{2.20}$$

is then used to determine stability.

The comparison equation has the same form as Eq. 2.18: $d^2u/dx^2 + Q(x)u = 0$, where $x=r-r_s$. It also has the same singular behavior, which is determined by an

expansion of Eq. 2.19. The key is that it has known solutions. The perturbed flux is then assumed to have the form

$$\psi(x) = \alpha(x)u_1(x) + \beta(x)u_2(x),$$

where u_1 and u_2 are two linearly independent solutions of the comparison equation. With the additional condition,

$$\frac{d\alpha}{dx}u_1 + \frac{d\beta}{dx}u_2 = 0, \tag{2.21}$$

it is easy to show that

$$\frac{d^2\psi}{dx^2} = \frac{d\alpha}{dx}\frac{du_1}{dx} + \frac{d\beta}{dx}\frac{du_2}{dx} - (\alpha u_1 + \beta u_2)Q. \tag{2.22}$$

Subtracting Eq. 2.22 from Eq. 2.18, with the assumed form of ψ, yields

$$\frac{d\alpha}{dx}\frac{du_1}{dx} + \frac{d\beta}{dx}\frac{du_2}{dx} = (\alpha u_1 + \beta u_2)(Q - A), \tag{2.23}$$

and this is not singular at r_s. Furthermore, Eqs. 2.21 and 2.23 are linearly independent, so one may solve for $d\alpha/dx$ and $d\beta/dx$:

$$\begin{pmatrix} \frac{d\alpha}{dx} \\ \frac{d\beta}{dx} \end{pmatrix} = \frac{1}{\frac{du_1}{dx}u_2 - \frac{du_2}{dx}u_1} \begin{pmatrix} u_2 & -\frac{du_2}{dx} \\ -u_1 & \frac{du_1}{dx} \end{pmatrix} \begin{pmatrix} (Q-A)(\alpha u_1 + \beta u_2) \\ 0 \end{pmatrix}. \tag{2.24}$$

This is Robinson's Eq. 13. Note that the denominator on the right side of Eq. 2.24 is the Wronskian of the two linearly independent solutions, so it is never zero.

The singular term at r_S in Eq. 2.19 is expanded in x in the following manner,

$$-\frac{(\lambda'+\lambda''x+\ldots)\left[m\left(\langle B_z\rangle+\langle B_z\rangle' x+\ldots\right)-k(r_s+x)\left(\langle B_\theta\rangle+\langle B_\theta\rangle' x+\ldots\right)\right]}{(r_s+x)\left(F'x+\frac{F''x^2}{2}+\ldots\right)}$$

where the mean fields are evaluated at r_S, $F\equiv m\langle B_\theta\rangle+kr\langle B_z\rangle$, primes indicate d/dx, and it is assumed that $F'\neq 0$ at r_S. To order x^0, this expression is

$$-\frac{\lambda'(m\langle B_z\rangle-kr_s\langle B_\theta\rangle)}{xF'r_s}-\frac{\lambda''(m\langle B_z\rangle-kr_s\langle B_\theta\rangle)}{F'r_s}-\frac{\lambda'\left(m\langle B_z\rangle'-k\langle B_\theta\rangle-kr_s\langle B_\theta\rangle'\right)}{F'r_s}$$
$$+\frac{\lambda'(m\langle B_z\rangle-kr_s\langle B_\theta\rangle)}{F'r_s^2}+\frac{\lambda'(m\langle B_z\rangle-kr_s\langle B_\theta\rangle)F''}{2F'r_s}.$$

The first term of this varies as 1/x, and the coefficient is Robinson's G. The remaining terms plus other terms in Eq. 2.19 evaluated at r_S are his G_1. The function Q(x) is then set to $G/x+G_1+R(x)$, with

$$R(x)=\left[x\left(6a^3-16ab\right)+x^2\left(4a^4-14b^2-2a^2b\right)\right.$$
$$\left.+x^3\left(8a^3b-14ab^2\right)+x^4\left(4a^2b^2-6b^3\right)\right]$$
$$+\left(1+ax+bx^2\right)^2$$

where a=G/2, $b=(G^2+G_1)/6$, and published typographical errors have been corrected in the expressions for Q(x) and R(x).

Robinson's choice of Q(x) means that Q-A (which appears in Eq. 2.24) is of order x, and the solutions of the comparison equation have the closed forms,

$$u_1(x)=\frac{x}{1+ax+bx^2}$$

$$u_2(x)=u_1(x)\left[-\frac{1}{x}+2a\ln|x|+\left(a^2+2b\right)x+abx^2+\frac{b^2x^3}{3}\right].$$

Neither solution is singular at x=0; however, the denominator of u_1 may be zero elsewhere. This is not a serious problem, because the comparison equation is only needed near the resonance surface. One may integrate Eq. 2.18 to a point between the u_1 singularity and r_S in an ordinary manner, transition to Eq. 2.24 to get across r_S, then integrate to the wall or to a point before the next u_1 singularity and transition again if necessary.

For the second linearly independent solution in $r_S\leq r\leq 1$, it is convenient to choose one that behaves like u_1 near r_S, so that a linear combination of this solution and ψ_0 changes Δ' without creating a discontinuity in ψ. In fact, when the second solution (ψ_i) is found by marching from r_S with $\beta(x=0)$ set to zero and $\alpha(x=0)$ set to unity, the ideal stability is determined. This solution is Newcomb's 'small' solution in this region, after a change of variables from the perturbed displacement to the perturbed flux (Furth, 1973). To paraphrase Newcomb's theorems, ideal stability is determined by finding the solution that is small on the left side of each independent region. These regions are bounded by the origin, the resonance surface, and the conducting wall. The proper small solution in $0<r<r_S$ is the

segment of ψ_0 in this domain. If the small solution in each region does not change sign, the configuration is ideally stable (Newcomb, 1960). [Suydam's condition must also be checked at each resonance surface when finite pressure is considered.]

Once ψ_0 and ψ_i have been found, the eigenfunction is constructed according to the conditions,

$$\psi(r=1) = \psi_0(r=1) + c\psi_i(r=1) = 0 ,$$

or $c = -\psi_0(r=1)/\psi_i(r=1)$. Since the slope of ψ_i is unity as r_s is approached from the right, c is the discontinuity of $d\psi/dr$ in the numerator of Eq. 2.20. The eigenvalue is then

$$\Delta' = -\frac{\psi_0(1)}{\psi_i(1)\psi_0(r_s)} . \qquad (2.25)$$

Observe that stability can be determined without computing Δ'. As long as the configuration is ideally stable, the denominator of Eq. 2.25 is positive, so the sign of Δ' depends on the sign of $\psi_0(1)$. *If ψ_0 is positive throughout the domain, $\Delta' < 0$,* and the mode is resistively stable. Note that an ideally stable configuration cannot produce an eigenfunction that is zero at both the wall and some position between r_s and the wall. If it did, this segment of the eigenfunction and ψ_i, which are two linearly independent solutions in $r_s<r<1$, would violate Sturm's separation theorem (Derrick, 1982).

A paramagnetic equilibrium similar to the one plotted in Fig. 2.1 provides an excellent example, because the m=1 modes show all possible results. This

equilibrium has E_Z=3.95 with $B_Z(0)$=1 and a flat resistivity profile. [In Fig. 2.1 the paramagnetic equilibrium has E_Z=3.8] The ψ_0 and ψ_i solutions of four modes computed by RESTER are shown in Fig 2.9. With R/a=3, the resonance surface nearest the axis is associated with the (m=1,n=-6) mode, and it is ideally unstable because $\psi_i(1)<0$. The (1,-5) mode is not resonant, so it cannot be resistively unstable, but it is ideally unstable—though it is very close to being marginal. The (1,-7) is ideally stable, because $\psi_i(1)>0$, but it is resistively unstable as $\psi_0(1)<0$. This mode is close to ideal instability, so the resistive analysis with the 'constant ψ' approximation is not strictly valid. However, the $-21 \le n \le -8$ modes are also resistively unstable, so the n=-7 mode is definitely unstable. The (1,-22) mode is the first that is both ideally and resistively stable; both solutions are positive at the wall.

A mode may have more than one resonance surface when the safety factor is a nonmonotonic function of radius. In the RFP, the most common reason for this occurrence is the high resistivity near the wall. If the resistivity is large enough to suppress all current, then B_Z is constant and B_θ is proportional to 1/r in this region. The safety factor then has an inflection and bends upward near the wall. An example of this is the paramagnetic equilibrium in Fig. 2.1. A nonmonotonic safety factor profile may also result from current-profile modification. If the additional current drive is strong, it can produce a large degree of axial field reversal, and the applied axial electric field can drive the parallel current below zero. To handle these possibilities, the algorithm in RESTER determines stability for modes with up to two resonance surfaces. More than two resonance surfaces for a single mode has not been encountered.

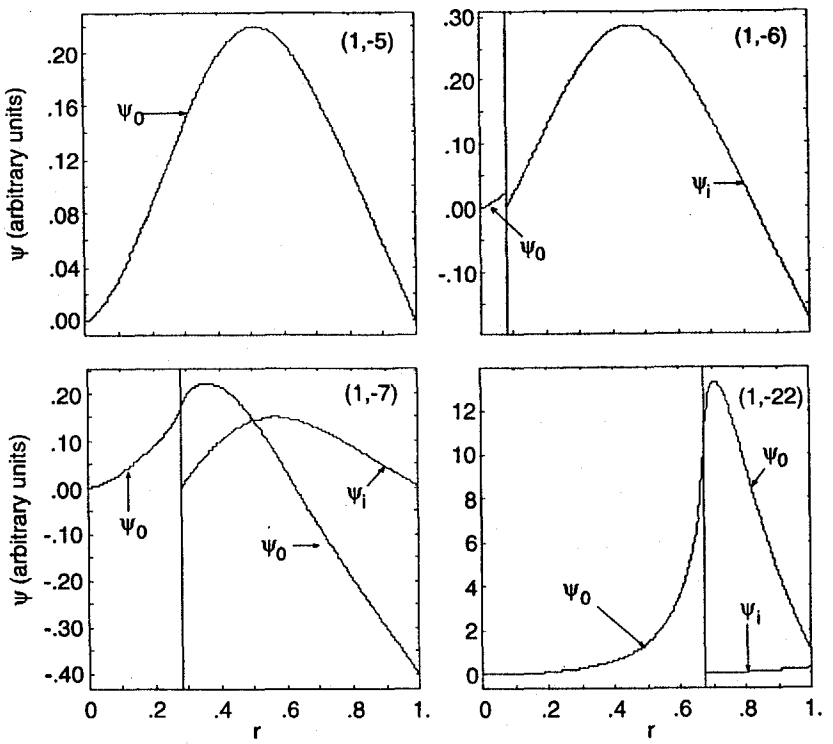

Figure 2.9 Perturbed flux solutions for the paramagnetic equilibrium with E_z=3.95 and $B_z(0)$=1. The four plots show the solutions for the Fourier modes indicated, and the vertical lines indicate r_s for the modes that have resonance surfaces.

When there are two resonance surfaces, the ideal stability determination only requires the consideration of an additional independent region; however, the resistive stability determination is slightly more complicated than it was with one resonance surface. There are two inner regions and three outer regions. The

outer region bounded on the left by the origin again has only one possible solution, but the other outer regions have two possible solutions each. The boundary condition at the wall determines the linear combination in the region between the second resonance surface and the wall, and an additional condition is needed to determine the eigenfunction. That condition is the matching of the temporal behavior at the two resonance surfaces. For the problems considered here, the modes are purely growing. Thus, the eigenfunction must produce the same growth rate in the two inner regions. The derivation that follows has this physical basis, but its form otherwise follows the 'double-tearing' analysis in Dewar, 1993. [Dewar uses this situation as an example for a general mathematical formalism for modes that couple multiple resonance surfaces.]

In the limit of vanishing pressure, the inner region analysis yields the following relation between the growth rate (γ) and the normalized change of the flux function's slope across the inner region (Δ):

$$\gamma \propto \Delta^{4/5}\eta^{3/5}\left(\frac{F'^2}{\rho}\right)^{1/5} \qquad (2.26)$$

with the physical quantities evaluated at a particular resonance surface (Furth, 1963 and Robinson, 1978). It is convenient to use the general relation $\Delta_j = K_j\gamma^{\varsigma}$, where the subscript j is the surface index and ς is a fraction. A physically meaningful eigenfunction then results when the outer solutions are matched to the inner solutions, $\Delta'_1 = \Delta_1$ and $\Delta'_2 = \Delta_2$, and the temporal behavior in the two inner layers match, $\Delta_1/K_1 = \Delta_2/K_2$. Note that the eigenfunction discontinuities, Δ'_1 and Δ'_2, are not necessarily the same.

For convenience and consistency with Dewar, the eigenfunction is constructed in two steps. First, the solutions ψ_1 and ψ_2 are constructed from the solution in the region adjacent to the origin and from the linearly independent solutions in the other two outer regions. Each covers two of the outer regions: ψ_1 is equivalent to a single-resonance eigenfunction with a wall at r_{s2}, and ψ_2 is an eigenfunction for an annular region formed by an additional conducting wall at r_{s1} (see Fig. 2.10). A linear combination of these solutions always satisfies the boundary conditions, and the temporal matching sets the proportionality of the linear combination.

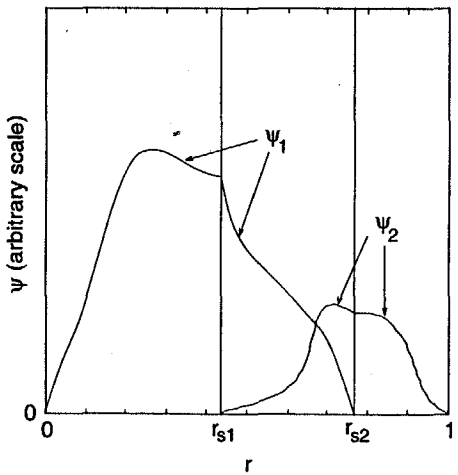

Figure 2.10 Sketch of intermediary eigenfunctions ψ_1 and ψ_2 for an ideally stable mode with two resonance surfaces, r_{s1} and r_{s2}.

The following quantities are used to assist the temporal matching:

$$\Delta'_{11} \equiv \lim_{\varepsilon\to 0} \frac{\left.\frac{d\psi_1}{dr}\right|_{r_{s1}+\varepsilon} - \left.\frac{d\psi_1}{dr}\right|_{r_{s1}-\varepsilon}}{\psi_1|_{r_{s1}}}$$

$$\Delta'_{22} \equiv \lim_{\varepsilon\to 0} \frac{\left.\frac{d\psi_2}{dr}\right|_{r_{s2}+\varepsilon} - \left.\frac{d\psi_2}{dr}\right|_{r_{s2}-\varepsilon}}{\psi_2|_{r_{s2}}}$$

$$\Delta'_{12} \equiv \lim_{\varepsilon\to 0} \frac{\left.\frac{d\psi_2}{dr}\right|_{r_{s1}+\varepsilon}}{\psi_2|_{r_{s2}}}$$

$$\Delta'_{21} \equiv \lim_{\varepsilon\to 0} \frac{-\left.\frac{d\psi_1}{dr}\right|_{r_{s2}+\varepsilon}}{\psi_1|_{r_{s1}}}.$$

The first two represent the slope discontinuities of ψ_1 and ψ_2 at their respective rational surfaces. The second two represent the slope discontinuities induced by ψ_1 and ψ_2 at the opposite rational surface. All of these quantities are known once the linearly independent solutions are computed in each region.

The final eigenfunction is a linear combination of ψ_1 and ψ_2, and the resulting slope discontinuities are linear combinations of the four quantities defined above. With $\psi = \psi_1 + B\psi_2$,

$$\Delta'_1 = \Delta'_{11} + \frac{B\psi_2|_{r_{s2}}\,\Delta'_{12}}{\psi_1|_{r_{s1}}} \text{ and}$$

$$\Delta_2' = \Delta_{22}' + \frac{\psi_1|_{r_{s1}} \Delta_{21}'}{B\psi_2|_{r_{s2}}}.$$

Setting Δ_1' to $K_1\gamma^S$ gives B in terms of γ^S. Substituting this in the expression for Δ_2' produces a dispersion relation for γ^S:

$$K_1K_2\left(\gamma^S\right)^2 - (K_2\Delta_{11}' + K_1\Delta_{22}')\gamma^S + \Delta_{11}'\Delta_{22}' - \Delta_{12}'\Delta_{21}' = 0\,. \qquad (2.27)$$

The solutions are

$$\gamma^S = \frac{(K_2\Delta_{11}' + K_1\Delta_{22}') \pm \sqrt{(K_2\Delta_{11}' + K_1\Delta_{22}')^2 - 4K_1K_2(\Delta_{11}'\Delta_{22}' - \Delta_{12}'\Delta_{21}')}}{2K_1K_2}, \qquad (2.28)$$

which may be compared with Dewar's Eqs. 61-63 where the viscous limit of the inner layer solution is used, including differential rotation between the rational surfaces.

A configuration is unstable when either of the solutions in Eq. 2.28 is positive. This is the case when either Δ_{11}' or Δ_{22}' is positive (Dewar, 1993). To demonstrate this, the discriminant of Eq. 2.28 is rewritten as $(K_2\Delta_{11}' - K_1\Delta_{22}')^2 + 4K_1K_2\Delta_{12}'\Delta_{21}'$. By definition, K_1 and K_2 are positive. The quantities Δ_{12}' and Δ_{21}' are also positive when the configuration is ideally stable (Manickam, 1983). In the region $r_{s1}<r<r_{s2}$, ψ_2 is Newcomb's small solution with a positive slope on the left and a positive value at r_{s2} if ideally stable, so $\Delta_{21}' > 0$. A similar argument can be made for Δ_{12}', except the small solution starts from the right side of the interval at r_{s2}, which is equally valid (Newcomb, 1960). The discriminant is therefore positive, and its root is large enough to make the numerator of Eq. 2.28 positive.

Having Δ_{11}' and Δ_{22}' both negative is not a sufficient condition for stability, however. From the form of the discriminant in Eq. 2.28, it is apparent that a positive solution still exists unless $\Delta_{12}'\Delta_{21}' < \Delta_{11}'\Delta_{22}'$ (Dewar, 1993). Both of these conditions are checked in RESTER to determine the resistive stability of a mode with two resonance surfaces.

The procedure carried out in RESTER begins by numerically solving for the equilibrium fields and safety factor from a model specified by the user. The code then cycles through the desired Fourier modes, and determines the ideal and resistive stability for each in the following five steps: 1) The radial domain is searched to determine the number of resonance surfaces for the current mode. 2) The grid is adjusted so that grid points do not coincide with resonance surface locations, and the equilibrium quantities are recalculated on the new grid. Functions such as F(r), λ(r) and λ'(r) are also determined, and the singular functions A(r) and Q(x) are computed separately and subtracted, so the grid rescaling prevents floating point errors. 3) For each resonance surface, the roots of the u_1 denominator are determined. The code then creates of set of instructions that tell the integration procedures where to make transitions from the use of one comparison equation to another or to a straightforward integration without a comparison equation. This is probably the most complicated part of the code due to all of the possibilities when there are two resonance surfaces. 4) The 'ideal' solutions are computed in each region, and ideal stability is determined. 5) If the mode is ideally stable, ψ_0 is computed to determine resistive stability.

The code has been applied to many equilibria, and it produces reliable results. To verify accuracy, I have compared output with a paramagnetic equilibrium discussed by Robinson. The resistivity profile is flat, and the most unstable mode is the m=1, k=-0.60 mode. In Robinson's units, the normalized current density on axis

is unity, and the wall location for marginal stability is 2.4527 (Robinson, 1978). Converting to the normalizations used here, the value of Robinson's wall location becomes $J_z(0)$. In a convergence test with 2047, 4095, and 8191 radial cells, the marginal values are 2.468, 2.461, and 2.457, respectively. Thus, RESTER converges to Robinson's result. The marginal level of $J_z(0)$ for ideal stability computed by RESTER for this mode is 4.1. This also matches the graphical information in Robinson's Fig. 2 (a numerical value is not given). For the Bessel function model (Gibson, 1968), where $\lambda(r)$ is a constant, RESTER finds the onset of instability at λ=3.112; the often-quoted value is Θ=1.56 or λ=3.12. Finally, it should be pointed out that modes resonant at the origin demand special treatment (Robinson, 1978), and this is not done in RESTER.

References

D. A. Anderson, J. C. Tannehill, and R. H. Pletcher, *Computational Fluid Mechanics and Heat Transfer,* (Hemisphere Publishing, 1984).

V. Antoni, D. Merlin, S. Ortoloni, R. Paccagnella, "MHD Stability Analysis of Force-free Reversed Field Pinch Configurations," Nucl. Fusion **26**, 1711 (1986).

A. Y. Aydemir, D. C. Barnes, E. J. Caramana, A. A. Mirin, R. A. Nebel, D. D. Schnack, and A. G. Sgro, "Compressibility as a Feature of Field Reversal Maintenance in the Reversed-field Pinch," Phys. Fluids **28**, 898 (1985).

R. J. Bickerton, "The Amplification of a Magnetic Field by a High Current Discharge," Proc. Phys. Soc. **72**, 618 (1958).

L. A. Charlton and B. A. Carreras, "The effect of Compressibility on Magnetohydrodynamic Instabilities in Toroidal Geometry," Phys. Fluids B **2**, 539 (1990).

B. Coppi, J. M. Greene, and J. L. Johnson, "Resistive Instabilities in a Diffuse Linear Pinch," Nucl. Fusion **6**, 101 (1966).

W. R. Derrick and S. I. Grossman, *Elementary Differential Equations with Applications,* 2nd ed., (Addison-Wesley Publishing, 1982).

J. H. Ferziger, "Higher-level Simulations of Turbulent Flows," in *Computational Methods for Turbulent, Transonic and Viscous Flows,* edited by J. A. Essers, 93 (Hemisphere Publishing, 1983).

H. P. Furth, J. Killeen, and M. N. Rosenbluth, "Finite-resistivity Instability of a Sheet Pinch," Phys. Fluids **6**, 459 (1963).

R. D. Gibson and K. J. Whiteman, "Tearing Mode Instability in the Bessel Function Model," Plasma Phys. **10**, 1107 (1968).

D. S. Harned and W. Kerner, "Semi-implicit Method for Three-dimensional Compressible Magnetohydrodynamic Simulation," J. Comput. Phys. **60**, 62 (1985).

Y. L. Ho and S. C. Prager, "Nonlinear Reversed-field Pinch Dynamics with Nonideal Boundaries," Phys. Fluids B **3**, 3099 (1991a).

Y. L. Ho, "Numerical Simulation of Fluctuation Suppression via DC Helicity Injection in a Reversed-field Pinch," Nucl. Fusion **31**, 341 (1991b).

J. W. Johnson, "A Plasma Model for Reversed Field Pinch Circuit Design," Plasma Phys. **23**, 187 (1981).

N. A. Krall and A. W. Trivelpiece, *Principles of Plasma Physics,* (San Francisco Press, 1986).

J. Manickam, R. C. Grimm and R. L. Dewar, in *Energy Modeling and Simulation,* IMACS, edited by A. S. Kydes, A. K. Agrawal, S. Rahman, R. Vichnevetsky, and W. F. Ames, 355 (North-Holland, 1983).

J. C. McWilliams, "The Emergence of Coherent Vortices in Turbulent Flow," J. Fluid Mech. **146**, 21 (1984).

A. A. Mirin, D. R. Martin, and N. J. O'Neill, "TUBE88-A Code Which Computes Magnetic Field Lines," Comput. Phys. Comm. **54**, 183 (1989).

NRL Plasma Formulary, edited by J. D. Huba, NRL/PU/6790--94-265 (Office of Naval Research, 1994).

W. A. Newcomb, "Hydromagnetic Stability of a Diffuse Linear Pinch," Ann. Phys. **10**, 232 (1960).

D. C. Robinson, "Tearing-mode-stable Diffuse-pinch Configurations," Nucl. Fusion **18**, 939 (1978).

D. D. Schnack, D. C. Barnes, Z. Mikic, D. S. Harned, and E. J. Caramana, "Semi-implicit Magnetohydrodynamic Calculations," J. Comput. Phys. **70**, 330 (1987).

K. L. Sidikman, "Self-consistent Field Error Effects in Reversed Field Pinch Plasmas," Ph.D. thesis, University of Wisconsin-Madison (1990).

3. MHD ACTIVITY AND ENERGY CONFINEMENT IN THE RFP

The MHD equations form a fairly complete model of the RFP, and the solutions to these equations capture many—if not most—of the important features of experiments. The model is a driven/damped system of interacting Fourier modes, and the rich, dynamic behavior can be explained in terms of the power flow. To lay the foundation for this discussion, I will begin with the power flow through the paramagnetic equilibrium. This is a simple system, but it is not realistic because it is unstable. Considering the instabilities then leads to the RFP configuration.

It has already been shown in Chapter 2 that the parallel current and safety factor profiles of the paramagnetic equilibrium are similar to those in an RFP. The current density is everywhere parallel to the magnetic field in the limit of vanishing plasma pressure, and it satisfies the parallel component of Ohm's law. The perpendicular component is satisfied through a mean, inward drift: $\langle V_r \rangle = -\langle E_z \rangle \langle B_\theta \rangle / S \langle B \rangle^2$ in the normalized units with time in terms of τ_r (where the magnitude of E_z for a given configuration is independent of η_0). The simple vector addition is illustrated in Fig. 3.1, showing that the applied axial electric field sustains azimuthal current when the magnetic field is not purely axial or azimuthal. Since both components of Ohm's law are satisfied, the paramagnetic equilibrium does not resistively decay.

The energy in this system is predominantly magnetic energy. Poynting's theorem in steady state simplifies to

$$-\frac{1}{r}\frac{\partial}{\partial r} r\left(S\langle V_r \rangle \langle B \rangle^2\right) = \eta \langle J \rangle^2 , \qquad (3.1)$$

using the radial velocity and the parallel component of Ohm's law (from Eq. 2.6). A volume integral of Eq. 3.1 over the region within some radius $r' \leq 1$ shows that the inward pinching flow is feeding magnetic energy across the $r=r'$ surface to balance the resistive dissipation in this volume:

$$-Sr\langle V_r \rangle \langle B \rangle^2 \Big|_{r=r'} = \int_0^{r'} \eta \langle J \rangle^2 r dr .$$

In the RFP, the majority of the power has the same fate, but the remaining 10% is redistributed by the fluctuations.

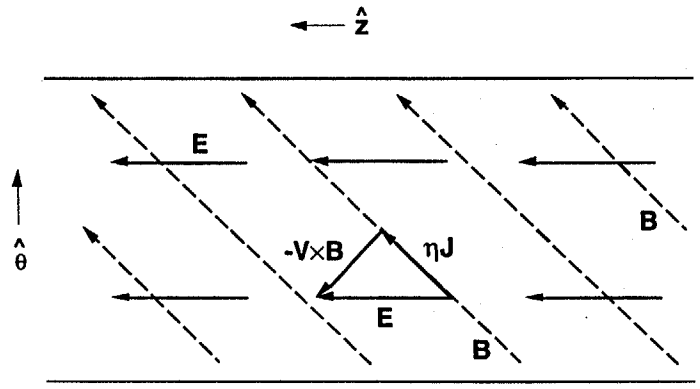

Figure 3.1 Sketch of electric and magnetic fields in a constant-r plane in the paramagnetic equilibrium. The radius illustrated is approximately halfway between the axis and the wall. At smaller r the magnetic field is more axial, while at larger r, it is more azimuthal.

The inward pinching flow has divergence, so the system as described does not satisfy a steady-state continuity equation. This is not a major inconsistency, however. From Eq. 3.1, it is clear that the magnitude of the drift velocity scales as 1/S when the resistivity profile and the distributions of $\langle \mathbf{B} \rangle$ and $\langle \mathbf{J} \rangle$ are fixed. As the overall resistivity level is decreased, less magnetic energy is needed to balance the dissipation. For the S-values of interest, the drift velocity is small, so the density accumulation over the duration of an experimental discharge is small. This minor inconsistency also exists in the RFP simulations, since the continuity equation is not evolved. Modeling a complete system would presumably lead to fluctuation-induced density transport that balances the pinch. [The smallness of the drift also justifies neglecting $\langle \mathbf{V} \rangle \cdot \nabla \langle \mathbf{V} \rangle$ when setting $\langle \mathbf{J} \rangle$ parallel to $\langle \mathbf{B} \rangle$ for the equilibrium.]

The DEBS simulation results in Section 2.1 and the RESTER example in Section 2.2 show the unstable nature of the paramagnetic equilibrium when an RFP-sized electric field is applied. The reason it is unstable stems from the relation between the magnetic field shear and the parallel current profile. Normally, shear is considered stabilizing, because it prevents interchange instabilities, where columns of adjacent flux tubes slip past each other (Schmidt, 1979). In this case, the large axial electric field drives a large current density on axis, and this shears the magnetic field away from the axial direction. At large radii, the magnetic field is mostly azimuthal, so the current drive is weak. Therefore, the parallel current density profile is very peaked, as it is in Fig. 2.1c. The safety factor profile in Fig. 2.1d drops to a small value near the wall, because the axial flux is packed into the center.

That the peaked distribution is unstable can be roughly explained by a thought experiment. If one could decrease the peaking of the current profile while maintaining the same total current and axial flux, the value of $\langle B_\theta \rangle$ will decrease or

remain the same at each radial position, courtesy of Ampere's law. The axial flux will also be less tightly packed, so the magnetic energy decreases. The magnetic energy acts as potential energy, so if lower energy, flatter distributions are accessible through fluid motions, then perturbations are unstable. This argument is similar to reasoning behind the Taylor hypothesis, where magnetic helicity and axial flux are held constant (Taylor, 1974). However, the thought experiment is not the basis for another minimization hypothesis—minimizing magnetic energy in this manner produces a uniform axial field surrounded by surface current, which is not an equilibrium without plasma pressure.

This is not to say that all paramagnetic equilibria are unstable. If the dimensionless $\langle E_z \rangle$ is less than 2.45 and the resistivity profile is flat, the configuration is stable to both resistive and ideal modes. This fact has been used to validate RESTER results in Section 2.2. Stable paramagnetic equilibria have less shear and broader parallel current profiles than the one in Fig. 2.1. The problem with these configurations is that the current density does not fall to zero at the wall, so it is unrealistic. A realistic resistivity profile that is large near the wall also leads to unstable current profiles at this level of electric field.

Flattening the current profile for stability is moving towards the Taylor state. But, Ohm's law gives a unique prescription for the parallel current if there are only mean fields, so only paramagnetic equilibria are steady under resistive diffusion. [The Taylor state also suffers from a parallel current profile that does not drop to zero at the wall.] Therefore, the RFP sustained by axial electric field alone always has magnetic fluctuations.

In the following section, I discuss results from the basic version of DEBS that show how the fluctuations modify the power flow and hence the current profile. The model is completed by the transport of thermal energy out of the system, and this

aspect is considered in Section 3.2 with results from the finite-pressure DEBS code. In Section 3.3, I revert to the pressureless system to examine the S-scaling of the magnetic fluctuation level.

3.1 RFP Power Flow

There are two important features of the quasi-steady RFP configuration, which were given brief mention in Section 2.1. The first is the sustainment of mean azimuthal current at the reversal surface, where on average the magnetic field is perpendicular to the applied electric field. The second is that the MHD modes saturate and do not grow so large as to disrupt the discharge. These features are related; sustaining the poloidal current requires power which comes from the fluctuations. If the fluctuations could not transfer this power to the mean fields, they would grow to a larger level, possibly leading to disruption.

When there are Fourier modes other than the mean field, the mean magnetic energy density is

$$\frac{1}{2}\langle B^2\rangle = \frac{1}{2}\langle B\rangle^2 + \frac{1}{2}\sum_{\substack{(m,n)\\ \neq(0,0)}} \mathbf{b}_{m,n}\cdot\mathbf{b}^*_{m,n} .$$

There is magnetic energy density associated with each mode, which evolves according to a modal Poynting equation:

$$\frac{\partial}{\partial t} b^2_{m,n} = -\frac{1}{r}\frac{\partial}{\partial r} r\left(\mathbf{e}_{m,n}\times\mathbf{b}^*_{m,n}\right)_r - \mathbf{e}_{m,n}\cdot\mathbf{j}^*_{m,n} + \text{c.c.}\,, \qquad (3.2)$$

except for the mean-field energy which does not have complex conjugate terms, of course:

$$\frac{1}{2}\frac{\partial}{\partial t}\langle B\rangle^2 = -\frac{1}{r}\frac{\partial}{\partial r} r\left(\langle\mathbf{E}\rangle\times\langle\mathbf{B}\rangle\right)_r - \langle\mathbf{E}\rangle\cdot\langle\mathbf{J}\rangle\,. \qquad (3.3)$$

The system does not reach a true steady-state for most cases, but when averaged over a sufficiently long period of time (a substantial fraction of τ_r), the left sides of Eqs. 3.2 and 3.3 become zero.

The ideal part of the electric field transfers energy from one Fourier component to another, coupling the system of modes. The most dramatic realization of this stems from the dynamo electric field that is induced by the fluctuations,

$$\mathbf{E}_f = \sum_{\substack{m,n\\ \neq(0,0)}} \mathbf{v}_{m,n}\times\mathbf{b}^*_{m,n}\,,$$

which is part of $\langle\mathbf{E}\rangle$ despite the lack of brackets. Fig. 3.2 shows the linear power density from $\mathbf{E}_f\cdot\langle\mathbf{J}\rangle$ for the R/a=3, S=10^4 simulation whose λ profile is shown in Fig. 2.4a. Considering the sign of the last term on the right side of Eq. 3.3, the positive region of $\mathbf{E}_f$ in the interior extracts energy from the mean field, and the negative region in the exterior adds energy. At the reversal surface (r=0.82 in this case), $\mathbf{E}_f$ balances $\eta\mathbf{J}$ to sustain the poloidal current and therefore the reversed axial field between the reversal surface and the wall. The significance of $\mathbf{E}_f$ in RFP simulations is well established (Schnack, 1985; Nebel, 1989; Kusano, 1990; and Ho, 1991).

What is less established is how the power gets from the interior to the exterior. Previous papers emphasize the nonlinear interactions that transfer energy from modes resonant in the interior to modes resonant near or at the reversal surface (Kusano, 1987; Holmes, 1988; and Ho, 1991). This is certainly an important part of the power flow, but from Eqs. 3.2 and 3.3, it is clear that a Poynting flux is

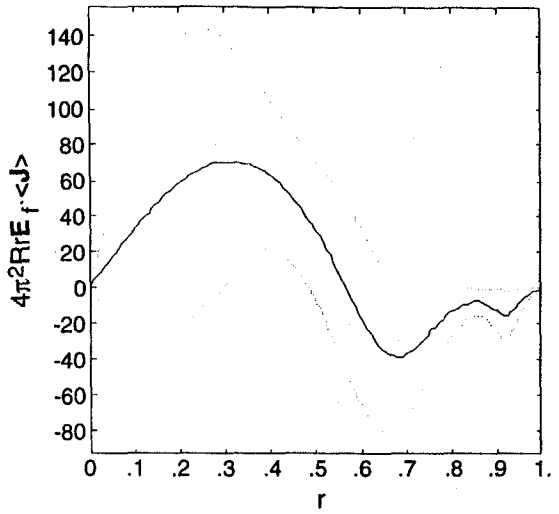

Figure 3.2 Linear dynamo power density for the $S=10^4$, R/a=3 simulation discussed in Section 2.1. The solid line is the temporal average and the dotted lines are one standard deviation above and below the average.

necessary to move magnetic energy from one radius to another. The Poynting flux in Eq. 3.3 is similar to that in the paramagnetic pinch. However, the Poynting flux in Eq. 3.2 is induced by the fluctuating fields (Tsui, 1988). The fluctuation-induced Poynting flux in the simulation is shown in Fig. 3.3. The total power input is approximately 150, so the fluctuations reflect 8-9% of the power outward against the $\langle \mathbf{E} \rangle \times \langle \mathbf{B} \rangle$ Poynting flux. This effectively produces an electromagnetic energy 'transport.' Fig. 3.3 also shows the contributions from the different azimuthal mode numbers. The m=1 modes generate most of the flux, but the m=0 contribution is significant near the reversal surface. In Fig. 3.4a, the Poynting flux from the m=1, $-9 \le n \le -6$ modes is displayed mode-by-mode, and Fig. 3.4b shows the

corresponding contributions to $\mathbf{E}_f \cdot \langle \mathbf{J} \rangle$. The picture that emerges is a poorly organized 'bucket brigade' of individual modes, passing energy across their respective resonance surfaces. Some of the energy is dissipated, but a substantial part is returned to the mean parallel current at and around the reversal surface, where a large number of modes are resonant.

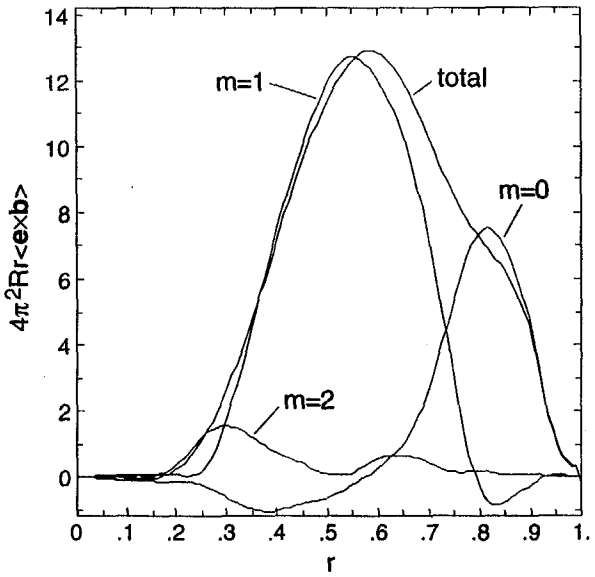

Figure 3.3 Radial fluctuation-induced Poynting flux from each azimuthal mode number. The plots are the average of eight data sets that are equally spaced in computational cycle number, so they are only approximate temporal averages.

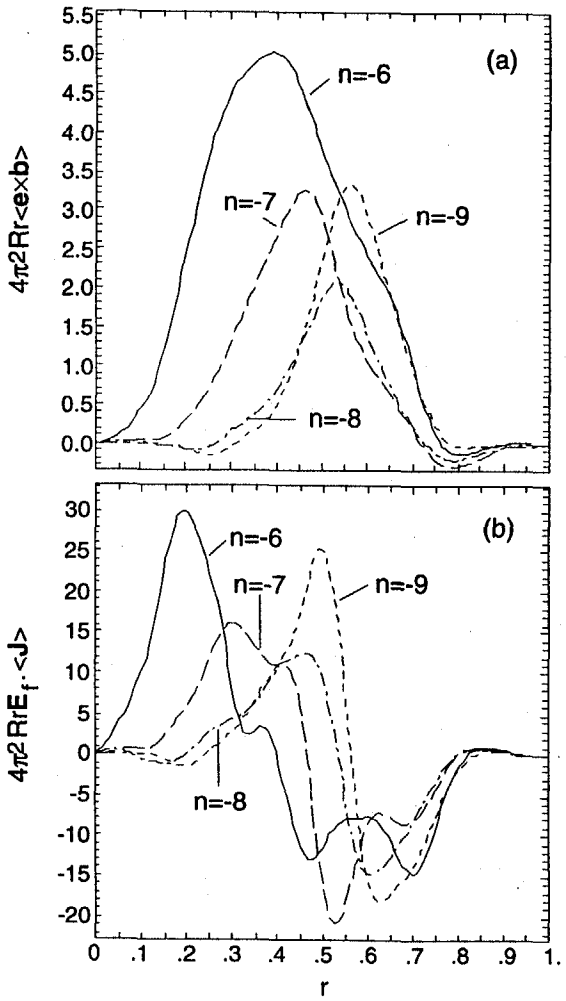

Figure 3.4 (a) Radial Poynting flux and (b) dynamo power density for the largest m=1 modes that remain resonant. The information is the average of eight data sets.

Another characteristic of fluctuation-induced Poynting flux is that it results from quasi-linear or self-interaction terms. To illustrate this point, consider that the electric field for a given mode may be written as

$$\mathbf{e}_{m,n} = -S\mathbf{v}_{m,n}\times\langle\mathbf{B}\rangle - S\langle\mathbf{V}\rangle\times\mathbf{b}_{m,n} - S(\mathbf{v}\times\mathbf{b})_{m,n} + \eta\mathbf{j}_{m,n}\,, \tag{3.4}$$

where the third term on the right side represents the sum of all nonlinear products that match the (m,n) spatial dependence. The second term is usually small, because it represents the contribution from the mean pinch. [Most other drift mechanisms that would lead to mean flow in the azimuthal and axial directions are not represented in the simulations.] Fig. 3.5 shows the total Poynting flux and that from the first term alone for the m=0 and m=1 groups. Clearly, this is the dominant term, and its radial component, $Sv_{r_{m,n}}\left(\mathbf{b}^{*}_{m,n}\cdot\langle\mathbf{B}\rangle\right)$, represents the net advection of nonuniform magnetic energy density.

The significance of the quasilinear terms does not detract from the importance of nonlinear interactions. These interactions sustain modes that would otherwise be linearly stable, especially m=0 modes and m=1 modes that are resonant near the reversal surface (Holmes, 1988 and Ho, 1991). In addition, nonlinear interactions can modify the shapes of the radial distributions of **v** and **b**, which affects the quasilinear terms (Ho, 1991). However, the nonlinear power necessary to sustain stable modes is often much smaller than the power transported by their Poynting fluxes. The behavior of these modes is somewhat analogous to a transistor—a small change in base current (nonlinear input) can lead to a large change in collector current (quasilinear transport). Since there are many of these modes that are coupled directly by nonlinear interactions and indirectly through the mean current, the temporal behavior of the system is quite dynamic. The nonlinear

interactions also excite m>1 modes. Their direct influence on the mean field is small, but they provide a nonlinear dissipation channel that helps saturate the unstable modes (Holmes, 1988).

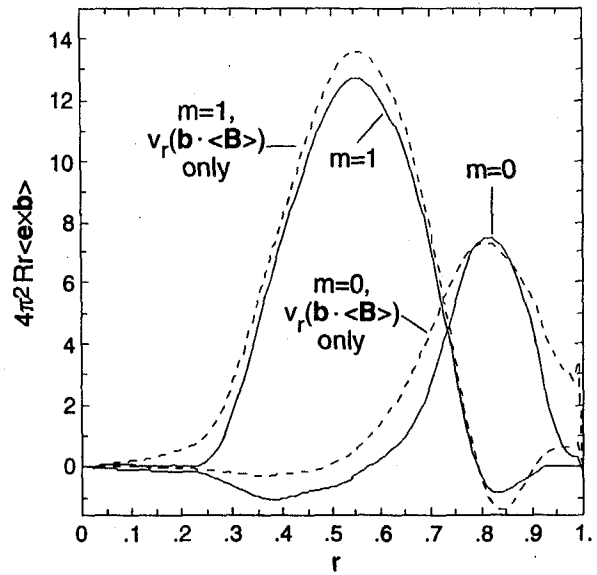

Figure 3.5 Radial Poynting fluxes induced by the m=0 and m=1 modes, and the quasilinear contributions to each (average of eight data sets).

The interactions lead to a fluctuation spectrum that is fairly broad except for a peak in the m=1 modes at the n-numbers that are resonant near the axis. The m=0 modes are usually peaked at n=1, which couples consecutive n, m=1 modes and is the least stable m=0 mode. These spectral features are shown in Fig. 3.6. The total magnetic fluctuation level is large enough to make the magnetic field stochastic over most of the plasma (see Fig. 3.7), which has also been observed in earlier simulations (Schnack, 1985 and Kusano, 1990).

To emphasize the significance of the nonlinear interactions, a simulation has been run from t=0.15 (the time at the end of the reversal parameter and energy histories in Section 2.1) with the same conditions, except all nonlinear interactions have been suppressed. There are only quasilinear interactions between the modes and the mean fields, and the advective term in Eq. 2.5 is eliminated:

$$\frac{\partial \mathbf{v}_{m,n}}{\partial t} = S\mathbf{j}_{m,n} \times \langle \mathbf{B} \rangle + S\langle \mathbf{J} \rangle \times \mathbf{b}_{m,n} + \upsilon \nabla^2 \mathbf{v}_{m,n} \tag{3.5}$$

$$\frac{\partial \mathbf{a}_{m,n}}{\partial t} = -\mathbf{e}_{m,n} = S\mathbf{v}_{m,n} \times \langle \mathbf{B} \rangle + S\langle \mathbf{V} \rangle \times \mathbf{b}_{m,n} - \eta \mathbf{j}_{m,n} \tag{3.6}$$

for all but the mean fields, and

$$\frac{\partial \langle \mathbf{V} \rangle}{\partial t} = S\sum_{m,n} \mathbf{j}_{m,n} \times \mathbf{b}^*_{m,n} + \upsilon \nabla^2 \langle \mathbf{V} \rangle \tag{3.7}$$

$$\frac{\partial \langle \mathbf{A} \rangle}{\partial t} = -\langle \mathbf{E} \rangle = S\sum_{m,n} \mathbf{v}_{m,n} \times \mathbf{b}^*_{m,n} - \eta \langle \mathbf{J} \rangle . \tag{3.8}$$

The impact is dramatic. All but the interior m=1 modes are stabilized, and the (1,-7) mode becomes larger without the nonlinear saturation mechanisms (see Fig. 3.8). The absence of modes in the exterior leads to the loss of reversal in this case (Fig.

3.9), and the temporal oscillations disappear without the m=0 interactions—consistent with Ho, 1991. The quasilinear power transport is still active in the interior, however, and this flattens the λ profile around the resonance surfaces of the surviving m=1 modes (Fig. 3.10).

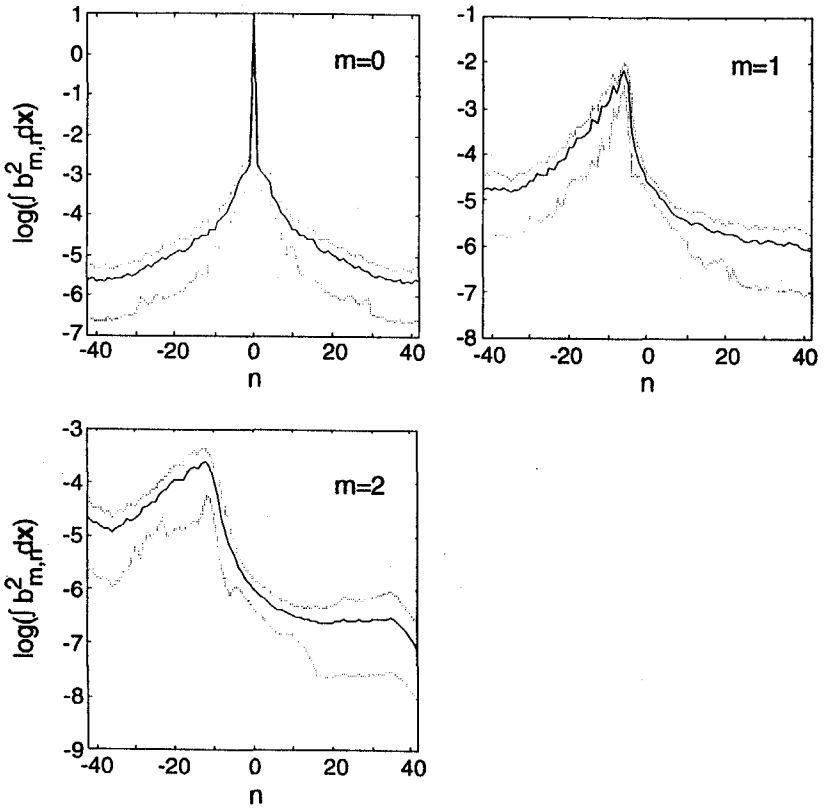

Figure 3.6 Magnetic energy spectra for the $S=10^4$, R/a=3 simulation. The solid and dotted lines show the temporal average and standard deviation, respectively.

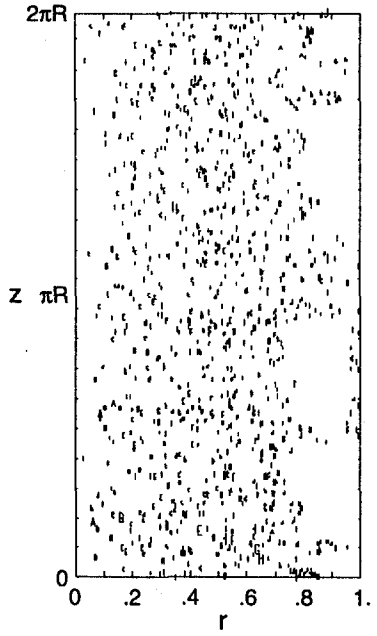

Figure 3.7 Magnetic field-line puncture plot in the r-z plane of the simulation.

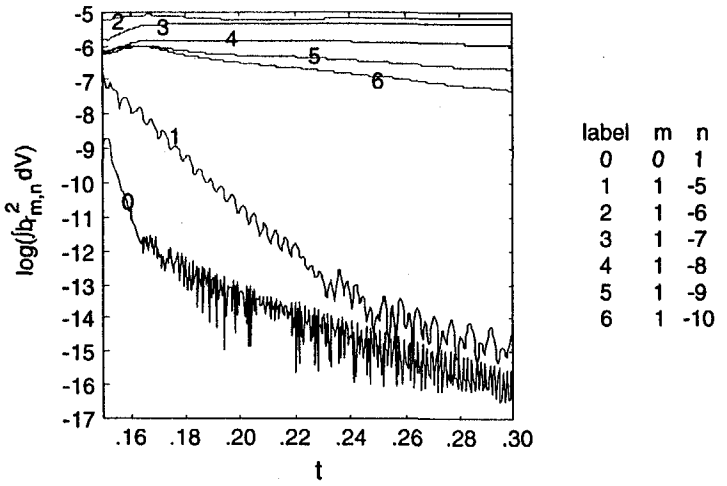

Figure 3.8 Modal magnetic energy histories (radial contribution) following the suppression of nonlinear interactions. All m=2 and the rest of the m=0 modes decay sharply.

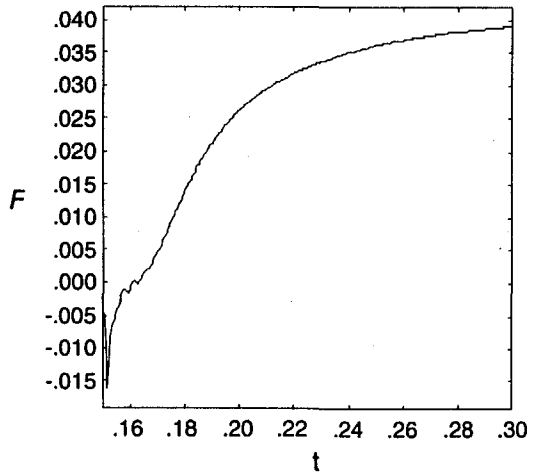

Figure 3.9 Reversal parameter following the suppression of nonlinear interactions.

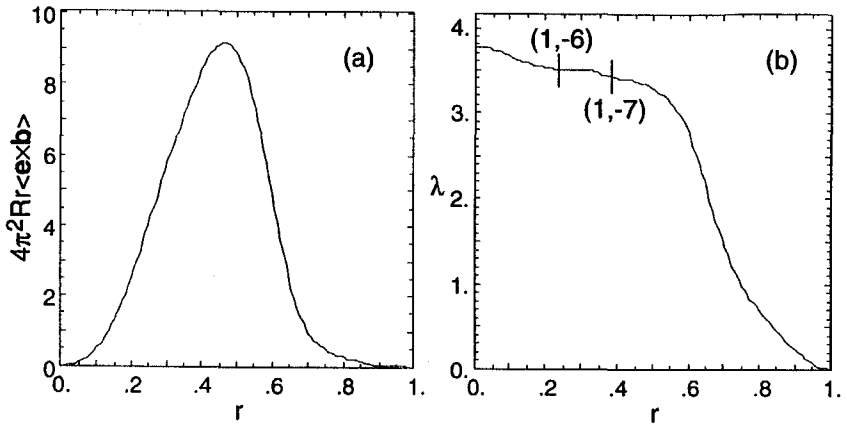

Figure 3.10 Profiles of (a) fluctuation-induced Poynting flux and (b) parallel current at t=0.30 of the simulation without nonlinear interactions. The locations of the resonance surfaces for the two largest modes are indicated in (b).

3.2 Energy Transport and Pressure Gradient Effects

When plasma pressure is evolved with the momentum equation and Ohm' law, the MHD model describes two more aspects of RFP behavior, energy transport and the pressure-gradient drive of fluctuations. The mechanisms for transport are embodied in the conductive and convective heat flows in Eq. 2.11, $-\underline{\kappa}\cdot\nabla T$ and $P\mathbf{V}$, respectively. The parallel conductivity is very large, so thermal conduction along the perturbed field-lines produces most of the heat flux. [The term $P\mathbf{V}$ would also be labeled conductive in analytic turbulence theory, because there is no density gradient in the simulations.] The modes can also tap into 'free' internal energy with

the pressure gradient term in Eq. 2.12. According to linear theory in cylindrical geometry, tearing modes are always unstable whenever $\partial\langle P\rangle/\partial r < 0$, regardless of mode number or Δ' (Coppi, 1966). However, the largest modes are unstable without the pressure gradient, so the relevant question is, "How significant is the pressure gradient relative to the current gradient for the sustainment of the fluctuations?" This can be answered quantitatively with the simulations.

In pressureless simulations, only three dimensionless parameters are needed to specify the physical conditions: S, R/a, and the ratio (ν/η). With pressure evolution and thermal conduction, the initial β and Prandtl numbers (ν/κ) for both parallel and perpendicular conductivities are also needed. A complete set of physical parameters are selected to self-consistently simulate real plasma conditions, but the selection is limited by the numerical implications of the Lundquist number. The parameter that appears in the normalized equation is based on the initial conditions,

$$S = \frac{\mu_0 a B_0}{\eta_0 \sqrt{\mu_0 \rho}},$$

and it is a constant along with ν. However, the temperature is a dependent variable, and with Spitzer resistivity, the actual Lundquist number is proportional to $T^{3/2}$. Of the three parameters a, B_0, and ρ, the density seems to be the most tractable for controlling the final result. As ρ is increased, S is reduced, and the specific heat capacity increases, which keeps T from becoming large. The simulation described here has $\rho=8\times10^{-9}$ kg/m^3, a=0.1 m, B_0=0.05 T, and ν=0.5. The initial temperature on axis (T_0) is 10 eV, so β_0=1.6% and $\kappa_\parallel/\kappa_\perp = 1.4\times10^5$ at B_0 and T_0.

The aspect ratio is given a small value of 1.25. In pressureless simulations, the fluctuation spectrum narrows as R/a is decreased, but the total fluctuation level remains fairly constant (Ho, 1995). Including pressure should not change these properties at low β, so the small aspect ratio allows less toroidal resolution. The computer resources are instead used for better poloidal resolution, ensuring accuracy for the mode coupling produced by the anisotropic thermal conduction. The simulation discussed here resolves modes with $0\le m\le5$ and $-21\le n\le21$. The safety factor is large on axis, so the resonance surfaces of the internal m=1 modes are well-separated relative to cases with larger R/a values.

The simulation is initiated from a paramagnetic equilibrium with nonzero pressure:

$$\langle \mathbf{J}\rangle \times \langle \mathbf{B}\rangle = \frac{\beta_0}{2}\frac{\partial\langle P\rangle}{\partial r},$$

$$\langle V_r\rangle = -\frac{\langle E_z\rangle\langle B_\theta\rangle + \eta\frac{\beta_0}{2}\frac{\partial\langle P\rangle}{\partial r}}{S\langle B\rangle^2},$$

and the parallel current profile is determined by the parallel component of Ohm's law. The initial pressure distribution is arbitrary, and I have used $\langle P\rangle$=1-0.9r^3.

Once the simulation is started, perturbations grow linearly then saturate while generating reversal, like the pressureless cases. The pinch parameter (Θ) is 1.8, which produces β=4% on axis, and β_p=22%, where

$$\beta_p \equiv \beta_0 \frac{2\int_0^1 \langle P\rangle r dr}{\langle B_\theta(r=1)\rangle^2}.$$

The resulting Lundquist number is 5500 on axis, so the radial resolution of 125 cells leaves a margin for improvement when current profile modification is applied. The parallel current, safety factor, and dynamo power density profiles in the quasi-steady state (see Fig. 3.12) are all similar to pressureless results. The (1,-3) is the first mode that is always resonant, and it has a pronounced effect on the parallel current profile. This is due to the small aspect ratio, hence poor coupling, and is not unlike the quasilinear result in the previous section (Fig. 3.11b).

The radial component of the magnetic field fluctuations allows radial heat flow via the large parallel conductivity. Energy transport due to fluctuating parallel conduction is determined by the correlation, $\langle q_{\langle B\rangle} b_r \rangle \langle B\rangle^{-1}$, where $q_{\langle B\rangle}$ is the component of the heat conduction vector in Eq. 2.11 that is parallel to $\langle \mathbf{B} \rangle$. This correlation is plotted in Fig. 3.13 for individual modes at the end of the simulation. The thermal energy transport allowed by each mode is localized near the respective resonance surface, or near the axis for the nonresonant (1,2) mode, despite the global extent of the b_r eigenfunctions. The fine-scale structure of the correlations changes in time, but the centering of each is relatively constant.

These modal contributions dominate the total thermal conduction and the total heat flux within $r \cong 0.85$, as shown in Fig. 3.14. The convection has a relatively small effect. The mean inward pinch convects thermal energy towards the axis and is larger than any fluctuation-induced convection. For $r>0.85$, the radial component of magnetic fluctuations becomes small due to the conducting wall, and perpendicular conduction completes the transport. The aggregate heat flux leads

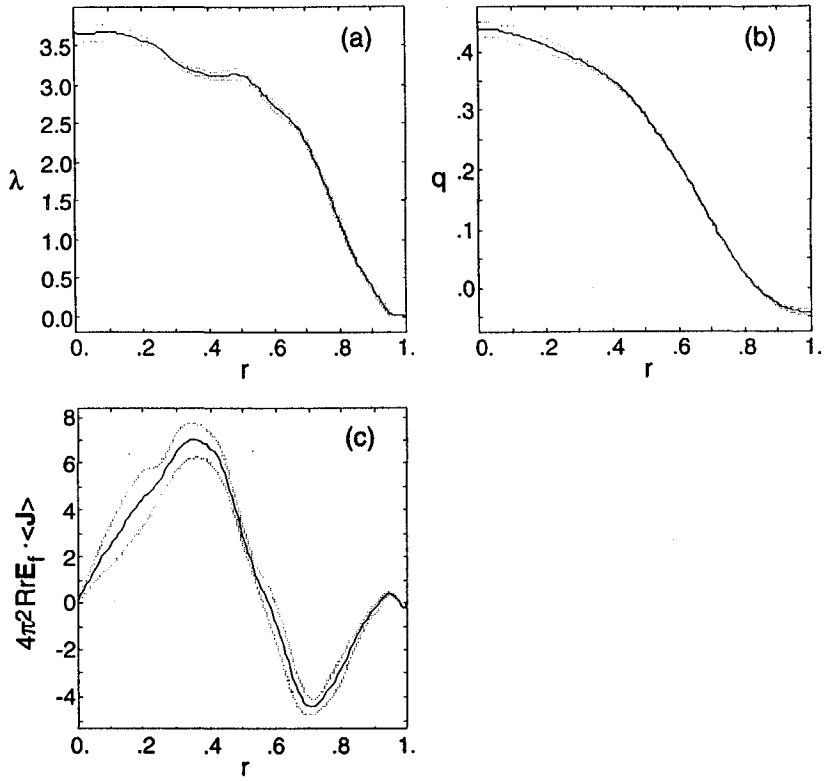

Figure 3.12 Radial profiles of (a) parallel current, (b) safety factor, and (c) dynamo power density for the finite pressure, R/a=1.25 simulation. The solid line is the time average over 0.2 τ_r, and the dotted lines are one standard deviation above and below the average.

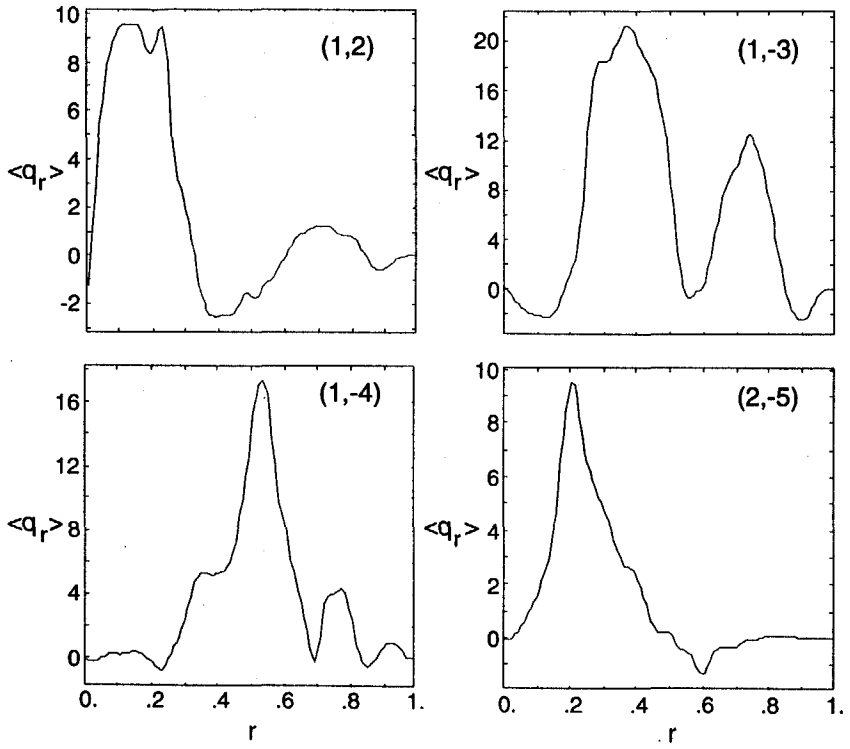

Figure 3.13 Typical profiles of radial heat conduction resulting from magnetic fluctuations for the indicated modes, $\left\langle q_{r_{m,n}} \right\rangle = \left(q_{\langle B \rangle_{m,n}} b^*_{r_{m,n}} + \text{c.c.} \right) \langle B \rangle^{-1}$.

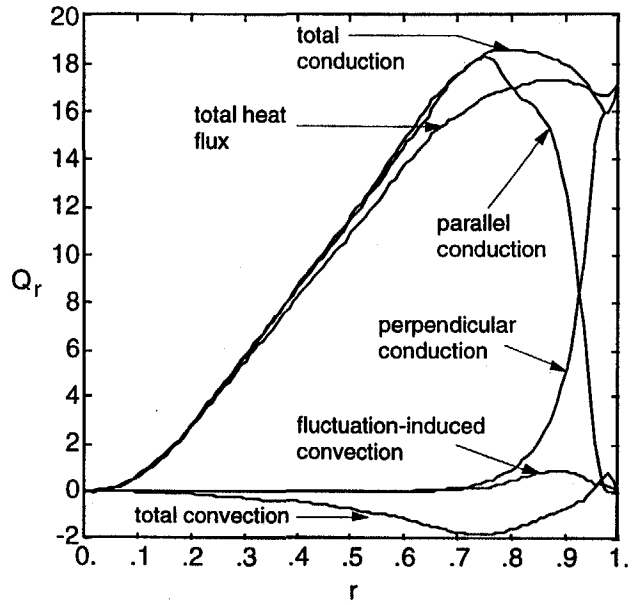

Figure 3.14 Decomposition of internal energy transport at the time shown in Fig. 3.13: $Q_r = 2\pi^2 r R \beta_0 (\gamma - 1)^{-1} h_r$, where h_r is $\langle q_r \rangle$ for conduction and $S\langle PV_r \rangle$ for convection. The parallel conduction is the sum of all modal contributions to $\left\langle q_{\langle B \rangle} b_r \right\rangle \langle B \rangle^{-1}$, and the fluctuation-induced convection is the sum of $S\langle pv_r \rangle$.

to a temperature profile that is flat in the interior with a large gradient for r>0.8 (see Fig. 3.15). The effective thermal diffusivity,

$$\chi_e \equiv -\frac{\langle q_r \rangle + S\langle PV_r \rangle}{\frac{\partial \langle T \rangle}{\partial r}},$$

is large where the interior modes are resonant and falls to the perpendicular conductivity near the wall. Therefore, only a small portion of the magnetic configuration provides thermal insulation for the plasma.

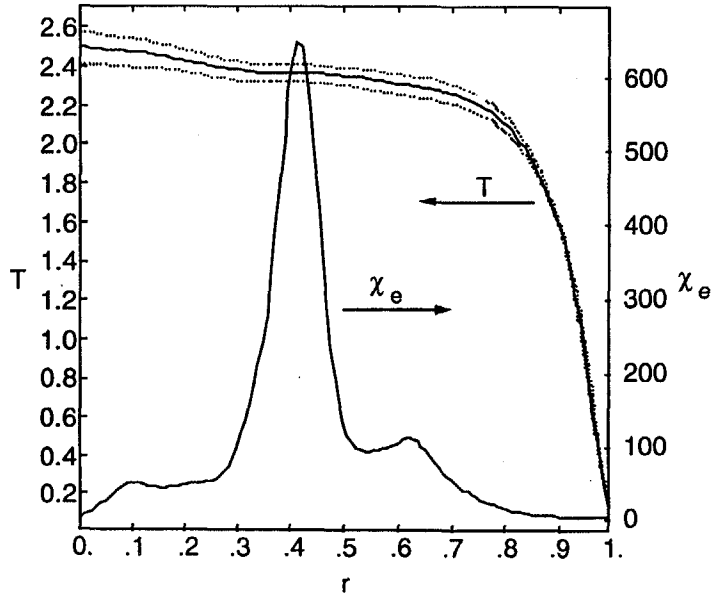

Figure 3.15 Radial profiles of mean temperature and effective thermal diffusivity, χ_e. The time average and standard deviation are plotted for $\langle T \rangle$, and χ_e is based on the average total thermal energy flux and the average temperature profile. The temperature is units of T_0 (10eV), and χ_e is in units of a^2/τ_r.

The significance of the parallel heat fluctuations is consistent with recent experimental measurements on MST (Fiksel, 1994); there is even agreement on the r=0.85 location, where the resulting transport ends. However, other measurements prove the importance of physical processes that are not in the MHD model. Stoneking has shown that fast electrons are transported along magnetic fluctuations inside $r/a \cong 0.85$ (Stoneking, 1994b). Furthermore, the product of the fast electron particle flux and internal energy density gives a convective heat flux that is consistent with the total heat flux measured by Fiksel (Stoneking, 1994a). This cannot be represented by the fluid convection in DEBS. A more detailed treatment would address convection from the electrons and ions separately, and modeling kinetic effects is far more complicated.

Using the Braginskii conductivity matrix elements is also not formally correct. The derivation assumes that the magnetic fields vary slowly in space, relative to particle mean free paths (Braginskii, 1965). In RFP plasmas, this condition is violated. The simulation discussed in this section has a core temperature of 25eV in the quasi-steady state, and the electron collisional mean free path (λ_e) is approximately 30a. This should be compared with the correlation length (L_c) for the magnetic fields. The Rechester-Rosenbluth formulation is $L_c = \pi R/\ln(\pi s/2)$, where s is the stochasticity parameter,

$$s = \frac{1}{2}\frac{\left(\Delta_{m,n} + \Delta_{m',n'}\right)}{\left|r_{m,n} - r_{m',n'}\right|},$$

$r_{m,n}$ and $r_{m',n'}$ are the resonance surfaces of two adjacent modes (Rechester, 1978), and $\Delta_{m,n}$ is the island width for the (m,n) mode,

$$\Delta_{m,n} = 4\left[\frac{R}{m}\left|\frac{b_{r_{m,n}}}{\langle B_z\rangle}\right|\left.\frac{q^2}{dq/dr}\right|_{r=r_{m,n}}\right]^{1/2}$$

(Rechester, 1976). Using the simulation results for the (1,-3) and (1,-4) modes that are resonant at r=0.45 and 0.55, gives $L_c \cong 2a$. Since this is much smaller than λ_e, the step-size in a random-walk diffusion process is determined by magnetic fluctuations and not particle collisions.

The thermal diffusivity in plasmas with collisional mean free paths that are much longer than the magnetic field correlation length remains an area of active research. Krommes reviews several theories for test particle diffusion in stochastic field configurations, where the field is assumed to be independent of particle motion (Krommes, 1983). In the collisionless limit, the Rechester-Rosenbluth diffusivity is appropriate: $\chi_r = D_{st} v_{te}$, where v_{te} is the electron thermal velocity, and $D_{st} = \pi R |b_r|^2 / \langle B \rangle^2$ with b_r determined by the locally resonant modes (Rechester, 1978). Experimental results show that the effective *particle* diffusivity just inside the reversal surface in MST can be related to χ_r when the ion thermal velocity is used in place of v_{te} (Stoneking, 1994a). Since the convective heat flux is consistent with the total heat flux, the effective thermal diffusivity is much smaller than the χ_r prediction—assuming the scale lengths for temperature and density are the same. Terry has recently developed an analytic turbulence theory that self-consistently models the heat flux and the response of the fields due to particle motion. He shows that there are ambipolar constraints on the electron heat flux, resulting in smaller effective diffusivities that are consistent with experiment (Terry, 1995). While it is possible to use an effective diffusivity from analytic theory in DEBS, it would be inconsistent with the local nature of the MHD equations. Thus, the fluid

thermal conductivities are applied for lack of a better approach at present, and results must be viewed in light of this simplification.

A comparison of χ_e from the simulation and the Rechester-Rosenbluth χ_r puts the simulation result into context. For the parameters and numerical fluctuation level in the vicinity of the (1,-3) resonance surface, $\chi_r \cong 90\, a^2/\tau_r$. Fig. 3.15 shows that χ_e, which involves the fluid parallel conductivity, exceeds this by a factor of seven. Thus, to the degree of accuracy in all of the estimates, $\chi_e \sim \chi_r \lambda_e / L_c$. If this holds at MST parameters, then the fluid model produces an effective diffusivity that is a factor of $\sqrt{m_p/m_e}\,(\lambda_e/L_c)$ larger than what has been observed. A more detailed numerical model with kinetic effects is likely necessary to accurately reproduce the experimental results. However, to the extent that the transport is related to b_r, the MHD simulations are valuable. They allow us to study the relative change in transport and other behavior that results when current profile modifications are applied (see Chapter 4).

Including thermal energy transport completes the flow of power through the MHD system. The Poynting vector from the applied potential and the mean magnetic field brings electromagnetic energy to the interior, though some is reflected by the fluctuations. It sustains current against Ohmic dissipation, generating plasma internal energy. The fluctuations allow heat to escape to the reversal surface, and near the wall a large temperature gradient maintains the conduction. The energy transit time for a cylindrical volume of radius r is

$$\tau_E(r) \equiv \frac{2\int_0^r \langle P(r')\rangle r' dr'}{r\left(\langle q_r(r)\rangle + S\langle P(r)V_r(r)\rangle\right)}.$$

Its profile—shown in Figure 3.16—summarizes the thermal part of the power flow. Ohmic heating is largest at the axis, where the current density is largest (η is approximately constant in the interior), so the total heat flux (denominator) has a dependence that is weaker than r^2 (see Fig. 3.14). However, the internal energy within a given radius (numerator) has an r^2-dependence, because the large χ_e produces a flat temperature profile. Thus, τ_E increases with r, and at the wall it is equivalent to the energy confinement time for the system.

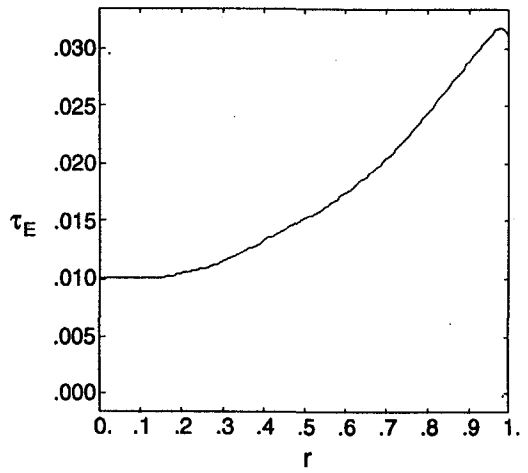

Figure 3.16 Internal energy turnover time for cylindrical volumes coaxial with the wall and extending from the axis to some radius r.

The significance of the pressure-drive for sustaining fluctuations may be examined by considering the modal kinetic energy equation, which is the scalar product of $\mathbf{v}_{m,n}$ and Eq. 2.12,

$$\frac{\partial v_{m,n}^2}{\partial t} = S\mathbf{v}_{m,n}\cdot\left(\frac{1}{2}V^2\right)^*_{m,n} + S\mathbf{v}_{m,n}\cdot(\mathbf{J}\times\mathbf{B})^*_{m,n} - S\frac{\beta_0}{2}\mathbf{v}_{m,n}\cdot\nabla p^*_{m,n} + \text{c.c.}\,. \qquad (3.9)$$

The third term is the pressure-gradient drive, though the mean pressure gradient does not appear directly. Note that the second term contains

$$\mathbf{v}_{m,n}\cdot\left(\langle\mathbf{J}\rangle\times\mathbf{b}^*_{m,n}\right) = -\left(\mathbf{v}_{m,n}\times\mathbf{b}^*_{m,n}\right)\cdot\langle\mathbf{J}\rangle\,,$$

which is the mode's contribution to $\mathbf{E}_f\cdot\langle\mathbf{J}\rangle$ and leads to the current-gradient drive associated with this particular mode. The importance of the pressure may therefore be assessed by comparing $S(\beta_0/2)\int\langle\mathbf{v}\cdot\nabla p\rangle d\mathbf{x}$ with $\int\mathbf{E}_f\cdot\langle\mathbf{J}\rangle d\mathbf{x}$.

The contributions to these two integrals are grouped by poloidal mode number and compared in Fig. 3.17 for the quasi-steady state of the simulation. The current gradient is the dominant source of power for the m=1 modes, but the two integrals are nearly equal for the m=0 modes. As discussed in Section 3.1, interior m=1 modes are sustained at large amplitude by the current gradient alone. The fluctuation-induced transport keeps the pressure profile (equivalent to the temperature profile, Fig. 3.15) flat in the vicinity of their resonance surfaces, which minimizes any pressure-gradient drive. In contrast, the m=0 modes are not sustained at large amplitude by the current gradient. Energy transport near their resonance surface (r=0.83) is therefore small, so the pressure gradient and its influence on the m=0 modes is large.

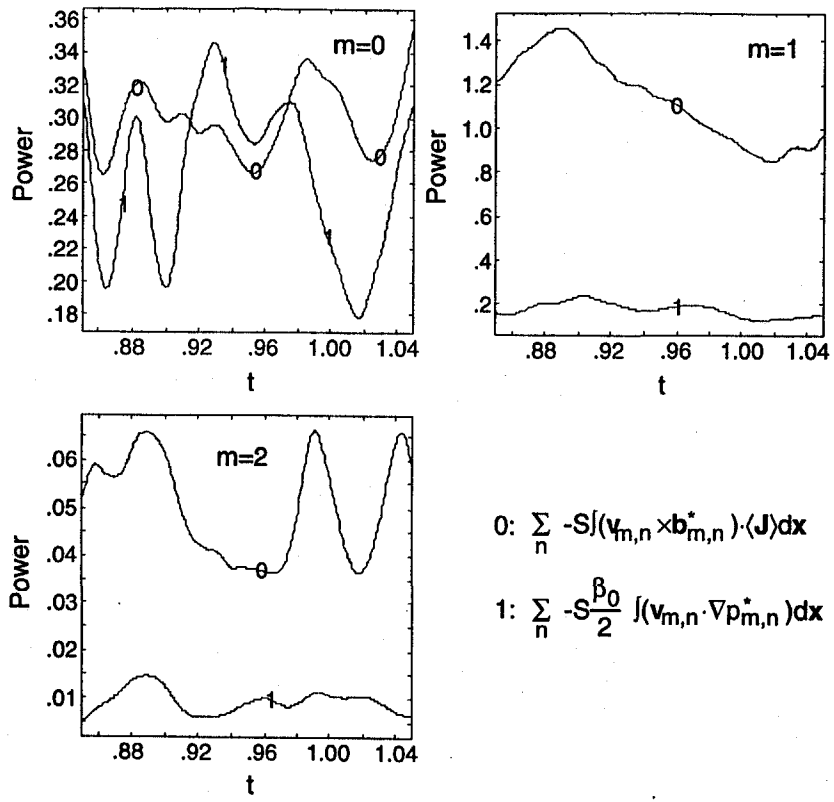

Figure 3.17 Comparison of power flowing into poloidal mode groups from the magnetic field and from pressure.

3.3 Nonlinear S-scaling for RFPs

Since the magnetic fluctuations play such an important role in energy transport, any attempt to improve RFP confinement must address the MHD activity. Using additional current drive is one possible approach (see Chapter 4), but the fluctuation level may also decrease naturally as the plasma temperature is increased. The linear growth rate of the tearing mode scales as a fractional power of resistivity, so less resistive plasmas are more stable, suggesting smaller saturation levels. However, other factors also change as the resistivity is decreased. Nonlinear coupling becomes more important as the scale-length for dissipation decreases. In addition, the parallel current profile depends on the dynamo, so mean-field profile effects are coupled with fluctuation level changes.

To examine the scaling of the nonlinear system, I have used the DEBS code to run a series of simulations with S from 2.5×10^3 to 4×10^4. Pressure is not evolved, so the results are applicable to low-β plasmas, where fluctuations are driven by the current gradient and not the pressure gradient. To reduce the required CPU time, the hyper-dissipation terms have been employed with a reduction in radial resolution. I have shown that the resolution may be halved with the hyper-dissipation terms, while preserving fluctuation level accuracy to within 3% (see Section 2.1.2). Here, a conservative reduction of one-fourth is used. The radial mesh spacing ranges from 2.2×10^{-2} for the lowest-S case to 5.3×10^{-3} for the largest S. The normalized coefficient ζ has the same value of 1×10^{-4} for all S. In physical units, it scales with the actual resistivity and viscosity, and this prevents disproportionate changes in the significance of the hyper-dissipation as S is varied.

Other parameters are typical of RFP simulations. In all cases R/a=2.5, and the axial flux (Φ) is conserved. The normalized resistivity profile is $\eta(r)=(1+9r^{30})^2$, and

the velocity at the wall is the radial $\langle \mathbf{E} \rangle \times \langle \mathbf{B} \rangle$ drift. The mean axial electric field at the wall is adjusted to keep Θ=1.657 on average:

$$\frac{1}{2\Phi}\frac{d}{dt}\langle E_z(r=1)\rangle = -10^5(\Theta - 1.657) - 50\frac{d\Theta}{dt}, \qquad (3.9)$$

where the second term on the right prevents E_z from changing too rapidly. The simulations resolve axial modes -42≤n≤42 and azimuthal modes 0≤m≤2. The azimuthal resolution is marginal. Holmes has shown that m>1 modes provide a dissipation channel for the fluctuations, and though m=2 modes are much smaller than m=1 modes, the decrease with m is weaker thereafter (Holmes, 1988). The lack of better azimuthal resolution therefore limits this dissipation channel. When the S=5000 simulation is performed with 0≤m≤5, the m=2 energy decreases by 25%, but the energy in all m≥2 modes increases by 20%. In addition, the m=0 energy drops by a factor of two, and the degree of reversal is reduced by 30%, so the dynamo is enhanced when poloidal resolution is insufficient. Nonetheless, the m>2 modes do not provide anything unique to the system, so I have chosen to expend available computational resources on extending the scaling to larger S instead of using better poloidal resolution.

Even with the hyper-dissipation terms and the reduced poloidal resolution, the range of S is limited to small values relative to present-day experiments—in MST for example, $S \cong 10^6$. Furthermore, linear calculations from initial-value simulations show that growth rates are only approaching their asymptotic behavior in this range (Li, 1995), so the S-scaling computed here may not be accurate for the large-S limit. However, the difference between the computed scaling and the large-S limit can be inferred. In addition, the simulations show spectrum changes

and the emergence of periodic oscillations, which are significant results in themselves.

The simulation results for the total fluctuation level and the magnetic fluctuation energy for each poloidal-mode group are plotted in Fig. 3.18. The m=1 and m=2 energies decrease with S, and the m=0 energy increases. When the groups are added together, the total fluctuation level decreases, but the $S^{-.18}$ dependence is weak. If the m=0 modes were negligible, the dependence would be much stronger. The m=1 energy decreases with an $S^{-.62}$ dependence, so the rms(b) scaling would be closer to $S^{-.3}$. The m=0 modes are not negligible, however; at $S=4\times10^4$, there is more energy in the m=0 modes than there is in the m=1 modes. Furthermore, the modes are resonant in different parts of the radial domain, so the fluctuation reduction relative to the mean field magnitude occurs mostly in the interior. Figure 3.19 illustrates the spectrum change. The peak of the m=1 modes decreases as S is increased, which is consistent with the linear growth rate dependence for unstable modes. In contrast, the large |n| modes increase with S for all m, and the (0,1) mode is nearly an order of magnitude larger at $S=4\times10^4$ than at $S=2.5\times10^3$. This reflects the enhanced nonlinear coupling that results when dissipation is reduced.

The parallel current profile also changes as S is increased. The current density is reduced on axis, but it is increased at r≅0.65 and at r≅0.85 (see Fig. 3.20a). The change in the safety factor profile reflects the current redistribution and shows that there is more reversal as S is increased (Fig. 3.20b). A comparison of the dynamo electric field is shown in Fig 3.21, and the cause of the current profile change is evident. The magnitude of $\mathbf{E}_f$ is larger in the interior and near the wall, so the dynamo transports more power as S is increased. The enhanced $\mathbf{E}_f$ in the interior results from the m=1 modes, which become more effective at collecting power from

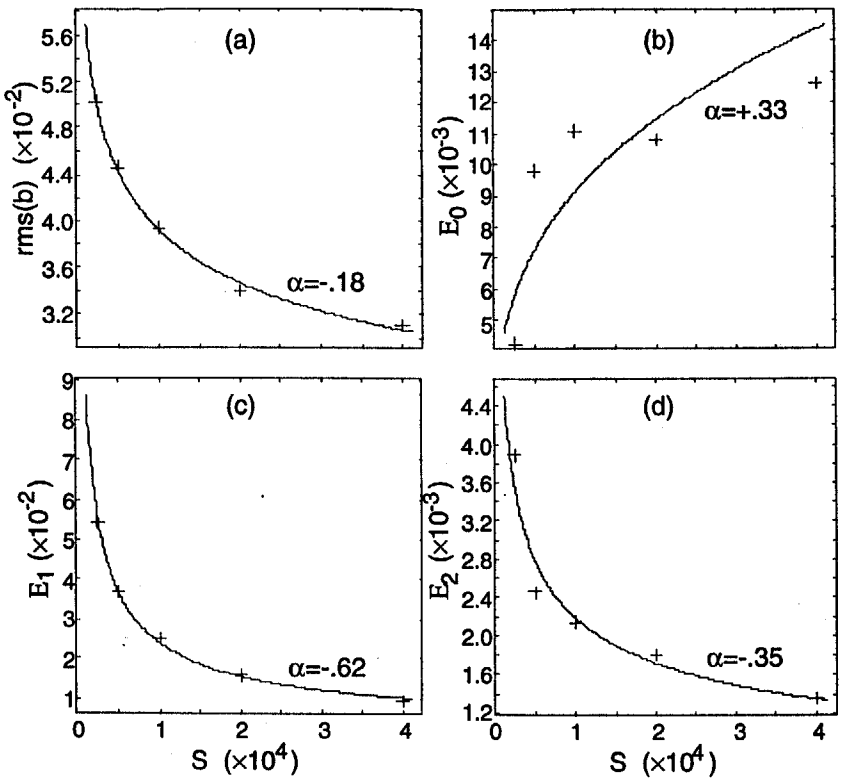

Figure 3.18 S-dependence of (a) the total magnetic fluctuation level and (b)-(d) the magnetic energy grouped by poloidal mode number; $E_m \equiv \frac{1}{2}\sum_n\left(\int b_{m,n}^2 dx + c.c.\right)$. The crosses are the time-averaged simulation results, and the solid lines show least-squares fits to lnC+αlnS, where α and C are the fitted parameters. The positive m=0 energy scaling cannot continue indefinitely, and the best fit—shown in (b)—is poor.

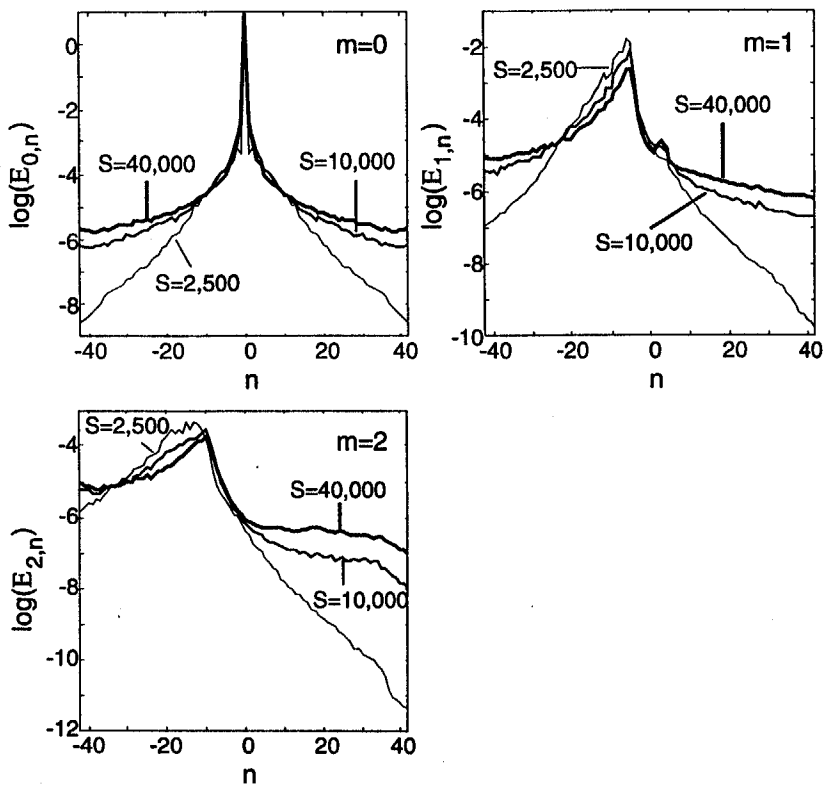

Figure 3.19 Time-averaged magnetic energy spectra grouped by poloidal mode number; $E_{m,n} \equiv \frac{1}{2}\left(\int b_{m,n}^2 dx + c.c.\right)$, except for m=0 where the complex conjugate energies are displayed separately.

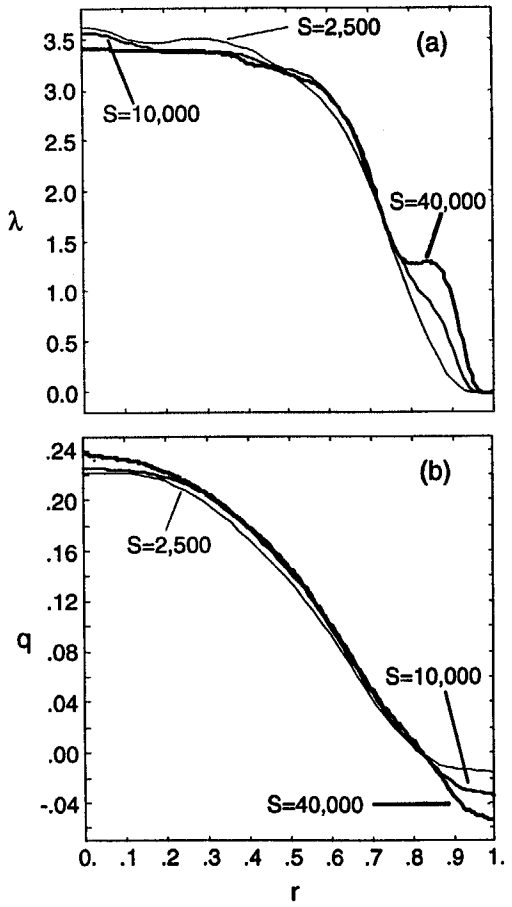

Figure 3.20 Time-averaged profiles of (a) parallel current and (b) safety factor. The difference in $\langle B_z(r=1)\rangle$ for the three cases is evident in (b) and in the reversal parameter (F=-.066, -.14, and -.23 for S=2.5×10^3, 1×10^4, and 4×10^4, respectively).

the mean current despite the fact that their magnitudes are reduced. The enhanced $\mathbf{E}_f$ in 0.8≤r<0.9 is due to the m=0 modes that are resonant at the reversal surface (r=0.8). They are excited by the nonlinear coupling and the current gradient at r≅0.7, both of which increase with S.

While the dynamo becomes stronger, the fraction of power dissipated by the fluctuations also increases. The power input and ohmic dissipation from mean current is listed in Table 3.1 for each simulation. The 'anomalous' power—related to 'anomalous' loop voltage in experiments—is the difference between them, and it is an increasing fraction of the input power as S is increased. The increase is dissipated through normal viscosity and the hyper-dissipation terms. Since larger |n| modes are excited, more of this occurs through nonlinear mode coupling, but dissipation from the largest m=0 and m=1 modes still dominates.

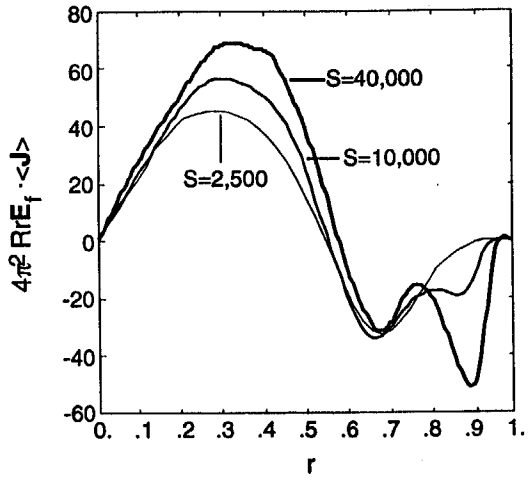

Figure 3.21 Time-averaged profiles of dynamo power density.

Table 3.1 Time-averaged powers from the simulations in the S-scaling study.

S ($\times 10^3$)	$V_L I$	$\int \eta \langle J \rangle^2 dx$	$\int \mathbf{E}_f \cdot \langle \mathbf{J} \rangle dx$	% anom.	$\int \eta j^2 dx$	$\int \mathbf{V} \cdot \nu \nabla^2 \mathbf{V} dx$	hyper-dissip.
2.5	145	135	9.6	6.9	7.6	1.9	0.47
5	142	131	11.2	7.8	7.6	3.0	0.61
10	143	131	11.9	8.4	7.7	3.0	0.85
20	144	131	13.2	9.0	8.1	3.4	1.33
40	146	131	15.0	10.3	8.0	3.8	2.14

The large-S limit will likely have a stronger scaling than what has been observed in the simulations, due to stronger linear scaling and quasilinear profile effects. The significance of the latter is inferred from Fig. 3.20a. The average parallel current within r=0.5 is fairly uniform at $S=4\times10^4$, so the profile effects are approaching saturation for the internally resonant, m=1 modes. In contrast, the m=0 modes are producing great changes in the current profile over this range. This should saturate when the average profile is flattened through the reversal surface. Externally resonant m=1 modes, i.e., n>0, may be excited at this point, but any further profile flattening will oppose the applied axial field, so it should be weak. In this scenario, the m=0 and m=1 energies both decay at large S, and the total fluctuation energy scales at a rate closer to what has been observed for the m=1 modes.

The temporal behavior of the simulations also changes over the range of S that has been scanned. At low S, there are weak oscillations in the reversal parameter

(see Fig. 3.22), but at large S, the oscillations are strong and regular with the sharp drop and gradual recovery of the 'sawteeth' observed in MST (Beckstead, 1990) and elsewhere. The oscillation period is approximately 0.03 for all of the simulations. This likely results from the diffusion of a mean current gradient, because the profiles all have the same general shape, so the diffusion rate is independent of S for time in units of τ_r. The evolution of the modes for the largest- and smallest-S cases is shown in Fig. 3.23. At $S=2.5\times10^3$, the temporal behavior is random with different m=1 modes being largest at different times. At $S=4\times10^4$, the largest m=1 modes drop as F is reduced and begin growing 0.01 τ_r later. The m=0 modes decay for a longer period of time and do not grow until the largest m=1 modes have nearly peaked. The (1,-4) mode is only resonant when the dynamo is most active and F is near its minimum value. This mode and the m=2 modes (not shown) follow the m=0 behavior also.

The reversal parameter for a comparable $\Theta \cong 1.64$ discharge in MST is shown in Fig. 3.24. The plot covers slightly more than two sawtooth periods, and the defining drops are evident. Shortly after recovery begins, there is a noticeable decrease in slope, which is not observed in the simulations. The time between sawteeth is also shorter on a resistive time-scale; in MST τ_r~0.5 s, so the period is less than $0.01\tau_r$. This may result from the external electrical circuit that controls the toroidal field at the wall. There is a 1-10ms L/R decay time for induced shell current as toroidal flux is exchanged between the plasma and external inductance. This is not modeled in the simulations, where boundary conditions represent a perfectly conducting wall. In addition, energy transport increases during each crash, which may produce resistivity changes. Capturing this effect would require the finite-pressure code.

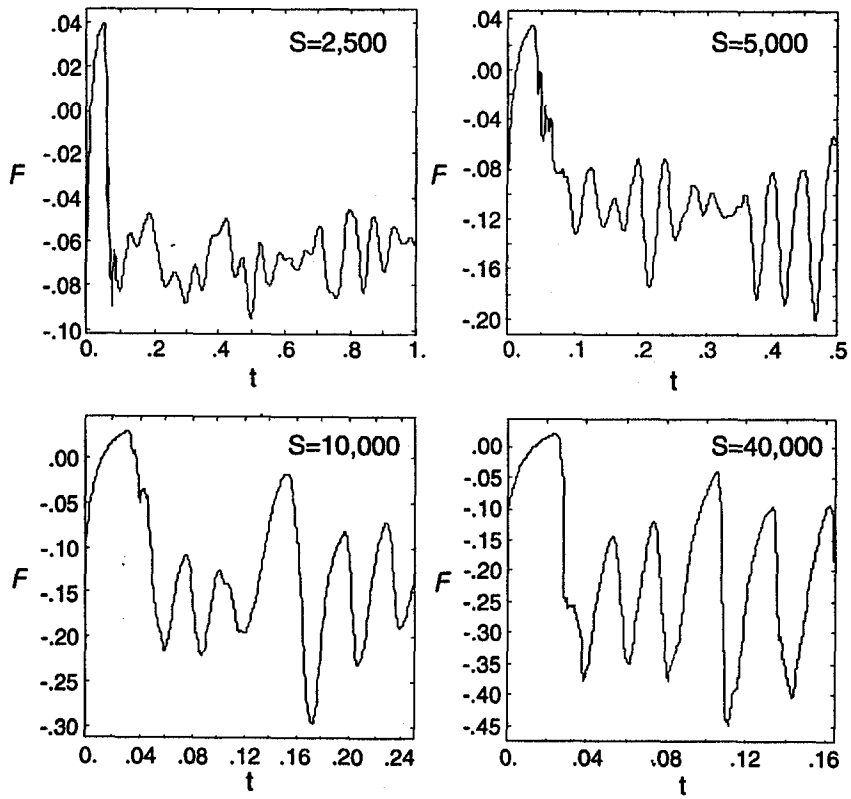

Figure 3.22 Comparison of the reversal parameter behavior for the Lundquist numbers indicated.

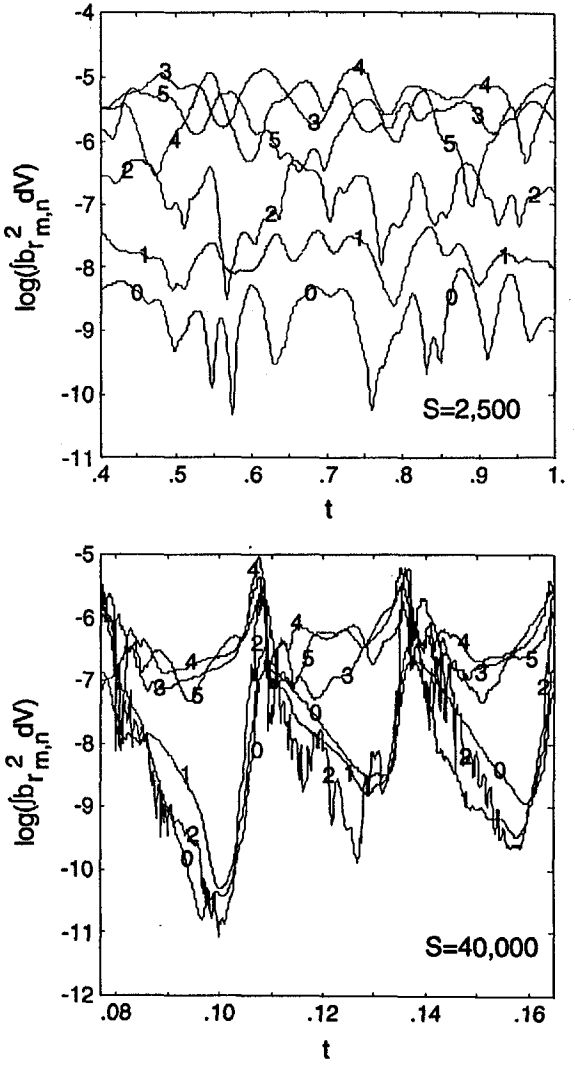

label	m	n
0	0	1
1	0	2
2	1	-4
3	1	-5
4	1	-6
5	1	-7

Figure 3.23 Comparison of the modal energy histories (radial contribution) for the lowest- and highest-S cases. [Reduced by a factor of 2^{10}.]

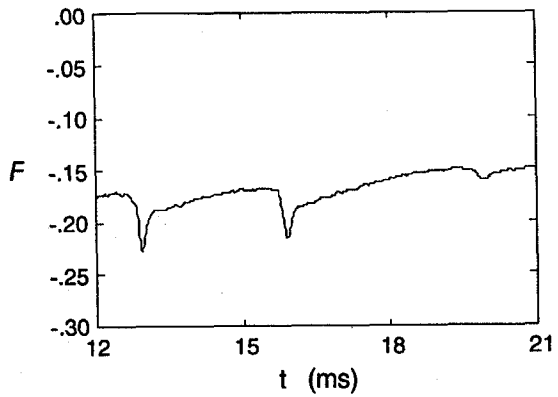

Figure 3.24 Time history of experimental reversal parameter near peak toroidal current in a $\Theta \cong 1.64$ MST discharge (shot #50, October 20, 1995). [Data courtesy of John Sarff.]

Despite the complications existing in the experiment, the temporal behavior of the fluctuations compare quite well. In MST, the poloidal component of magnetic fluctuations is measured with a set of 32 coils, and six of the toroidal modes are plotted in Fig. 3.25. With R/a=3, the (1,-5) mode is either not resonant or resonant near the axis, like the (1,-4) mode in R/a=2.5 simulations. Experimental signals for |n|<5 result from m=0 modes (Sarff, 1995). In comparison with the $S=4\times10^4$ plot in Fig. 3.23, both experiment and simulation show that the resonant m=1 modes rise prior to the drop in *F*. The explosive generation of m=0 modes and the 'axis mode' at the time of the crash is also consistent. All fluctuations are suppressed afterwards. The prolonged decay of m=0 modes—if it exists—cannot be observed on the linear experimental scale (the signals would probably be below the noise level, anyway).

Over a 'sawtooth' cycle in the $S=4\times10^4$ simulation, the current profile evolves in a manner that reflects the modal activity. Fig. 3.26 shows the evolution of the parallel current profile for one cycle, beginning and ending at sharp drops in *F*. The parallel current is enhanced inside the reversal surface when the m=1 energy peaks and *F* is dropping. Shortly thereafter, the increased current gradient near the reversal surface and nonlinear power from m=1 modes drive the m=0 modes to a large level. They induce current outside the reversal surface, and suppress it

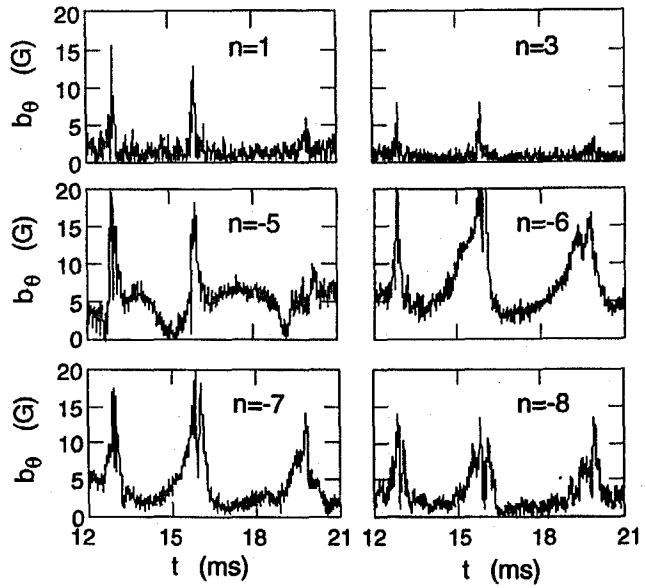

Figure 3.25 Fourier decomposition of experimental magnetic fluctuation signals (θ-component) from the same discharge and time period displayed in Fig. 3.24. All are measured near the wall, and those with |n|<5 are dominated by m=0 modes, while those with |n|≥5 are dominated by m=1. [Data courtesy of John Sarff.]

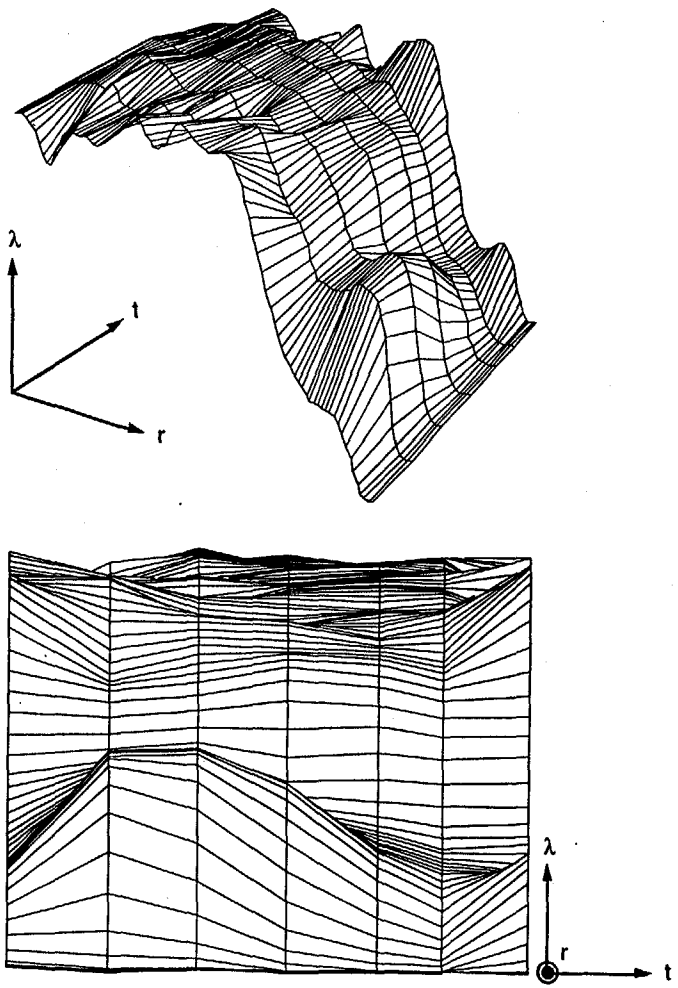

Figure 3.26 Two perspectives of the parallel current as a function of radius and time for the $S=4\times10^4$ simulation. The time represented is $0.136\le t\le0.165$, which starts and ends at sharp drops in *F*.

within. Meanwhile, diffusion smoothes the profile, and the current density on axis begins peaking. This increases the m=1 growth rates (see Fig. 3.23) until the next crash occurs. The pinch parameter (Θ) falls when the m=0 modes enhance parallel current along reversed magnetic field, outside the reversal surface. The applied $\langle E_z \rangle$ responds sharply according to Eq. 3.9. This is not realistic, but it occurs after *F* has dropped, so it is not responsible for triggering the crash.

The events that lead to the crash are consistent with Ho's description of the quasi-periodic oscillations in an $S=6\times10^3$ simulation (Ho, 1991). His three phases of dynamo: 1) interior m=1 modes gain energy, 2) nonlinear transfer of energy to m=1 modes near the reversal surface, and 3) mean poloidal current drive, produce the enhanced current inside the reversal surface at the time of the crash. However, there is an added phase of m=0 dynamo activity following the crash, which helps organize the temporal behavior. The m=1 modes are reduced following the initial redistribution of current inside the reversal surface. Similarly, the m=0 modes are reduced after they create the pedestal of parallel current outside the reversal surface. When the m=0 modes are small, the second dynamo phase is impeded. The third phase must then wait until the m=1 modes are large enough to nonlinearly drive the m=0 modes back to a significant level.

The fluctuation level scaling of $S^{-.18}$ from this scan is comparable to the result presented by Cappello and Biskamp of $S^{-.22}$ for $3\times10^3\le S\le1\times10^5$ (Cappello, 1993). They also observe increasing regularity in the temporal behavior of the reversal parameter (Cappello, 1994), though to a lesser degree than the DEBS results. The agreement enhances the credibility of both studies, since different codes with different numerical techniques have been used. Cappello and Biskamp use a spectral code where nonlinear products are created in Fourier space, so that modal resolution is free from FFT requirements. They eliminate many of the

smaller modes that must be computed with the pseudo-spectral algorithm but keep some modes with m as large as four. Another numerical difference is the hyper-dissipation, which is only employed in DEBS.

Although the fluctuation level scaling is similar, other results differ. Cappello and Biskamp do not observe an increase in the m=0 energy with S, and their reversal parameter decreases with S. These issues and the difference in regularity of the *F* oscillations are probably related. The discrepancies may result from the different aspect ratios (4 for Cappello and Biskamp vs. 2.5 here), but they may also result from the modal resolution, which is limited in different ways in the two studies. The pinch parameters are close (1.7 vs. 1.657), so this is not an issue.

References

J. A. Beckstead, "Sawteeth in the MST Reversed-field Pinch," Ph.D. thesis, University of Wisconsin-Madison, 1990.

S. I. Braginskii, "Transport Processes in a Plasma," Reviews of Plasma Physics **1**, 205 (Consultants Bureau, New York, 1965).

S. Cappello and D. Biskamp, "MHD studies of Stationary Turbulent Dynamics in a Reversed-field Pinch," in *Proceedings of the 20th European Physical Society Conference on Controlled Fusion and Plasma Physics,* Lisbon, II-487 (1993).

S. Cappello and D. Biskamp, "MHD studies of Stationary Turbulent Dynamics in a Reversed-field Pinch," in *Proceedings of the 1994 International Conference on Plasma Physics,* Foz do Iguacu, 149 (1994).

B. Coppi, J. M. Greene, and J. L. Johnson, "Resistive Instabilities in a Diffuse Linear Pinch," Nucl. Fusion **6**, 101 (1966).

G. Fiksel, S. C. Prager, W. Shen, and M. Stoneking, "Measurement of Magnetic Fluctuation Induced Energy Transport," Phys. Rev. Lett. **72**, 1028 (1994).

Y. L. Ho and G. G. Craddock, "Nonlinear Dynamics of Field Maintenance and Quasiperiodic Relaxation in Reversed-field Pinches," Phys. Fluids B **3**, 721 (1991).

Y. L. Ho, D. D. Schnack, S. Mazur, H.-E. Satherblom, J. Scheffel, and J. R. Drake, "Effect of Aspect Ratio on Magnetic Field Fluctuations in the Reversed-field Pinch," Phys. Plasmas **2**, 3407 (1995).

J. A. Holmes, B. A. Carreras, P. H. Diamond, and V. E. Lynch, "Nonlinear Dynamics of Tearing Modes in the Reversed Field Pinch," Phys. Fluids **31**, 1166 (1988).

J. C. Ingraham, R. F. Ellis, J. N. Downing, C. P. Munson, P. G. Weber, and G. A. Wurden, "Energetic Electron Measurements in the Edge of a Reversed-field Pinch," Phys. Fluids B **2**, 143 (1990).

A. R. Jacobson and R. W. Moses, "Nonlocal DC Electrical Conductivity of a Lorentz Plasma in a Stochastic Magnetic Field," Phys. Rev. A **29**, 3335 (1984).

J. A. Krommes, C. Oberman, R. G. Kleva, "Plasma Transport in Stochastic Magnetic Fields. Part 3. Kinetic of Test Particle Diffusion," J. Plasma Physics **30**, 11 (1983).

K. Kusano and T. Sato, "Non-linear Coupling Effects on the Relaxation Process in the Reversed Field Pinch," Nucl. Fusion **27**, 821 (1987).

K. Kusano and T. Sato, "Simulation Study of the Self-sustainment Mechanism in the Reversed-field Pinch Configuration," Nucl. Fusion **30**, 2075 (1990).

J. Li and D. Liu, "Tearing Mode in RFP Configurations," Alfven Laboratory Report ISSN 1102-2051, Stockholm, Sweden (1995).

R. A. Nebel, E. J. Caramana, and D. D. Schnack, "The Role of m=0 Modal Components in the Reversed-field-pinch Dynamo Effect in the Single Fluid Magnetohydrodynamics Model," Phys. Fluids B **1**, 1671 (1989).

A. B. Rechester and M. N. Rosenbluth, "Electron Heat Transport in a Tokamak with Destroyed Magnetic Surfaces," Phys. Rev. Lett. **40**, 38 (1978).

A. B. Rechester and T. H Stix, "Magnetic Braiding Due to Weak Asymmetry," Phys. Rev. Lett. **36**, 587 (1976).

J. S. Sarff, private communication (1995).

G. Schmidt, *Physics of High Temperature Plasmas*, 2 ed., (Academic Press, 1979).

D. D. Schnack, E. J. Caramana, and R. A. Nebel, "Three-dimensional Magnetohydrodynamic Studies of the Reversed-field Pinch," Phys. Fluids **28**, 321 (1985).

K. F. Schoenberg and R. W. Moses, "Magnetic Turbulent Electron Transport in the Reversed-field Pinch," Phys. Fluids B **3**, (1991).

M. R. Stoneking, "Fast Electron Generation and Transport in a Turbulent, Magnetized Plasma," Ph.D. thesis, University of Wisconsin-Madison, 1994.

M. R. Stoneking, S. A. Hokin, S. C. Prager, G. Fiksel, H. Ji, and D. J. Den Hartog, "Particle Transport Due to Magnetic Fluctuations," Phys. Rev. Lett. **73**, 549 (1994b).

J. B. Taylor, "Relaxation of Toroidal Plasma and Generation of Reverse Magnetic Fields," Phys. Rev. Lett. **33**, 1139 (1974).

P. W. Terry, G. Fiksel, H. Ji, A. F. Almagri, M. Cekic, D. J. Den Hartog, P. H. Diamond, S. C. Prager, J. S. Sarff, W. Shen, M. Stoneking, and A. S. Ware, "Ambipolar Constraints on Magnetic Fluctuation-induced Electron Thermal Transport," submitted to Phys. Rev. Lett.

H. Y. W. Tsui, "Magnetic Helicity Transport and the Reversed Field Pinch," Nucl. Fusion **28**, 1543 (1988).

4. HELICITY INJECTION FOR IMPROVING CONFINEMENT IN THE RFP

The fluctuation-level scaling discussed in Section 3.3 does not provide strong support for the RFP reactor concept. But, the nature of the MHD fluctuations is well-understood, and that knowledge can be used to improve confinement at any S. The drive of the largest modes results from an excessively-peaked parallel current distribution, and this can be modified by noninductive current drive. The modal contributions to the dynamo power density, shown in Fig. 3.4b, suggests how this may be done. The sign of the fluctuation-induced electric field is such that power is removed from the modes in the region $0.6 \le r \le 0.8$. If the mean current density in this region can be enhanced by auxiliary means, more power may be extracted from the fluctuations. The modes will then decay, resulting in better confinement. All terms involved are quasilinear, so linear stability resulting from current profile modification the same effect.

With fixed resistivity, enhancing the parallel current locally increases $\eta\langle \mathbf{J} \rangle \cdot \langle \mathbf{B} \rangle$, i.e., helicity dissipation (discussed in Chapter 1). Thus, there must be more helicity delivered to this region to sustain the improved state. Note that if the resistivity were locally reduced, or if some scheme generates collisionless charge carriers, there will be a reduction in helicity dissipation, which may be an effective substitute for helicity injection. The generation of fast particles is beyond the scope of MHD, but their impact on stability results from the current profile modification and not kinetic effects. Therefore, MHD analysis has an important role that is independent of the current drive mechanism.

The first two sections of this chapter are devoted to the stabilizing influence of current profile modification. The assumed current drive may best represent the

effects of RF waves, where the process does not otherwise influence MHD dynamics. [Wave propagation and energy deposition issues have been addressed elsewhere (see Shiina, 1992 and Uchimoto, 1994).] Linear stability calculations with varied auxiliary current drive parameters are discussed in Section 4.1. Related nonlinear simulations are presented in Section 4.2, and they confirm the implications of fluctuation suppression from the linear study. Quantitative information on the change in energy transport is also demonstrated with a finite-pressure simulation. In Section 4.3, I present DC helicity injection simulations that consider the complete injection/fluctuation-suppression problem. My results on this approach extend Ho's published work (Ho, 1991) and show that geometric effects are quite important. To complete the RFP fluctuation topic, Section 4.4 describes a simulation of an inductively-driven current pulse that yields transport reduction when applied in MST.

4.1 Linear Results

Since the source of MHD activity in RFPs is the instability of internally resonant modes, linear calculations are valuable for guiding the current profile modification efforts. I have used the RESTER code, described in Section 2.2, to determine the stability of many different configurations. The effect of plasma pressure on the modes and on the equilibrium fields is not considered, however.

The configurations used for this study have $\langle \mathbf{J} \rangle \times \langle \mathbf{B} \rangle = 0$ with a modified parallel Ohm's law, $\langle E_{\parallel} \rangle + \langle E_a \rangle = \eta \langle J_{\parallel} \rangle$, where $\langle E_a \rangle$ is an assumed auxiliary electric field. It may represent RF or other forms of current drive. With this modification, the parallel current profile is

$$\lambda(r) = \frac{\langle E_z\rangle\langle B_z(r)\rangle}{\eta(r)\langle B(r)\rangle^2} + \frac{\langle E_a(r)\rangle}{\eta(r)\langle B(r)\rangle} \,. \qquad (4.1)$$

The auxiliary field is given a Gaussian distribution in radius,

$$\langle E_a(r)\rangle = E_a \exp\left\{-\left(\frac{r-r_a}{\sigma_a}\right)^2\right\},$$

to parameterize the shape in terms of centering (r_a) and width (σ_a). The first term on the right side of Eq. 4.1 is the current driven by the axial electric field and has the same form as the paramagnetic equilibrium. Note that the auxiliary current changes the magnetic shear, so the current produced by the axial electric field is also affected. [Hereafter, $\langle\ \rangle$ is dropped for $\langle E_a\rangle$ and $\langle E_z\rangle$, but they are still mean fields.]

As an example of the linear effects of current profile modification, an auxiliary drive of E_a=1.5, r_a=0.6, and σ_a=0.15 is applied to the parameters used for Fig. 2.9: E_z=3.95, $\langle B_z(r=0)\rangle = 1$, and constant η. The resulting parallel current profile is essentially flat for r<0.5, and ψ_0, the solution without slope discontinuity, for the (1,-7) mode has less negative curvature to the right of its resonance surface (see Fig. 4.1). This brings ψ_0(r=1) above zero, which stabilizes the mode. From Eqs. 2.18 and 2.19, the additional current modifies the curvature of the solution through the terms,

$$-\lambda^2\psi + \frac{d\lambda}{dr}\frac{(m\langle B_z\rangle - kr\langle B_\theta\rangle)}{m\langle B_\theta\rangle + kr\langle B_z\rangle}\psi \,.$$

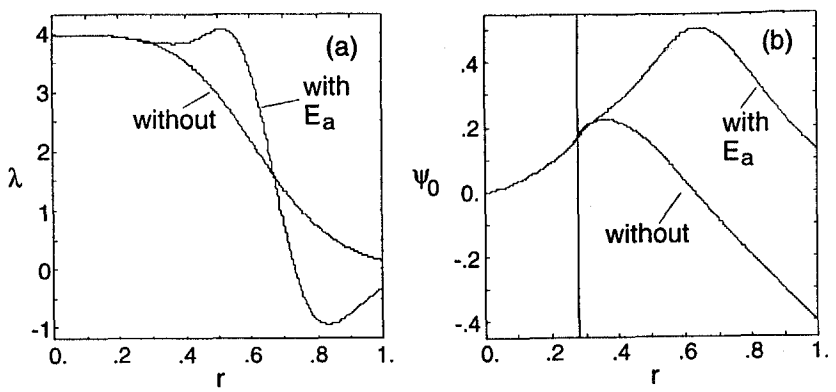

Figure 4.1 Comparisons of (a) parallel current profiles and (b) ψ_0 solutions for the (1,-7) mode with and without auxiliary current applied at r=0.6. The resonance surface does not move in this case, and its location is indicated by the vertical line in (b).

For the internal modes, the numerator of the current-gradient term is positive, while the denominator is positive on the left side of the resonance surface and negative on the right. Therefore, $d\lambda/dr < 0$ to the right of the resonance surface tends to bend ψ_0 to smaller values, which is destabilizing. The profile modification moves the λ gradient to a larger radius, where the denominator has a larger magnitude. The gradient still bends ψ_0 towards zero at r=0.7, but it does not lead to instability.

The enhanced current gradient outside r_a has an adverse effect on modes resonant in the exterior. The m=0 modes are stable without the profile modification, but m=0, 1≤n≤35 are resistively unstable with it. In addition, m=1 -20≤n≤-11 and 23≤n≤46 are also unstable. From this information alone, we cannot tell how much

transport will result from exterior modes, but some care is obviously necessary when applying the additional current.

A related study by Antoni, has proven that some parallel current profiles of the form $\lambda = \lambda_0\left(1-r^{\alpha}\right)$ are stable for all modes (Antoni, 1986). The auxiliary drive needed to sustain such configurations is found by subtracting $E_z\langle B_z\rangle/\langle B\rangle$ from $\eta\langle J_{\parallel}\rangle$. For these 'alpha model' profiles, the E_a distribution is broad and large near the wall. For example, with λ_0=3.95, the configuration is linearly stable for α=3. With E_z=3.95 to sustain the parallel current on axis, the necessary distribution is as shown in Fig. 4.2. The simple E_a distributions that are analyzed here are meant to guide proposed RF experiments on MST. I do not search for complete stability but instead try to determine what parameters are best for improving confinement with a limited current-drive capability.

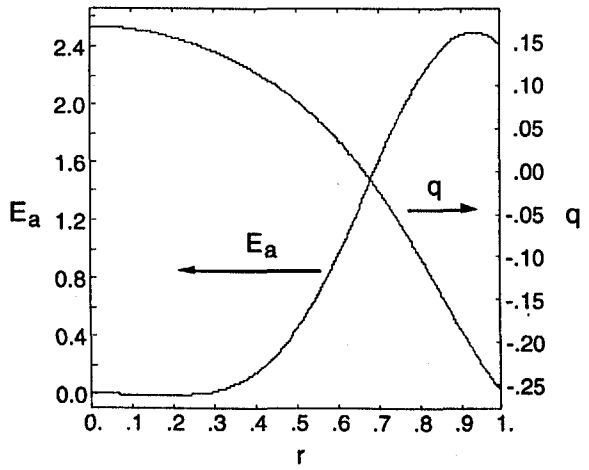

Figure 4.2 Auxiliary drive necessary to sustain the stable parallel current distribution, $\lambda = 3.95(1-r^3)$. The safety factor is also plotted to show the region of reversed field (q<0).

A parameter study completed with the RESTER code determines the stability of internally resonant modes while varying E_a, E_z, r_a, σ_a, and the resistivity profile. In linear calculations, axial mode numbers only appear through the wavenumber, k, but I have chosen to use integer n numbers with R=3 for consistency with MST. The group of modes under consideration is m=1, -9≤n≤-3, which includes the largest contributors to the fluctuation level. The resistivity profile has the form, $\eta(r)=1+31r^{\omega}$, and ω is set to 15 when r_a and σ_a are varied. For each (r_a, σ_a, ω) set, a 16×16 matrix of equilibria span the parameter space of $0\le E_a\le 6$ and $2\le E_z\le 5$. For each of these cases, the equilibrium solver—which marches from the axis to the wall—finds the value of $\langle B_z(r=0)\rangle$ that produces an axial flux of 0.66. Three sample equilibria are plotted in Fig. 4.3 to illustrate general features of the profiles. The first two are the low and high E_z limits with E_a=0, and the third has E_z=3.5 with E_a=1.5, r_a=0.7, and σ_a=0.15. The last of these is stable for all modes in the limited group.

Contour plots of Δ' show that the large |n| modes are the most sensitive to the parameters of the auxiliary current drive. The m=1, -8≤n≤-5 modes are plotted separately for (r_a=0.7, σ_a=0.15, ω=15) in Fig. 4.4, and the (1,-8) mode has the smallest region of stability ($\Delta' < 0$). The -8≤n≤-6 modes have similarly shaped bands of stability that are oriented on a diagonal. In general, moving to the left or above the band indicates that the auxiliary drive is insufficient or that the current profile is excessively peaked. In contrast, moving to the right or below the band indicates an excessive auxiliary drive or that the resonance surface is at a radius which is too large for the mode to benefit from the added current. The stable region for large |n| is displaced upward relative to small |n|, because a larger E_z is necessary to bring the resonance surface inside r_a. Within the region that is stable for all modes in the group, configurations at small values of E_z and E_a are

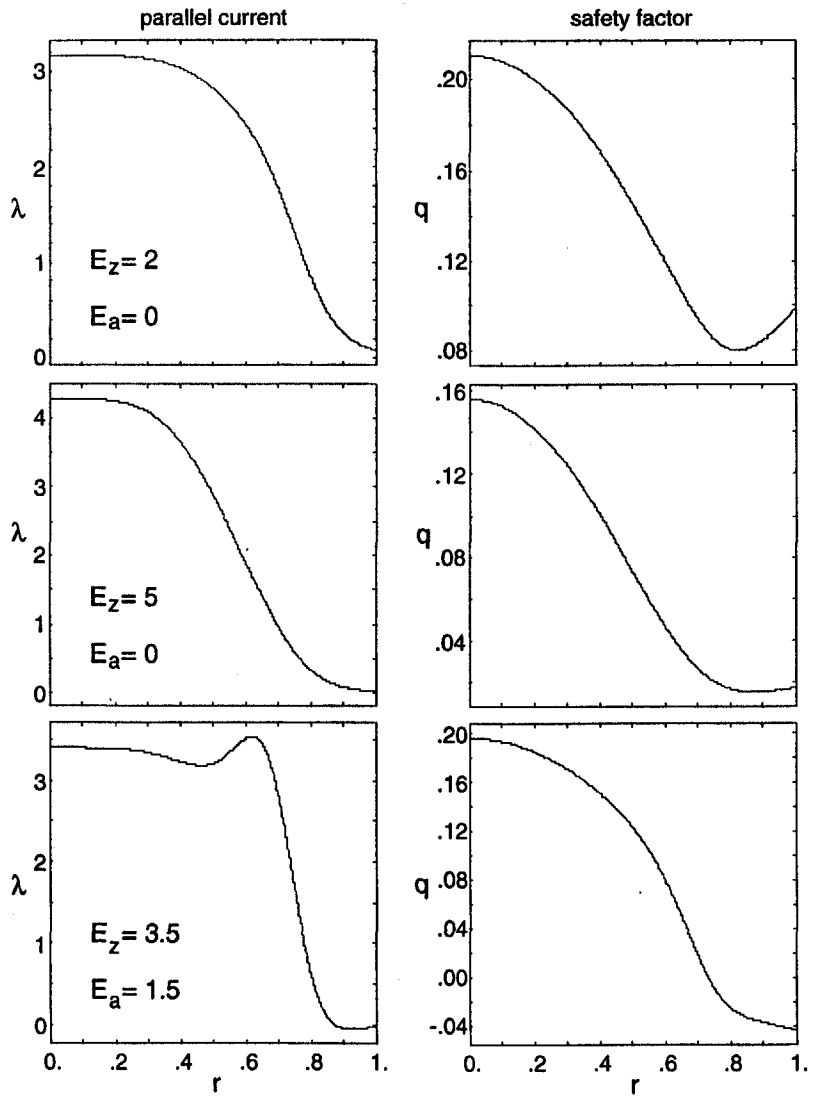

Figure 4.3 Representative profiles of parallel current and safety factor for three equilibria with the parameters indicated. All have $\eta(r) = 1 + 31r^{15}$.

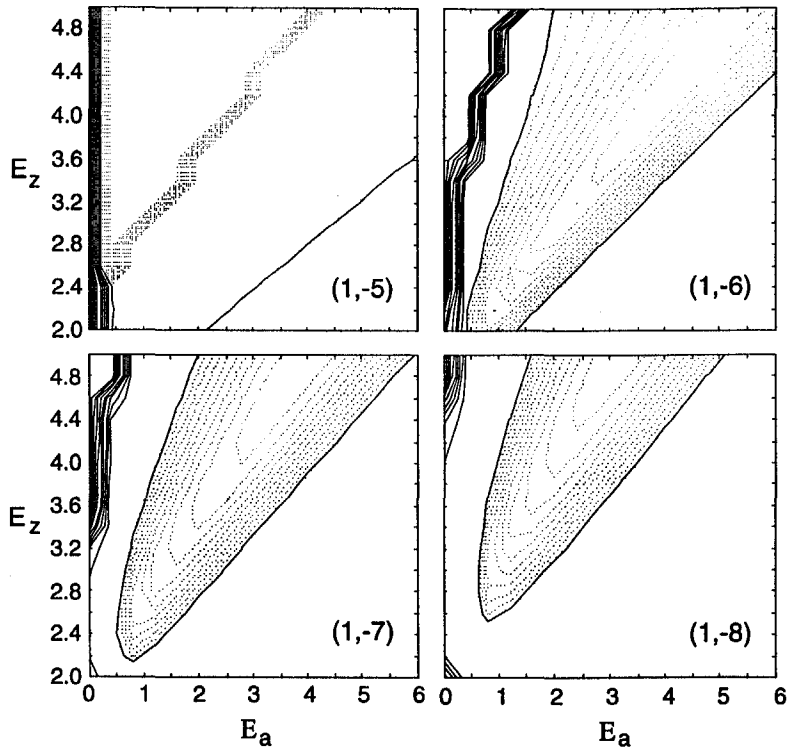

Figure 4.4 Contour plots of Δ' as a function of E_a and E_z for (r_a=0.7, σ_a=0.15, ω=15), with individual modes plotted separately. The solid lines indicate positive contour levels, dotted lines are negative contour levels, and the last solid line borders the stable region. Ideally unstable regions are plotted with $\Delta' = 1000$, which accumulates solid lines at the ideal/resistive instability border. The upper left corners of the -8≤n≤-6 plots are ideally unstable regions. The n=-5 mode is ideally stable and not resonant in the large triangle bordered by the accumulation of dotted contours.

preferable to those at large values, because the bump in the λ profile at r_a is smaller and therefore less destabilizing for exterior modes. In addition, small values of E_a imply small auxiliary power input; thus, the lower tip of the diagonal region is the most desirable condition. However, the location of the tip depends on the range of n considered, so it is important to evaluate only the modes that are most responsible for the transport.

To investigate the influence of the E_a profile shape, stability calculations have been performed for $0.6 \le r_a \le 0.8$ and $0.1 \le \sigma_a \le 0.2$. Figs. 4.5-4.7 show the maximum Δ' (least stable) of all modes in the m=1, $-9 \le n \le -3$ group, and different values of σ_a are plotted in separate figures. For each value of σ_a, the stable region moves to lower values of E_z as r_a is increased. Comparing the different values of σ_a for the same r_a shows that the stable region is larger as σ_a increases. Thus, a stable E_a-E_z combination is relatively easy to find if the auxiliary drive profile is broad. The tip of the stable region also moves to the left, so the auxiliary power does not necessarily increase as σ_a is increased.

The resistivity profile has been varied in a set of calculations with r_a=0.7 and σ_a=0.15, and the results for $7.5 \le \omega \le 20$ are shown in Fig. 4.8. The largest effect is that the stable region moves to smaller values of E_a as the resistivity profile is broadened. This is attributed to the change in resistivity at r_a that results when the profile shape is changed—inducing the same current density requires more electric field as the local resistivity is increased. The stable region also moves downward as ω is increased. Small values of ω implies a larger exterior resistivity, so a large E_z is necessary to move the group's resonance surfaces within r_a.

A final scan has R/a=1.25 with stability calculated for the m=1, $-4 \le n \le -1$ modes and (r_a=0.8, σ_a=0.2, ω=15), and the Δ' contours are shown in Fig. 4.9. It is very similar to one of the previous scans, but k=-3.2 (now n=-4) is included. This mode

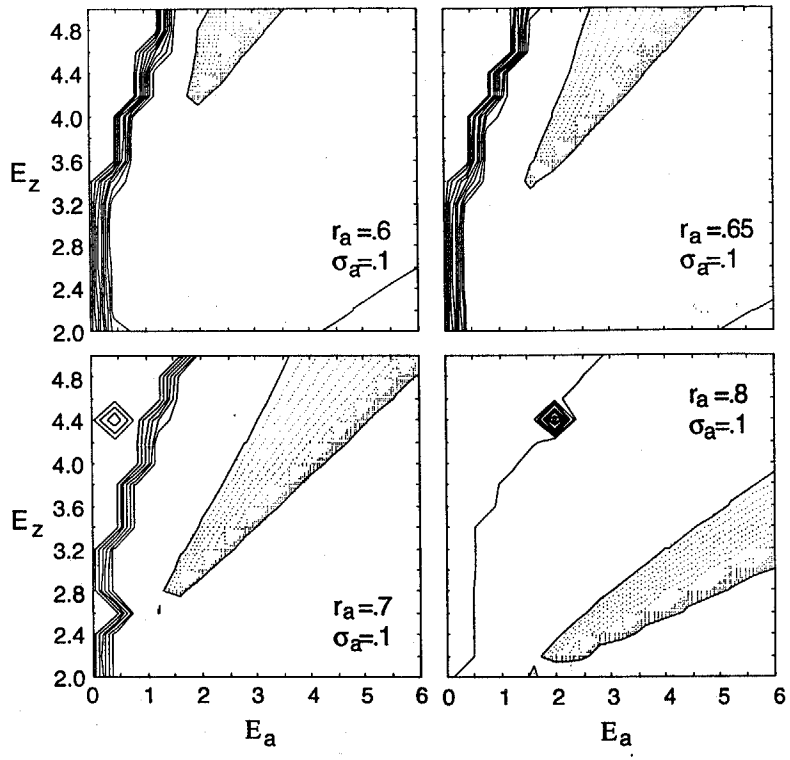

Figure 4.5 Contours of maximum Δ' (over m=1, $-9 \le n \le -3$) for σ_a=0.1 and the different values of r_a as indicated. The resistivity profile is $\eta(r) = 1 + 31r^{15}$.

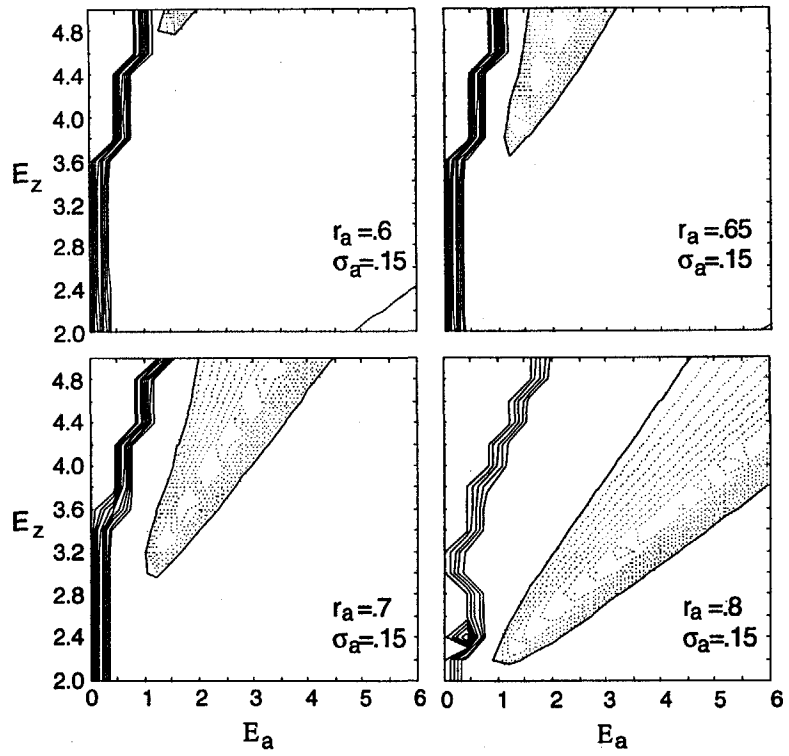

Figure 4.6 Contours of maximum Δ' (over m=1, $-9 \le n \le -3$) for σ_a=0.15 and the different values of r_a as indicated.

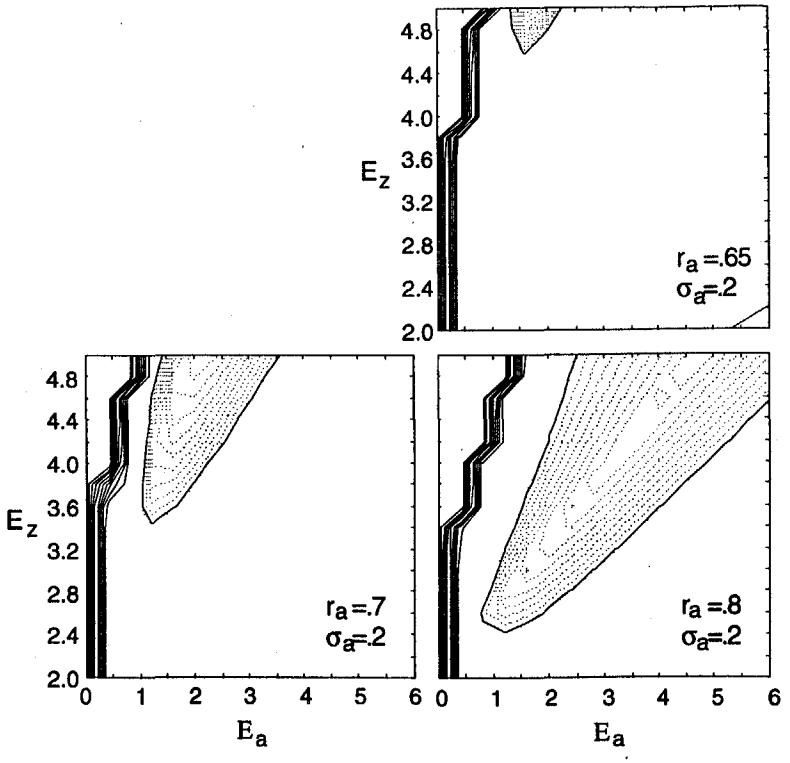

Figure 4.7 Contours of maximum Δ' (over m=1, $-9 \le n \le -3$) for σ_a=0.2 and the different values of r_a as indicated. For r_a=0.6, the entire region is unstable.

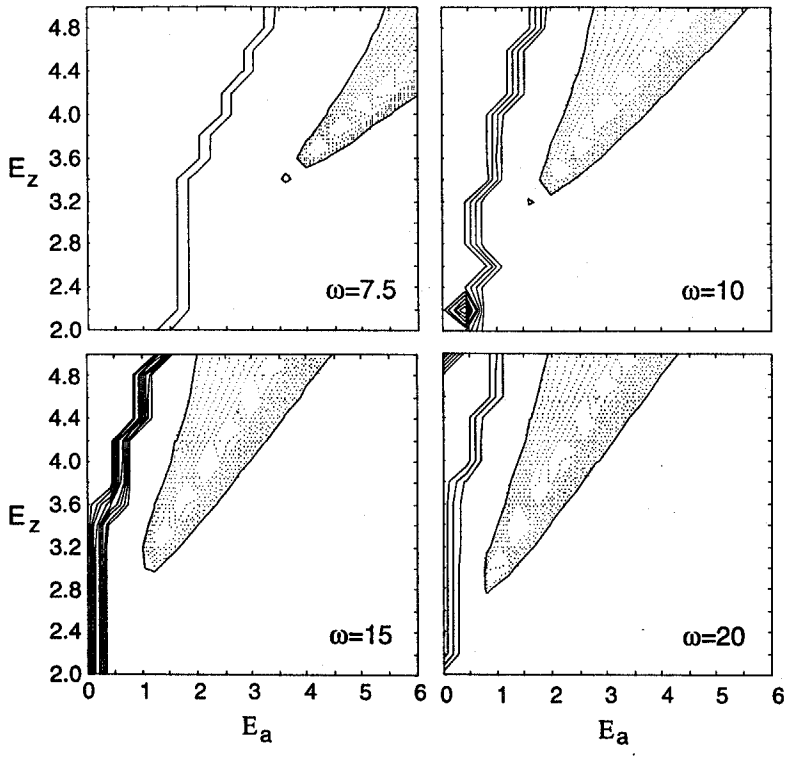

Figure 4.8 Contours of maximum Δ' (over m=1, $-9 \le n \le -3$) for (r_a=0.7, σ_a=0.15), with the resistivity profile parameters indicated: $\eta(r) = 1 + 31r^{\omega}$.

is important in a finite pressure simulation with R/a=1.25 that is discussed in Section 4.2. The heavy line indicates Θ=1.8, which the simulation maintains as auxiliary drive is applied.

The most important lesson from these parameter studies is that stabilization requires a balance between E_a and E_z to put the modes' resonance surfaces inside of, but not too far from the location of the auxiliary drive. For optimization with given r_a and σ_a, the tip of the stable region for the internal modes in E_a-E_z space is best, because the auxiliary drive and the λ bump are minimized. Large values of r_a help stabilize more of the radial domain, and large σ_a makes the stable E_a-E_z region broad.

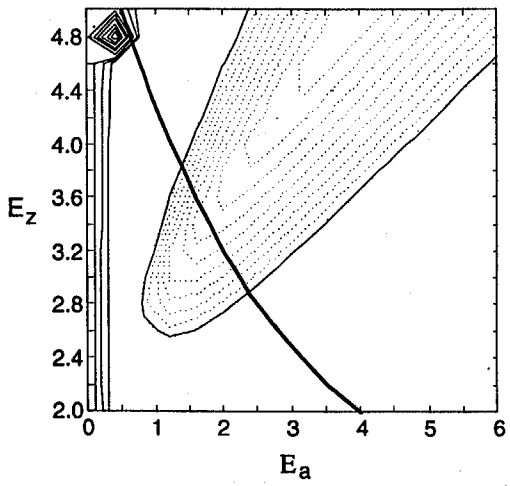

Figure 4.9 Contours of maximum Δ' (over m=1, $-4 \le n \le -1$) for (r_a=0.8, σ_a=0.2, ω=15), for the reduced aspect ratio R/a=1.25. The heavy line indicates equilibria with Θ=1.8.

4.2 Auxiliary Drive in Nonlinear Simulations

Nonlinear simulations including auxiliary current drive address several issues. First, pressureless simulations allow direct comparison with linear calculations to validate conclusions drawn from them. Second, the residual fluctuation level is important. Since I have not tried to stabilize all modes, the saturation level of those resonant outside the current drive may increase. In addition, nonlinear interactions can sustain the stabilized internal modes, so the center of the plasma may also retain some fluctuation level. Third, simulations with pressure quantitatively predict confinement improvement. They also show that the pressure-gradient drive of internally resonant modes becomes significant as the current-gradient drive is decreased and interior pressure builds.

In the nonlinear simulations, I apply an auxiliary parallel electric field through the m=0, n=0 Fourier component of Ohm's law with the same Gaussian distribution that is used in the linear calculations. Although the auxiliary drive is a generic form of helicity injection, the computations were motivated by the RF current drive concept. The velocity-space resonance effects of RF current drive (Fisch, 1978) cannot be modeled with MHD, but waves that impart momentum can be represented by an electron force, after averaging over a wave period. When separate electron and ion fluid equations are combined to form MHD equations, forces on the electrons are retained in both the single-fluid momentum equation and Ohm's law (in MKS units):

$$\rho\frac{\partial \mathbf{V}}{\partial t}+\rho\mathbf{V}\cdot\nabla\mathbf{V}=\mathbf{J}\times\mathbf{B}+F_a\frac{\langle\mathbf{B}\rangle}{\langle B\rangle} \tag{4.2}$$

$$\mathbf{E}-\frac{1}{ne}F_a\frac{\langle\mathbf{B}\rangle}{\langle B\rangle}=\mathbf{E}+\langle\mathbf{E}_a\rangle=-\mathbf{V}\times\mathbf{B}+\eta\mathbf{J} \tag{4.3}$$

where e is the elementary charge. Some simulations include the parallel force in Eq. 4.2, while others just have the auxiliary electric field in Eq. 4.3. When it is included, the magnitude of the driven flow is small, although the resulting power can be approximately 5% of the total system power. I have not observed any directly attributable effects, but nonlinear coupling between modes rotating at different rates may be inhibited. In the following subsections, I indicate which simulations include this force.

The simulations are started from RFP simulations without auxiliary drive. The magnitude, E_a, is increased slowly then held fixed at the desired level. For time-averaged information, temporal integrations are started after the transient phase resulting from the profile modification. The pressureless simulations discussed in Section 4.2.1 have $\eta(r)=\left(1+9r^{30}\right)^2$, and E_z is held constant while the auxiliary drive is applied. The finite pressure simulations in Section 4.2.2 have E_z adjusted to maintain constant Θ. Temperature-dependent resistivity is used in these cases, so E_z must be reduced while confinement improves to prevent excessive current density on axis. To avoid similar problems at r_a, the quotient $E_a/\eta(r_a)$ is specified instead of E_a.

4.2.1 Auxiliary Drive in Pressureless Simulations

Conclusions drawn from the linear study concerning the location and magnitude of the auxiliary drive are verified by nonlinear simulations. At $S=10^4$, internal modes may be reduced by an order of magnitude or more, though they are typically sustained to some degree. The reduction results from eliminating the large current-gradient drive associated with normal RFP profiles, but nonlinear interactions with the remaining unstable modes keep the targeted group from

disappearing completely. Here I shall discuss three representative cases. All have azimuthal modes $0 \le m \le 2$ resolved, and $R/a=3$.

The first simulation is an example of successful fluctuation suppression. The parameters are $\Phi=0.967$, $E_z=3.15$, $E_a=1.4$, $r_a=0.8$, and $\sigma_a=0.1$, and the electron force is included in the (0,0) momentum equation. At the end of the simulation, the auxiliary electric field supplies 14% of the total power, while the auxiliary, single-fluid force supplies 6%. Parallel current and safety factor profiles with and without the auxiliary drive are compared in Fig. 4.10 and show that the auxiliary drive generates reversal in this case. The profiles resulting from Eq. 4.1 with the same parameters are also displayed. This equation is derived from the parallel component Ohm's law without dynamo electric field, so the similarity between its prediction and the simulation result confirms a reduction in dynamo activity. The nonlinear simulation has a smaller peak at the location of the auxiliary drive, because it is reduced by locally resonant modes.

Fluctuation spectra are compared in Fig 4.11 and display the benefit of applying auxiliary drive. The largest internal modes are reduced by nearly two orders of magnitude. Modes with $n \le -11$, which are resonant at $r \ge 0.7$, are not reduced, but they are also not significantly enhanced. The m=0 modes are resonant at r=0.86, which is in the center of the large λ gradient outside r_a. The largest mode is smaller than the maximum without auxiliary drive, but the spectrum becomes very broad. This simulation would benefit from more axial resolution, but the relative change induced by the auxiliary drive is meaningful. The reduction of internal modes leads to the annealing of flux surfaces for $r \le 0.6$, as shown in Fig 4.12.

A RESTER calculation with the same parameters and resistivity profile (which produces the current profile in Fig. 4.10), predicts stability for the m=1, $-10 \le n \le -5$ modes. They are stabilized by the auxiliary drive, since all resonant m=1 modes

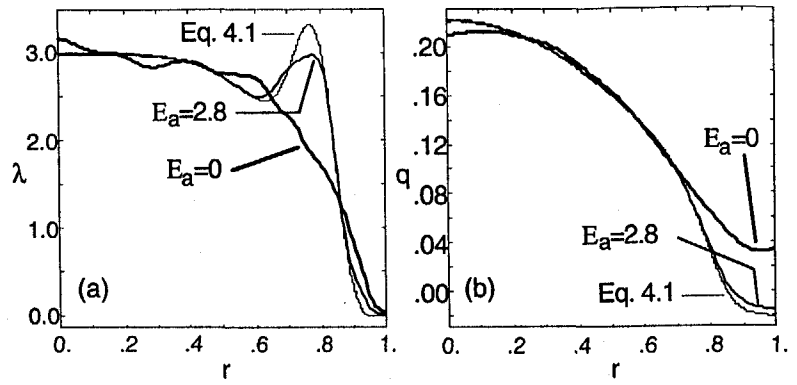

Figure 4.10 Profiles of (a) parallel current and (b) safety factor from the simulations with and without auxiliary drive and based on Eq. 4.1 with the same parameters.

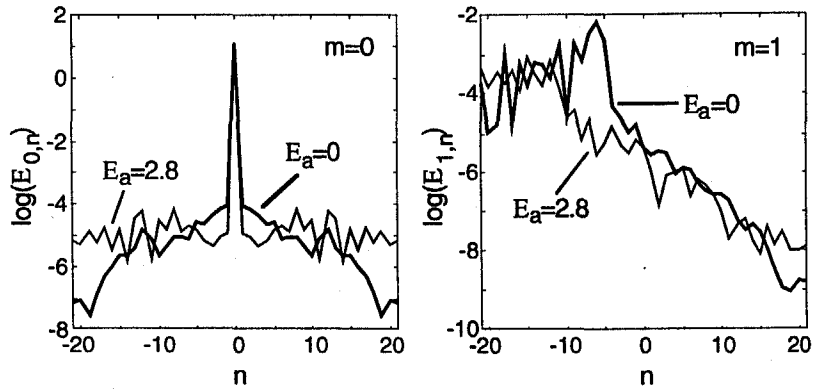

Figure 4.11 Magnetic energy spectra for the poloidal modes indicated on the plots, where $E_{m,n} \equiv \frac{1}{2}\left(\int b_{m,n}^2 dx + \text{c.c.}\right)$. The information is taken from the end of the simulations and is not averaged in time.

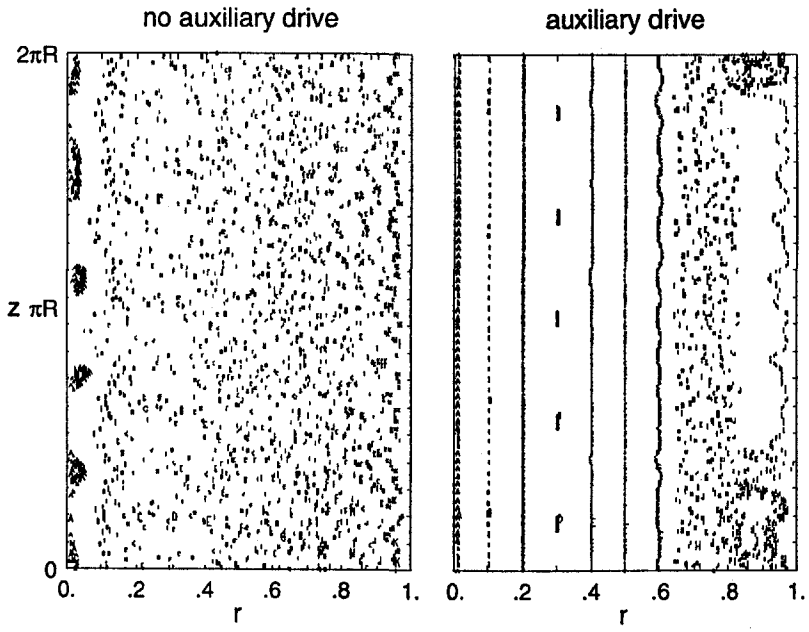

Figure 4.12 Comparison of magnetic field-line puncture plots in the r-z plane for the two cases with E_z=3.15, with and without the auxiliary drive.

with n≥-22 are unstable without it. However, modes in the ranges (m=0, 1≤n≤59) and (m=1, -38≤n≤-11 and 56≤n≤80) remain or are driven unstable. Comparing with the nonlinear simulation, the (1,-11) mode has the smallest |n| of those not reduced by the auxiliary drive (see Fig. 4.11), which is consistent with the linear prediction. Although some exterior modes are destabilized, they do not grow to a large level.

To investigate the auxiliary drive at a larger pinch parameter, two simulations have been run from the case discussed in Sections 2.1.1 and 3.1. Both have Φ=0.674, E_z=3.8, E_a=2.8, and σ_a=0.1 and resolve axial modes -42≤n≤42. The electron force is not included in the momentum equation in these cases. The two have different auxiliary drive locations; r_a is 0.65 for one and 0.8 for the other. It supplies 26% of the total input power in the first case and 23% in the second, and the final pinch parameters are 1.8 and 1.7, respectively (the previous case has Θ=1.4).

The resulting fluctuation spectra, shown in Fig. 4.13 with the E_a=0 results, are remarkably different. The auxiliary current suppresses m=1, n>-8 internal modes when r_a=0.65, but the (1,-6) mode, which is resonant nearest the axis, is not affected when r_a=0.8. Modes that are resonant further from the axis are reduced to a moderate extent in both cases. The m=0 spectra also differ. For r_a=0.65, the small |n| modes are no larger than the case without auxiliary drive, though the spectrum is broadened. For r_a=0.8, the small |n| modes are enhanced.

Linear predictions capture the essential features of the nonlinear results in these cases, also. An overview is provided by the Δ' contour plots in Fig. 4.5, though the resistivity profile is not the same as in the simulations. The stable region for the internal modes covers the (E_a, E_z) point, when r_a=0.65, but it moves to lower values of E_z when r_a=0.8. With the simulated resistivity profile and r_a=0.65, the following groups are linearly unstable: (m=0, 1≤n≤43), (m=1, -34≤n≤-9 and 20≤n≤53), and (m=2, 40≤n≤53). For r_a=0.8, (m=0, 1≤n≤30), (m=1, -7≤n≤-6 and 9≤n≤35), and (m=2, 18≤n≤41) are unstable. When m=1 modes resonant near the axis are linearly stable, there is a great reduction in the nonlinear saturation level. However, when these modes are not stable, modes resonant at larger radii may not be significantly reduced, due to nonlinear coupling from the core. The fluctuation

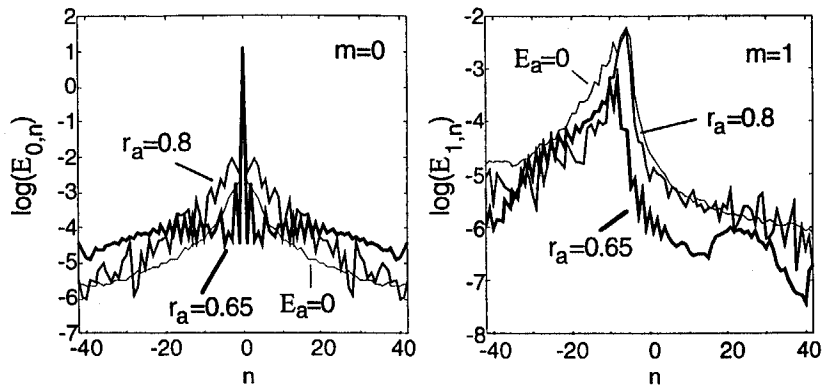

Figure 4.13 Magnetic energy spectra of simulations with auxiliary drive applied at different radii. The r_a=0.8 information is from the end of the simulation, the other two are time-averaged.

reduction in the small r_a case leads to closed flux surfaces for r≤0.35, but there are no closed flux surfaces for the large r_a case (see Fig 4.14).

Considering all three simulations, the low Θ case produces the best results with flux surfaces out to r=0.6. Therefore, a small E_z, large r_a combination is preferable to a large E_z, small r_a combination. Retaining some degree of reversal is important, because the nonlinear coupling provided by the m=0 modes helps saturate those that are unstable. But with auxiliary current drive, large axial electric fields are not necessary. With relatively small E_z, the interior has less than normal shear for an RFP, and this portion of the discharge has the properties of a stable paramagnetic equilibrium. The auxiliary drive substitutes for the dynamo to sustain reversal.

In summary, there is very good agreement between the linear predictions of stability and nonlinear results of fluctuation reduction for the internal modes. An

integral part of this is reducing the dynamo, so that simulated current profiles agree with those from Eq. 4.1. Also, the residual fluctuation level is not so great that it precludes flux surface formation. Most of the external modes are no larger with the auxiliary drive than they are without it. These modes are usually sustained by nonlinear coupling, which is reduced when the interior modes are suppressed. Finally, the nonlinear results also confirm the benefit of choosing large r_a and small E_z (small Θ); it produces a large region of closed flux surfaces across the minor radius.

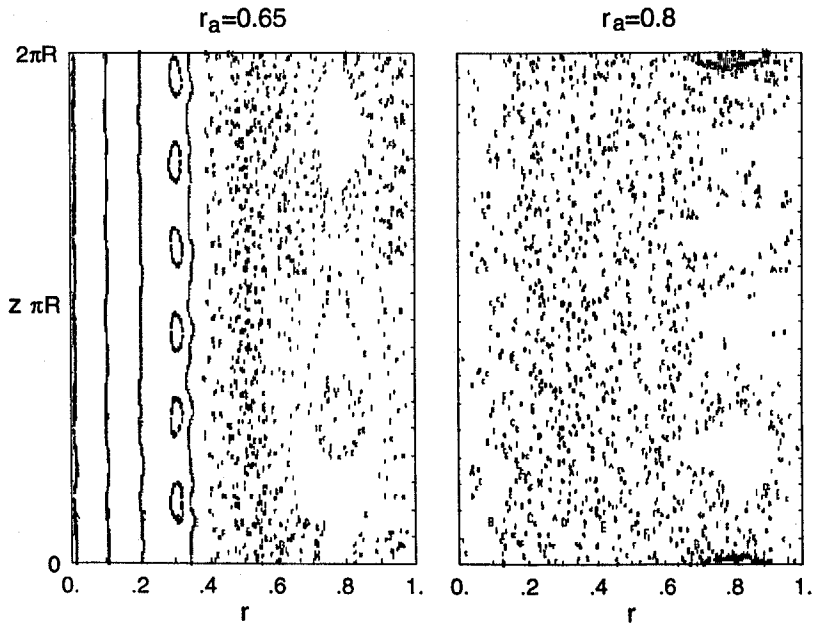

Figure 4.14 Comparison of magnetic field-line puncture plots in the r-z plane for simulations with E_z=3.8. The centering of the auxiliary drive is indicated.

4.2.2 Auxiliary Drive with Pressure

The simulations discussed in this section use the same plasma parameters as the one described in Section 3.2. Auxiliary drive is applied with r_a=0.8 and σ_a=0.2, to suppress fluctuations over a large portion of the radial domain without a lot of sensitivity to the final E_a and E_z. The pinch parameter is kept at 1.8, so the conditions should track the heavy line in Fig. 4.9 from the left side of the parameter space into the stabilized region. The resistivity profile is not fixed, however, and the location of this region may move. There is an initial transient phase as the current and pressure profiles evolve, but E_z and E_a are adjusted to prevent thermal runaway. Following this phase, the simulations again settle into a quasi-steady condition.

With $E_a/\eta(r_a)$=1.02, the time-averaged parallel current profile acquires the shape of a modified Bessel function model; it is virtually flat from the axis to r=0.8 (see Fig. 4.15). This reduces the dynamo power density by more than a factor of ten (compare Fig. 4.15c with Fig. 3.12c), and remaining activity for r≤0.5 is primarily due to the (1,-2) mode, which becomes resonant. The magnetic fluctuation spectra with and without auxiliary drive are compared in Fig. 4.16. The (m=1, -6≤n≤-3) modes are reduced by at least an order of magnitude, though the (1,-2) stays at the same level. The small aspect ratio inhibits nonlinear coupling, which prevents this mode from sustaining the others. All m=0 modes are suppressed, so the enhanced current gradient at r=0.9 does not lead to a large fluctuation level near the wall.

The effective thermal diffusivity over most of the plasma decreases as the fluctuation level is reduced. In the center of the radial domain, χ_e is reduced by two orders of magnitude, which is commensurate with the reduction of fluctuation energy for the locally resonant modes (compare Figs. 4.17 and 3.15). The spike at r=0.75 results from the (1,-8) mode, which is not reduced by the auxiliary drive.

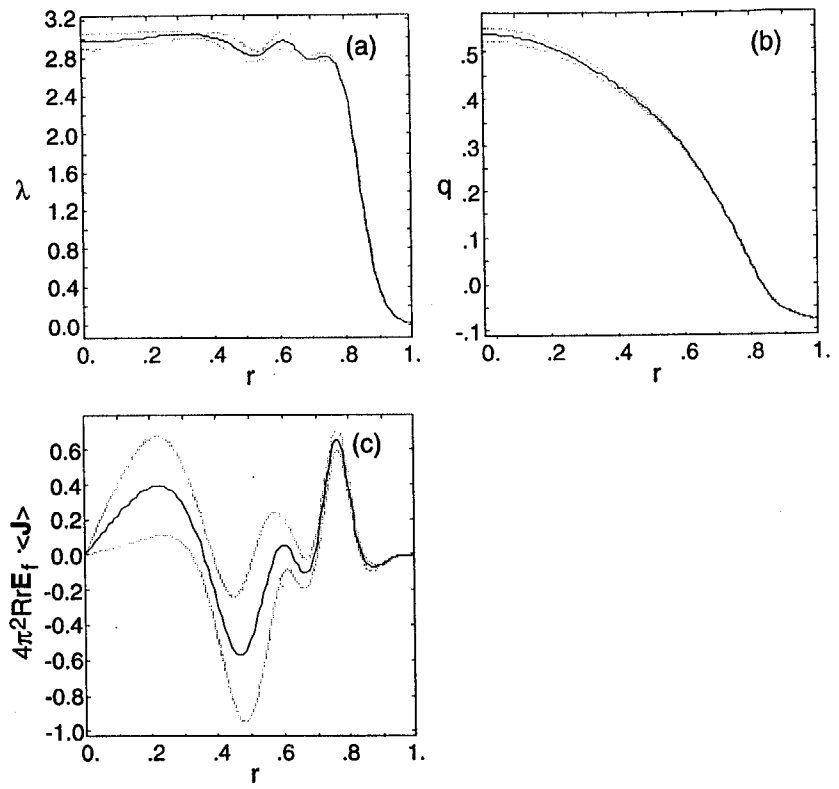

Figure 4.15 Radial profiles of (a) parallel current, (b) safety factor, and (c) dynamo power density for the finite-pressure simulation with auxiliary drive. The solid line is the time average over 0.6 τ_r, and the dotted lines are one standard deviation above and below.

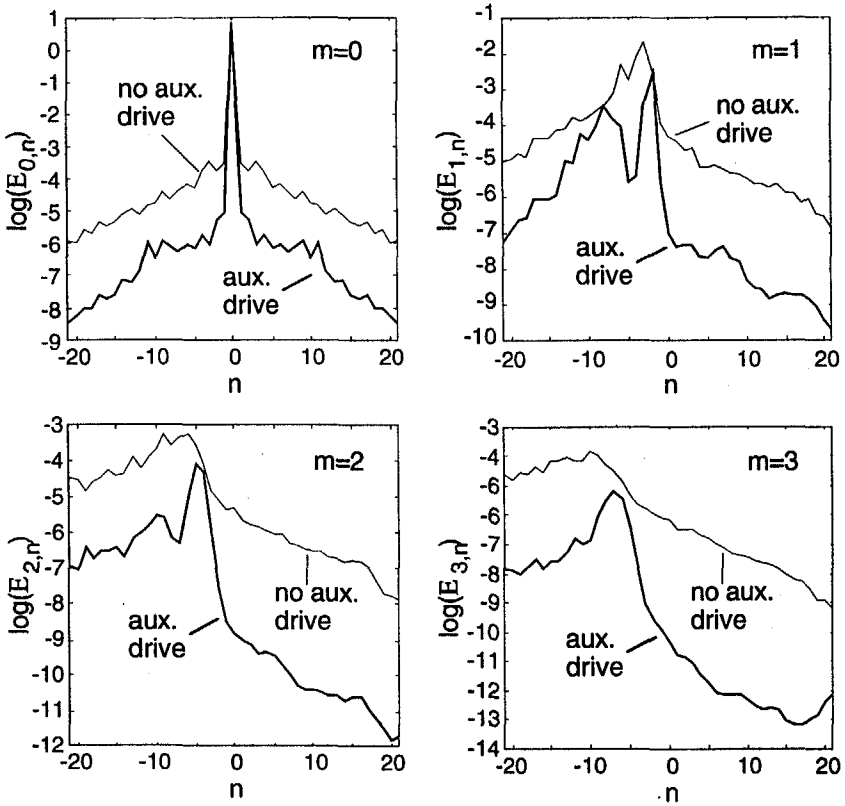

Figure 4.16 Comparison of time-averaged magnetic fluctuation spectra for the finite-pressure simulations with and without auxiliary drive.

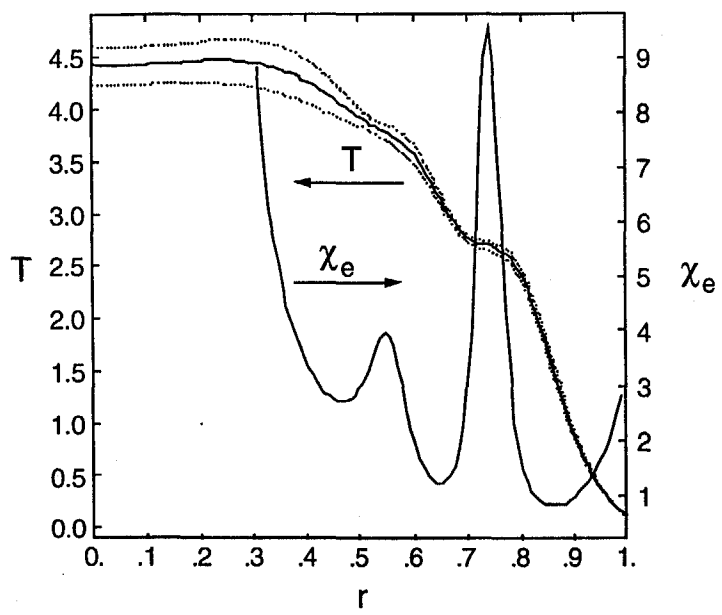

Figure 4.17 Radial profiles of mean temperature and effective thermal diffusivity for the quasi-steady condition with auxiliary drive. The temperature is averaged over 0.6 τ_r, and the diffusivity is based on the average temperature gradient and total heat flux. The diffusivity is not computed near the axis, where the gradient is nearly zero.

Near the axis, confinement is not improved, but the central temperature increases from 2.5 to 4.4. The decomposition of internal energy transport is shown in Fig. 4.18. Conduction parallel to magnetic fluctuations still dominates interior transport, and the fluctuation-induced convection remains relatively small.

In the final quasi-steady state, E_z is only 25% of its initial value, and the auxiliary drive supplies 40% of the total power . [The electron force is included in the momentum equation, but the resulting power is negligible.] Thus, while the total power is reduced by more than a factor of two, power flowing across the r=0.5 surface is reduced by more than a factor of three (see Figs. 4.18 and 3.14). This power flow change results in the $\tau_E(r)$ profile shown in Fig. 4.19, which is nearly flat. The auxiliary drive serves to spread input power more evenly than inductive drive alone. Applying more auxiliary drive is harmful. A simulation with $E_a/\eta(r_a)$ increased by 10% has an energy confinement time that is 20% smaller. The resulting parallel current profile in Fig. 4.20a has a destabilizing positive gradient at r=0.6. Enhanced dynamo activity and associated fluctuations are centered where the previous simulation has a large temperature gradient.

Without auxiliary drive, the influence of plasma pressure on the internally resonant modes is small relative to the current-gradient drive. After its application, dynamo power is reduced by the current profile flattening, and β_p increases from 22% to 30%. The powers that drive the fluctuations are plotted in Fig 4.21 for comparison with Fig. 3.17. Clearly, the pressure drive is much more significant here. The two powers are equally important for the m=1 and m=2 modes, and pressure term is larger than the current-gradient term for the m=0 modes.

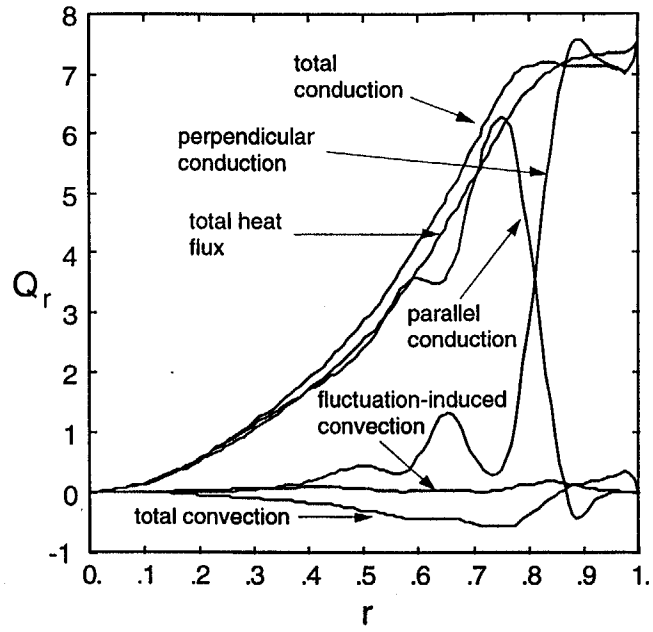

Figure 4.18 Decomposition of internal energy transport at the end of the finite-pressure simulation with auxiliary drive.

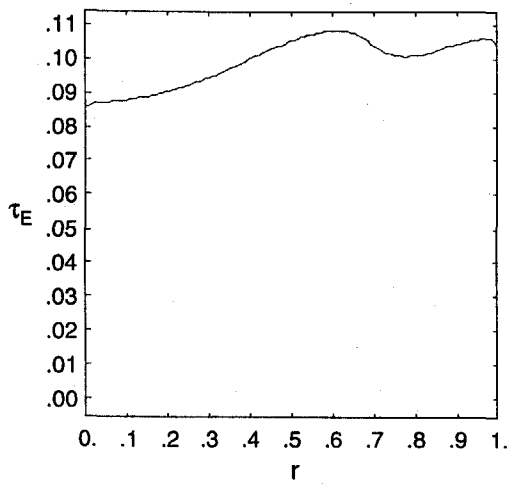

Figure 4.19 Energy transit time as a function of radius for the simulation with auxiliary drive.

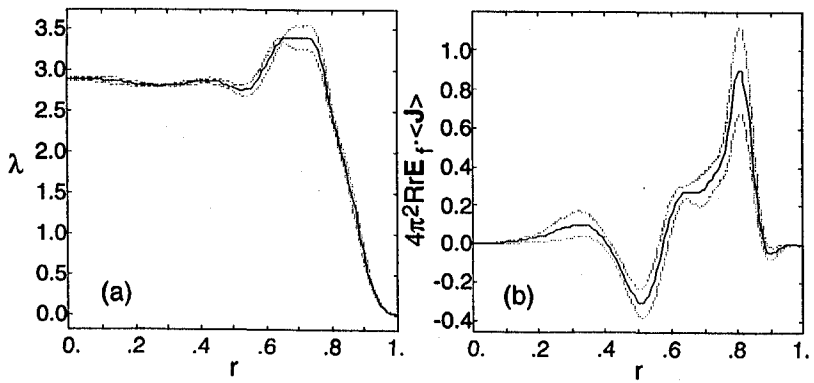

Figure 4.20 Radial profiles of (a) parallel current and (b) dynamo power density from the simulation with 10% more auxiliary drive.

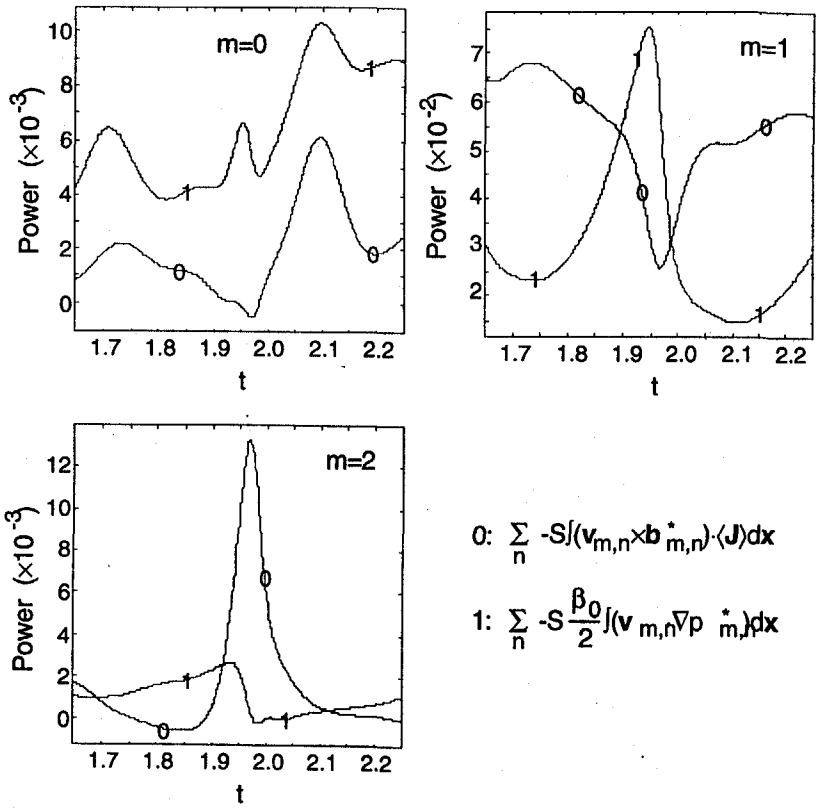

0: $\sum_n -S\int(\mathbf{v}_{m,n}\times\mathbf{b}^*_{m,n})\cdot\langle\mathbf{J}\rangle d\mathbf{x}$

1: $\sum_n -S\frac{\beta_0}{2}\int(\mathbf{v}_{m,n}\nabla p^*_{m,n})d\mathbf{x}$

Figure 4.21 Comparison of the powers flowing into poloidal mode groups for the simulation with auxiliary drive.

The impact of the pressure-gradient drive on confinement is assessed by continuing the simulation with $(S\beta_0/2)\nabla P$ removed from all but the (m=0, n=0) Fourier component of the momentum equation (Eq. 2.12). Only $S\nabla\cdot(\langle P\rangle\langle \mathbf{V}\rangle)$ and $S(\gamma-1)\langle P\rangle\nabla\cdot\langle \mathbf{V}\rangle$ of the hydrodynamic terms in the pressure evolution equation (Eq. 2.11) are retained. In this fashion, internal energy transport remains consistent with the MHD dynamics, and the force balance between the mean pressure gradient and the Lorentz force from the mean magnetic field is not disturbed. The modes reducing confinement initially decay, which results in β_p rising to 37% (see Fig. 4.22). The change in resistivity near the axis affects the current profile, and the (1,-2) mode increases. The average temperature profile and effective diffusivity for the period, $1.85\le t\le 2.25$, are shown in Fig. 4.23. Although the (1,-2) mode keeps the temperature profile flat at the plasma center, the effective diffusivity for $0.3\le r\le 0.6$ is reduced. The change is again commensurate with the modest change in energy for the locally resonant modes.

These simulations prove that auxiliary drive can sustain RFP configurations with confinement properties that are considerably improved over those powered by inductive drive alone. Although global tearing modes still dictate core confinement, χ_e is reduced by two orders of magnitude. This reduction is directly related to changes in magnetic fluctuation energy, consistent with analytic, stochastic-field diffusivities, which are proportional to $\langle b_r^2\rangle$. The energy confinement time for the device improves by a factor of three, and the energy transit time at r=0.5 is larger by a factor of seven (compare Figs. 4.19 and 3.16). Thus, the region that has the poorest confinement in conventional RFPs receives the most benefit. When the pressure terms are removed, there is another factor of three improvement at r=0.5, but the device confinement time is only slightly better (see Fig. 4.24). The difficulty

is that as interior confinement improves, the auxiliary drive supplies a larger fraction of the total power. It is deposited near the wall and easily escapes.

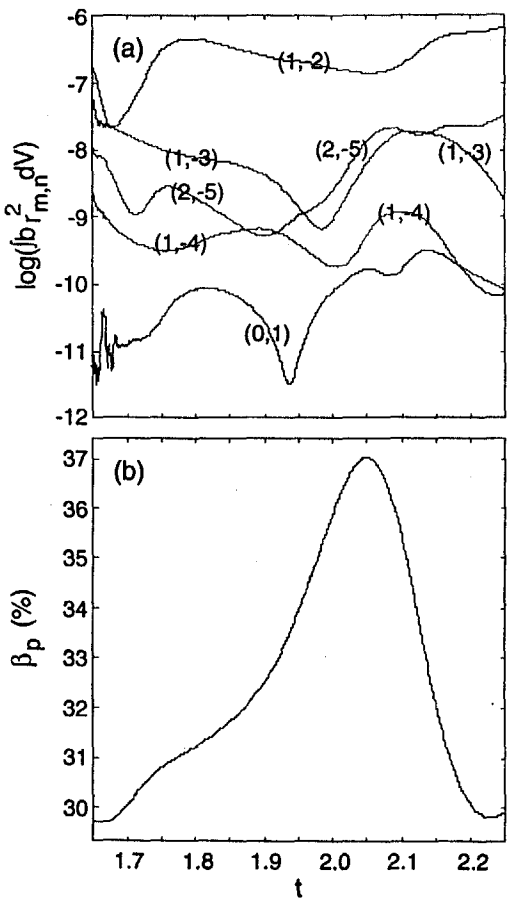

Figure 4.22 Time histories of (a) modal magnetic energy [reduced by 2^{10}] and (b) β_p from the time when the pressure terms are eliminated.

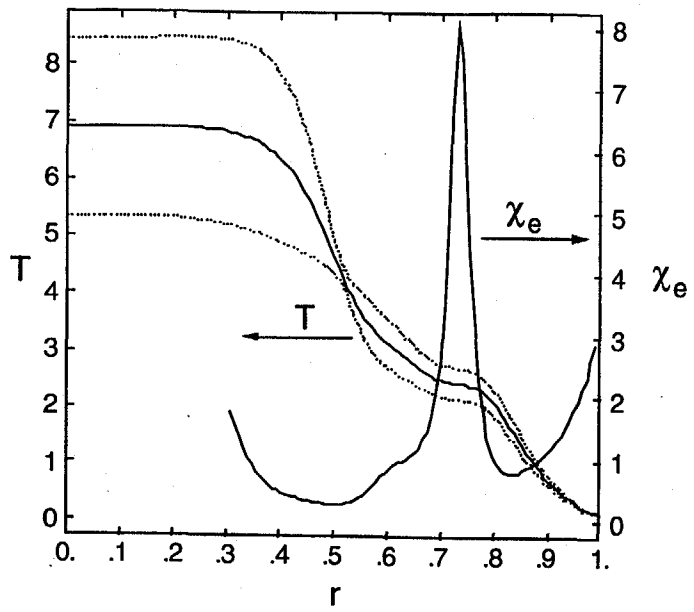

Figure 4.23 Radial profiles of mean temperature and effective diffusivity over the time 1.85≤t≤2.25 for the simulation without pressure terms.

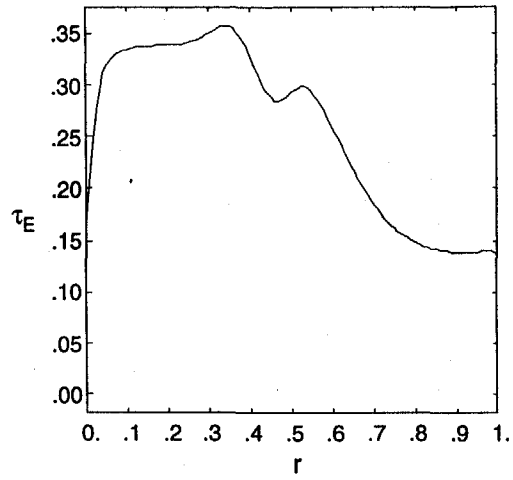

Figure 4.24 Radial profile of energy transit time for the simulation with auxiliary drive with the pressure terms removed.

4.3 DC Helicity Injection in RFPs

When the current profile is modified with an electrostatic potential, MHD equations can model the coupled issues of helicity injection and fluctuation suppression. The injection does not depend on high-frequency effects, and the length scales of the induced perturbations are macroscopic. In fact, MHD effects associated with DC helicity injection cannot be ignored. While some configurations reduce fluctuations, others sustain them through nonlinear coupling. The MHD model is not complete, however. Electrodes force current across plasma-solid interfaces, where sheaths will exist in experiment. Charge separation effects in these regions are outside the scope of a single-fluid treatment, so electrode

surfaces in the MHD model necessarily represent the plasma side of any sheath. In addition, the driven current may be carried by fast electrons with mean-free-paths are long in comparison to other length scales. If the resulting nonlocal conductivity is important, a kinetic treatment is necessary.

Earlier DEBS results demonstrate reduced fluctuation levels with two electrode geometries (Ho, 1991). The first is an axially symmetric configuration, which is illustrated in Fig. 4.25. A divertor coil draws magnetic field through electrodes that are flush with the chamber wall, and current is driven in the plasma exterior when a potential is applied. The resulting current density has an (m=0, n=0) Fourier component, so it directly affects the λ profile. In terms of power, this configuration is a combination of the RFP and the spheromak, which is driven by DC helicity injection alone (Jarboe, 1994). With both inductive drive for axial current and helicity injection for azimuthal current, power is distributed evenly to avoid dynamo activity.

This configuration has two drawbacks. First, it would be difficult to implement a symmetric electrode/divertor system in an existing device such as MST. Second, RFP configurations have large amounts of poloidal current, and a symmetric electrode must drive all current on the intercepted field lines (Ho, 1992). This leads to a large current requirement for the electrode circuit, which is not practical. Ho therefore proposed an asymmetric or 'localized' system such that field lines intercepted by the electrodes make several poloidal passes. This reduces the current requirement and increases impedance, because the current takes a longer path through the resistive plasma. The patterns formed by the electrodes on the chamber wall are compared in Fig. 4.26, along with two others configurations. The axially symmetric electrodes induce electrostatic field with m≠0, n=0 Fourier components, but the localized electrodes generate a broad spectrum.

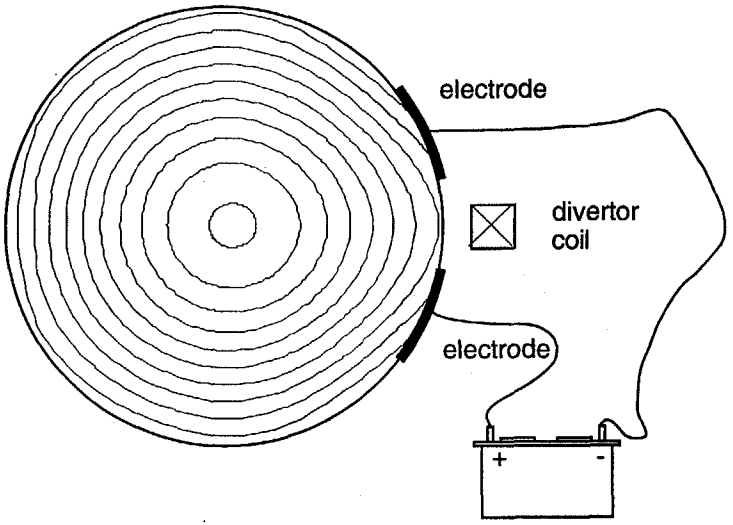

Figure 4.25 Sketch of the axially symmetric injection system (r-θ plane), superimposed on poloidal flux contours from simulation. The electrodes are insulated from the rest of the wall, and injected current follows magnetic field lines—which lie along the flux contours—from one electrode to the other.

Ho's results were obtained with the plasma parameters, $S=10^3$ and $R/a=1.25$—conditions that impede nonlinear interactions (see Section 3.3). To test the axially symmetric injection in more realistic conditions, it is simulated with $S=10^4$ and $R/a=3$. To provide adequate resolution for both the fluctuations and the injection, the modal resolution is $0\le m\le 5$ and $-42\le n\le 42$. The injected current and diverted flux are increased simultaneously over 0.05 τ_r, beginning from another simulation that has reached the quasi-steady state. Boundary conditions on the vector

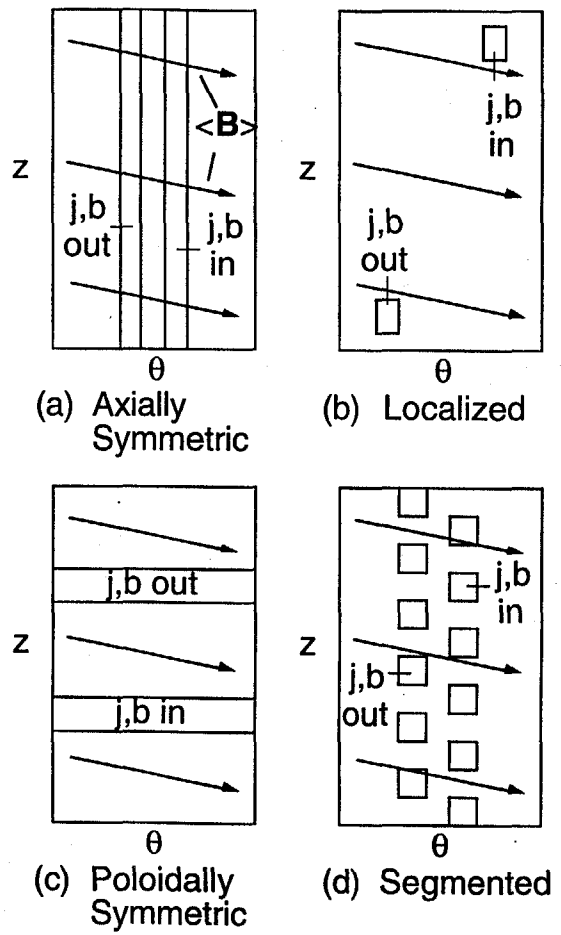

Figure 4.26 Electrode patterns on the plasma surface (r=1 plane) for the geometries discussed in this section. Ho considered the axially symmetric and localized configurations.

potential are specified such that j_r/b_r=3 at the electrode surface (see Section 2.1.1). The applied E_z is adjusted to keep the total input power at its initial value. This reduces Θ from 1.46 to 1.20, and the final configuration has very weak reversal ($F = -0.03$). The divertor draws approximately 25% of the poloidal flux through the electrodes, and the injected current is large. At the end of the simulation, it is 70% greater than the axial current. In addition, the electrostatic injection supplies 70% of the total power.

The parallel current profiles with and without injection are shown in Fig. 4.27. Penetration of the injected current depends on the resistivity profile, which has the usual $\left(1+9r^{30}\right)^2$ distribution. Most of the injected current therefore remains near

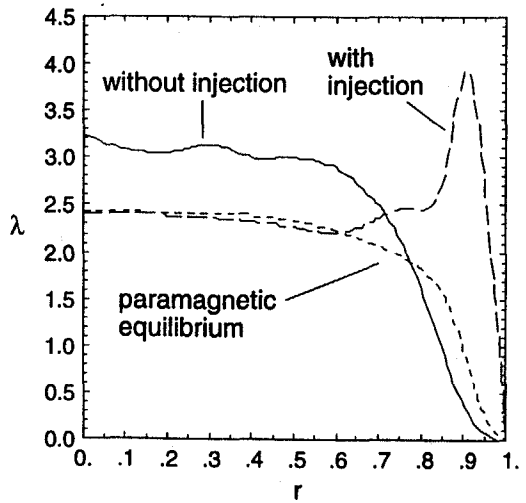

Figure 4.27 Comparison of parallel current profiles with and without axially symmetric helicity injection. Also plotted is a paramagnetic equilibrium based on the E_z and $\langle B_z(r=0)\rangle$ from the simulation with injection.

the wall, and the change in the interior results from reducing E_z. There is less shear in the center of the plasma, so power from the normal inductive drive is spread over a larger fraction of the radius. The interior is essentially equivalent to that of a paramagnetic equilibrium, which would be stable with a flat resistivity profile. In the simulation, all resolved modes are stabilized. This last closed flux surface is 20% of the minor radius from the wall on the side opposite the divertor, and field lines beyond this point are open to the electrode surfaces (see Fig. 4.25).

Although the symmetric configuration has good stability properties, energy confinement is poor. A large fraction of the power is deposited in the exterior, where the magnetic field provides no insulation. Simulations of this configuration with finite pressure, thermal conduction, and temperature-dependent resistivity highlight the problem. When the divertor field exposes the outer plasma to the surface, thermal conduction increases. The injected current does not produce enough ohmic heating to compensate this loss, so the plasma cools, and the resistivity increases. This leads to enhanced penetration, exposing a larger fraction of the plasma to the surface. The confinement time plummets before any MHD stabilization can take place. Larger injected current densities with less diverted flux may reduce the cooling, but this has not been verified.

In the localized configuration, the injected current has a much longer path length. As injection is applied in S=1000, R/a=1.25 simulations, the energy of the largest internally resonant mode drops by two orders of magnitude. Current-filament tracing shows that the injected current makes several poloidal passes, while making one axial pass. Calculations of $-\int\left\langle \mathbf{v}_{m,n}\times\mathbf{b}^{*}_{m,n}\right\rangle\cdot\langle\mathbf{J}\rangle d\mathbf{x}$ for modes induced by the injection show that power is delivered to mean current density predominantly through the (0,1) Fourier component, i.e., through the axial component of the electrostatic field. The poloidally symmetric configuration of Fig.

4.26c therefore represents the important aspects of the localized configuration. Simulation results of parallel current profiles (see Fig. 4.28) and fluctuation reduction are very similar. I have therefore used the poloidally symmetric configuration as a representative of all configurations with two axially separated electrodes.

When poloidally symmetric injection is applied in larger aspect ratios, the stabilizing effect is diminished. The configuration has been tested in series of simulations with R/a=2.5, S=10^3, and j_r/b_r at the electrode surface varied from 2.5 to 7.5. At best, the largest internally resonant modes are reduced by a factor of three in energy (see Fig. 4.29). When the injection is increased beyond this point, the

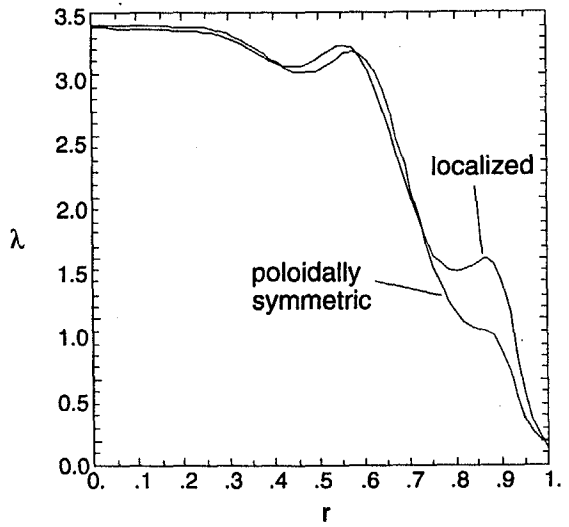

Figure 4.28 Comparison of parallel current profiles that result from the localized configuration and the poloidally symmetric configuration at S=10^3 and R/a=1.25.

fluctuations become larger. The parallel current profiles are similar to the small aspect ratio cases (compare Figs. 4.28 and 4.30), so linear stability properties are similar. The difference lies in the nonlinear properties. For a relatively large aspect ratio, the safety factor is small on axis, and there are more m=1 resonance surfaces nearby. Closely spaced modes interact readily, which leads to problems for this configuration.

The injection system delivers power by inducing m=0 perturbations that extend into the interior. [The axial electrostatic field cannot drive significant current in the exterior, because the magnetic field is azimuthal.] Most of the power sustains mean current or is dissipated directly, but approximately 10% couples with

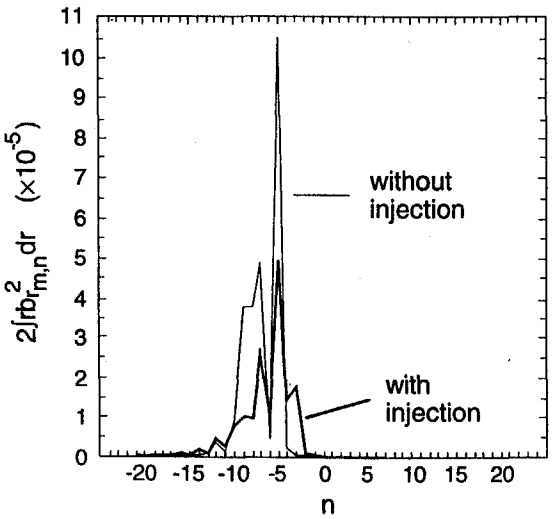

Figure 4.29 Magnetic energy spectra (radial component contribution) for m=1 modes with and without poloidally symmetric helicity injection from an R/a=2.5 simulation. This plot shows the largest reduction obtained.

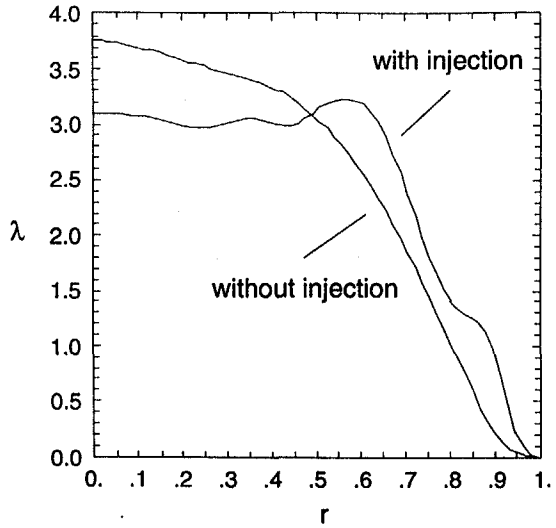

Figure 4.30 Parallel current profiles with and without poloidally symmetric helicity injection from R/a=2.5 simulations.

resonant modes. The (0,1) perturbation is the largest, and it couples fluctuations with the same poloidal mode number and consecutive axial mode numbers. This is evident in a comparison of the quasilinear power, $-\int \langle \mathbf{v}_{m,n} \times \mathbf{b}^*_{m,n} + \text{c.c.} \rangle \cdot \langle \mathbf{J} \rangle d\mathbf{x}$, with the total input power for the m=1 modes, which is shown in Fig. 4.31. The simulation is virtually steady, so the difference between the powers results from nonlinear interactions. For the (1,-4) and (1,-6) modes, the quasilinear input is less than the total, and nonlinear coupling sustains them. Furthermore, the alternating pattern of quasilinear-nonlinear sustainment implicates the (0,1) perturbation as the source of power.

The segmented configuration, illustrated in Fig 4.26d, combines practical aspects of the localized geometry with stability properties of the axially symmetric geometry. The electric field induced by this configuration has many Fourier components, but they are either n=0 or harmonics of the number of electrode segments (n_s). The harmonics include m=0 components, and three-wave interactions between the (0,n_s) perturbation and two m=1 modes can occur, but the m=1 fluctuations must have axial mode numbers that differ by n_s. If this number is large, coupling with an unstable mode must involve either nonresonant modes or stable fluctuations that are resonant near the reversal surface, so these nonlinear interactions are impeded.

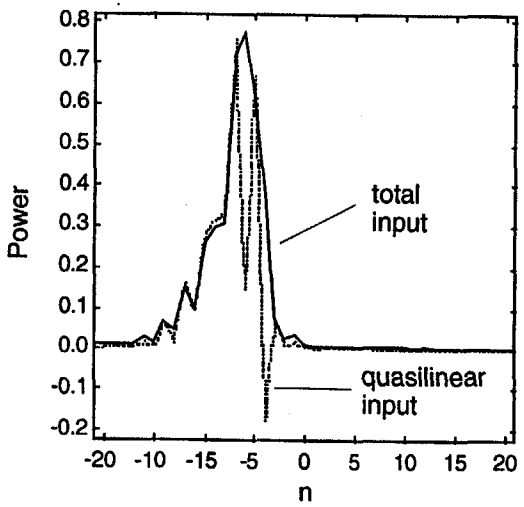

Figure 4.31 Input power for m=1 modes at the end of the poloidally symmetric injection simulation with R/a=2.5. The modes are nearly steady, and the total input is balanced by dissipation.

The segmented injection has been tested in simulations with S-values of 10^3 and 10^4. A simulation with $S=10^4$, R/a=3, n_s=6, and j_f/b_f=4 demonstrates the properties of this configuration. It is initiated from the simulation that served as the starting point for the axially symmetric case discussed above. The applied E_z is again adjusted to maintain constant total power, and at the end of the simulation, the injection supplies 50%. It is delivered to mean current through electrostatic field with the Fourier components, m≠0, n=0 and m=0, n=6. This produces the λ profile shown in Fig. 4.32, which is similar to the axisymmetric result.

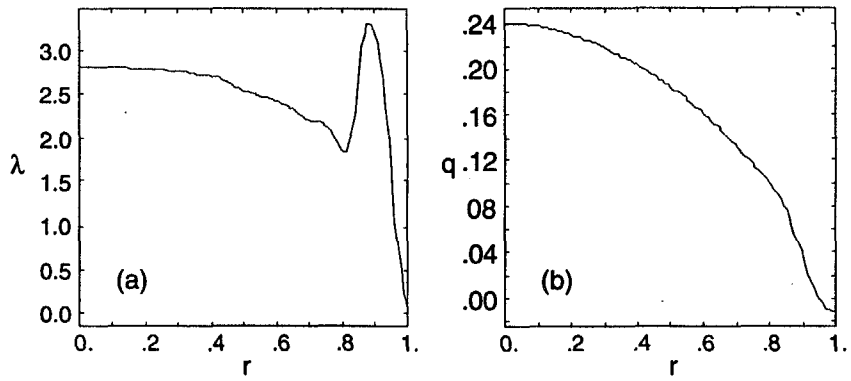

Figure 4.32 Radial profiles of (a) parallel current and (b) safety factor the $S=10^4$, R/a=3 simulation with the segmented injection geometry.

The internally resonant m=1 fluctuations are reduced by two orders of magnitude, with the exception of the (1,-6) mode (see Fig. 4.33). Harmonics of the injector periodicity are apparent across the spectrum, but most are small with the exception of the (1,0) and (0,$\pm n_s$) fundamentals, which deliver power. The (1,-6) mode is reduced from its original level, but the injection does not allow further decay. It leaves an island near its resonance surface, r=0.58, but there are closed flux surfaces in the plasma center (the field-line puncture plot is not shown). This configuration can be improved by increasing n_s. The internal mode perturbed by the injection would then be resonant at a larger radius, producing a larger region of closed flux surfaces.

This configuration is being developed for experiment in MST (Craig, 1995). The current injectors are miniature plasma guns that are mounted on probes and inserted into the edge of the plasma. The magnetic field topology is the same as described here; field that diffuses into a probe is equivalent to the field diverted through the wall in the simulations. There will be twenty to thirty of these guns, so they should not induce large internal islands. They also minimize the thermal conduction loss, which destroyed confinement in the finite-pressure simulation with axisymmetric injection. The guns are no larger than other probes that are commonly inserted, and their presence does not reduce confinement.

The simulations in this section show that the electrode geometry used for DC helicity injection determines much of the resulting behavior. When power is delivered by modes that couple to large internally resonant fluctuations, stabilization is precluded. However, the injection system can be designed to avoid these couplings, and the segmented configuration is one that meets these requirements.

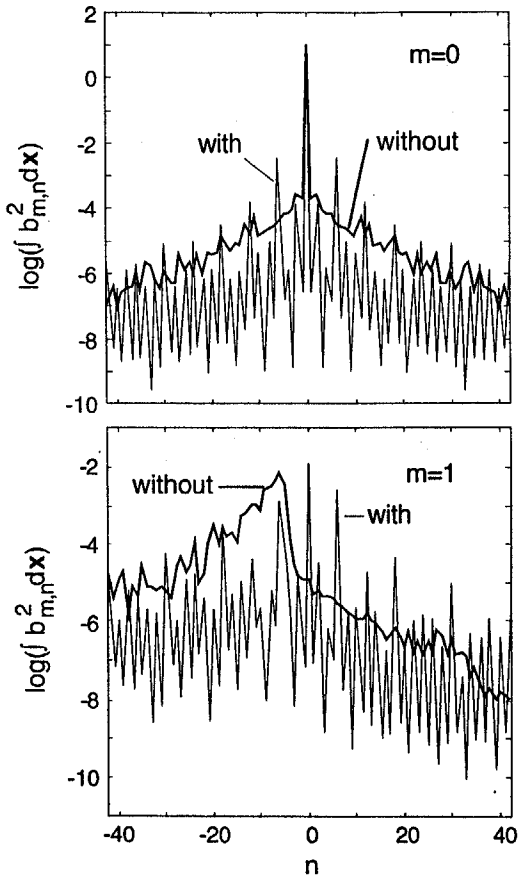

Figure 4.33 Magnetic fluctuation spectra for the m=0 and m=1 poloidal mode groups with and without the segmented injection.

4.4 Pulsed Poloidal Current Drive (PPCD)

A class of MST experiments has been devised to test the effects of current profile modification using hardware that exists for normal RFP operation. A pulse of poloidal electric field is applied to the discharge near the time of peak toroidal current. This inductive field enhances parallel current near the wall, which modifies the λ profile. Besides the inherently transient aspects, the effect is similar to DC injection or RF current drive. There is enhanced helicity dissipation from $-2\int\langle E_\theta\rangle\langle B_\theta\rangle dx$ in Eq. 1.3, but it is not sustained because there is no helicity injection. Toroidal flux is removed from the chamber, while the poloidal flux remains approximately constant, and a reduction of flux linkage results (Sarff, 1995). Evidence for fluctuation suppression is observed in the magnetic coil array, which shows an absence of the usual periodic growth of internally resonant modes. It also comes from calculations of energy confinement time, where a factor of two improvement is found (Sarff, 1994).

The numerical simulation discussed in this section is one of several that show fluctuation suppression resulting from PPCD. In this case, $S=10^4$, $R/a=3$, $E_z=3.8$, $\Phi=0.674$, and the starting point is t=0.3 of the simulation discussed in Section 2.1.1. [This was also used as the start of the two large-Θ, auxiliary drive cases in Section 4.2.1.] The boundary conditions on the vector potential are used to apply the poloidal 'voltage' pulse illustrated in Fig. 4.34, which approximates the sharp rise and slow decay of the pulse applied in MST. One-fourth of the axial (toroidal) flux is extracted, and in the simulation, the plasma cannot recover because $\langle E_\theta\rangle$ returns to zero. The duration of the pulse is chosen with respect to tearing mode dynamics. Since the simulation and experiment have Lundquist numbers that differ by two orders of magnitude, it would be incorrect to scale the pulse length with respect to either τ_a or τ_r. The MST pulse duration is approximately 5 ms,

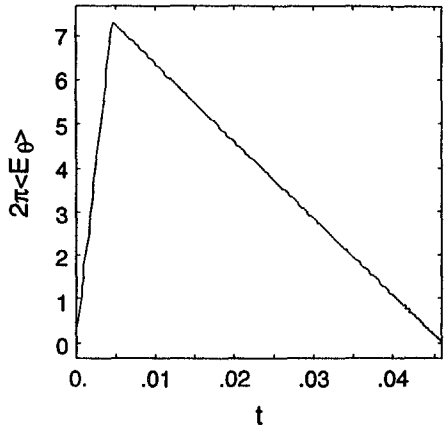

Figure 4.34 Pulse of poloidal potential applied to the plasma surface in the PPCD simulation. Here, t=0 corresponds to t=0.3 of the simulation discussed in Section 2.1.1.

which is an order of magnitude larger than the geometric mean of τ_a and τ_r. In this $S=10^4$ simulation, the pulse is applied over 0.046 τ_r. For both experiment and simulation, the pulse length is therefore comparable to the respective oscillation period in *F*.

Removing flux leads to a commensurate increase in the pinch parameter, as shown in Fig. 4.35. In contrast, Θ is virtually constant under the same conditions without the pulse. [E_z is fixed and not adjusted to maintain constant Θ.] The drop in *F* is proportionately larger, because the change in $\langle B_z\rangle$ is concentrated near the wall. The evolution of these global parameters may be compared with the same quantities from an MST discharge with PPCD, shown in Fig. 4.36. With the exception of high frequency oscillations in the experimental traces, the evolution is

qualitatively similar over the first 60% of the pulse. The oscillations are attributed to m=0 activity (Sarff, 1994), which may be suppressed at the S-value of this simulation (see Section 3.3). There is violent activity near the end of the pulse in both experiment and simulation. In MST, the large sawtooth recovers the extracted flux from external inductance, while in the simulation, recovery is prevented. The pulse has a dramatic effect on the magnetic fluctuations. For the first 0.005 τ_r, modal evolution is unchanged, but thereafter the resonant modes decay steadily (see Fig. 4.37). The (1,-5) mode is strongly suppressed because it does not regain resonance, unlike the simulation without PPCD (see Fig. 4.38). For all m=1 modes, the simulated behavior compares very well with the MST data shown in Fig. 4.39. Suppression of the 'axis mode' appears identical, and the first resonant mode remains largest. With respect to MST results from a similar discharge without PPCD (Fig. 3.25), there is an effective reduction in fluctuation amplitude by more than 50% relative to the periodic maximums. The numerical result in Fig. 4.37 is similar, though the simulation without PPCD does not have clear sawteeth.

The mechanism behind the fluctuation suppression is the change in quasilinear power that results from the parallel current modification. The λ profile and dynamo power density from m=1 modes are plotted in Fig. 4.40 at four different times during the simulation. When the modes are decaying, $\lambda(r\cong 0.7)$ is sustained a standard deviation above average, relative to normal temporal fluctuations (compare with Fig. 2.4a). This makes the dynamo power relatively large in the region where energy is extracted from the fluctuations. The pulse continues to propagate inward, however, leading to a narrow current profile at $t=3.68\times10^{-2}$. Additional power is then supplied to the modes, enhancing their growth rates until a violent crash in *F* occurs at $t=4.2\times10^{-2}$ (see Figs. 4.35 and 4.37).

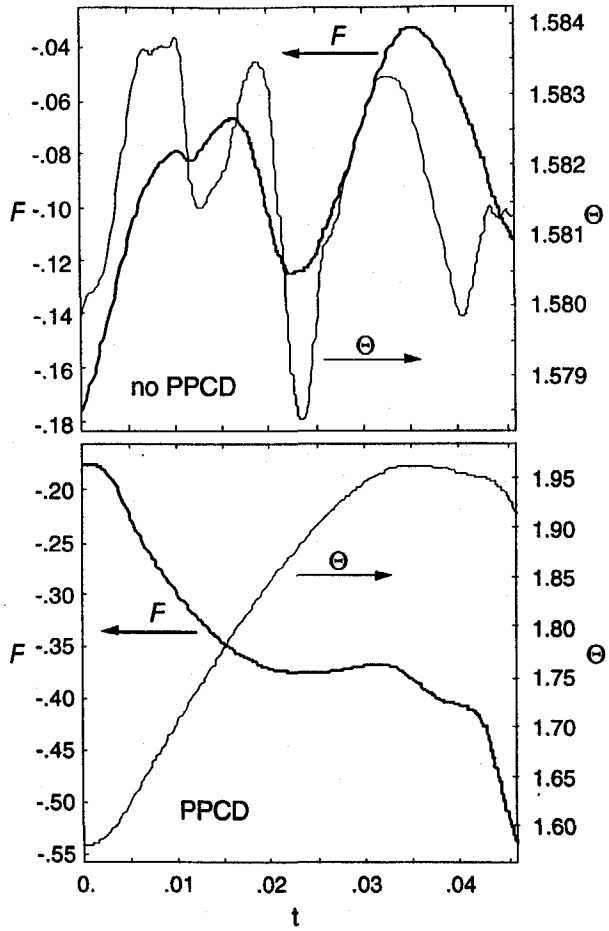

Figure 4.35 Evolution of reversal and pinch parameters for the simulations with and without the PPCD pulse, where both are started from the same conditions.

Since the change in modal behavior is a direct consequence of the modified parallel current profile, the increased confinement time resulting from PPCD is experimental proof of benefits possible with RF current drive or DC helicity injection. The degree of similarity between the simulation and experiment also stresses the importance of MHD activity in RFPs.

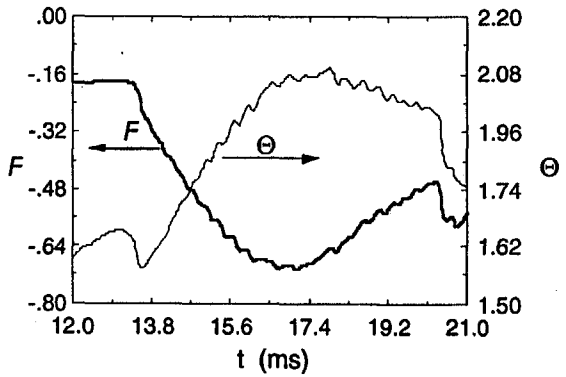

Figure 4.36 Evolution of reversal and pinch parameters from MST shot #73, October 20, 1995. The PPCD pulse is applied at t=13.5ms. [Data courtesy of John Sarff.]

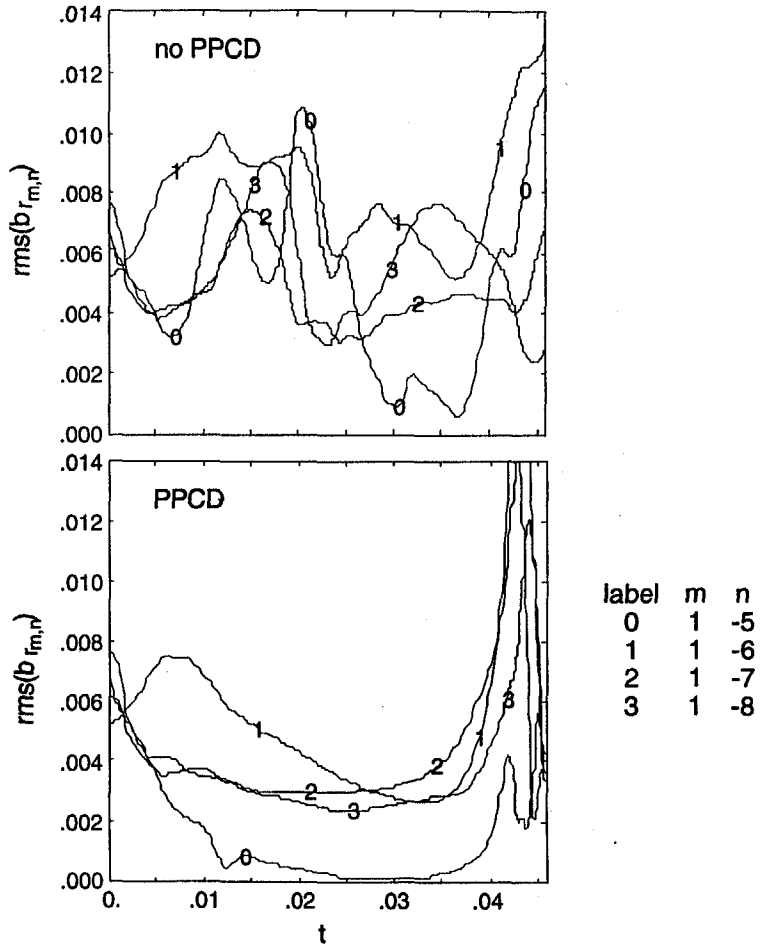

Figure 4.37 Time histories of $\mathrm{rms}\left(b_{r_{m,n}}\right) = 2\sqrt{\int_0^1 b_{r_{m,n}} b^*_{r_{m,n}} r dr}$ for the largest m=1 modes in the simulations with and without PPCD.

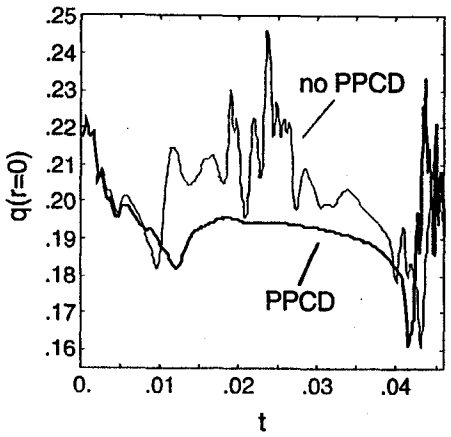

Figure 4.38 Evolution of the safety factor on axis for the two simulations.

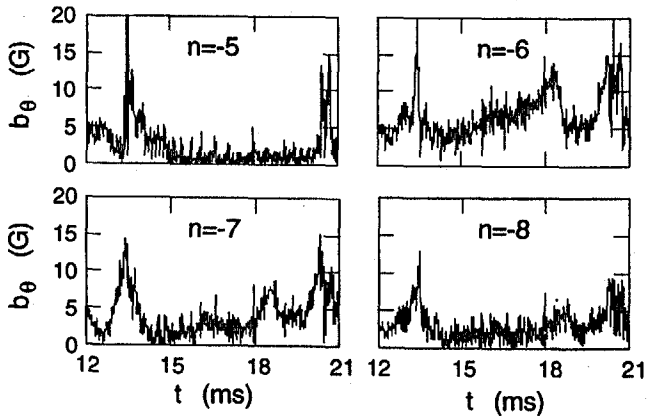

Figure 4.39 Poloidal components of magnetic fluctuations from the MST experiment with PPCD applied at t=13.5ms (shot #73, October 20, 1995). [Data courtesy of John Sarff.]

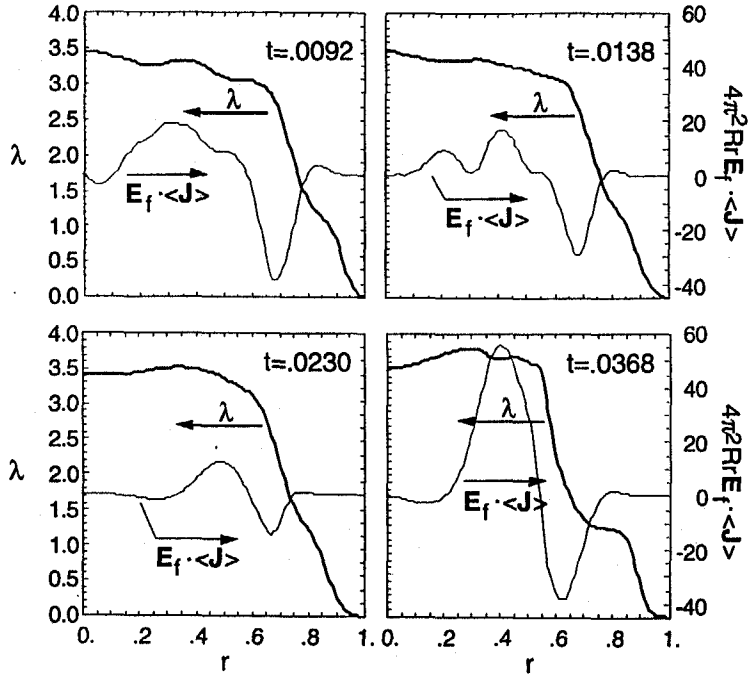

Figure 4.40 Four sets of radial profiles showing parallel current and dynamo power density from m=1 modes during the simulated PPCD pulse. The fluctuations are decaying at the time of the first two sets, beginning growth at the third, and growing strongly at the fourth.

References

V. Antoni, D. Merlin, S. Ortoloni, R. Paccagnella, "MHD Stability Analysis of Force-free Reversed Field Pinch Configurations," Nucl. Fusion **26**, 1711 (1986).

D. Craig, A. Almagri, G. Fiksel, M. Iida, S. Oliva, S. C. Prager, J. S. Sarff, and M. A. Thomas, "Current Profile Control and Fluctuation Reduction in MST via Electrostatic Current Injection," Bull. Am. Phys. Soc. **40**, (1995).

N. J. Fisch, "Confining a Tokamak Plasma with RF-Driven Current," Phys. Rev. Lett. **41**, 873 (1978).

Y. L. Ho, "Numerical Simulation of Fluctuation Suppression via DC Helicity Injection in a Reversed-field Pinch," Nucl. Fusion **31**, 341 (1991).

Y. L. Ho, private communication (1992).

J. Li and D. Liu, "Tearing Mode in RFP Configurations," Alfven Laboratory Report ISSN 1102-2051, Stockholm, Sweden (1995).

J. Sarff, S. A. Hokin, H. Ji, S. C. Prager, and C. R. Sovinec, "Fluctuation and Transport Reduction in a Reversed Field Pinch by Inductive Poloidal Current Drive," Phys. Rev. Lett. **72**, 3670 (1994).

J. Sarff, private communication (1995).

S. Shiina, K. Saito, Y. Kondoh, H. Ishii, T. Shimada, Y. Hirano, "Current Density Profile Control in Reversed Field Pinch Plasma by RF Current Drive," in *Proceedings of the 19th European Physical Society Conference on Controlled Fusion and Plasma Physics*, II-917, (Innsbruck, 1992).

E. Uchimoto, M. Cekic, R. W. Harvey, C. Litwin, S. C. Prager, J. S. Sarff, and C. R. Sovinec, "Lower-hybrid Poloidal Current Drive for Fluctuation Reduction in a Reversed Field Pinch," Phys. Plasmas **1**, 3517 (1994).

5. DC HELICITY INJECTION FOR TOKAMAKS

Nearly all toroidal plasma devices use an inductive electric field to drive toroidal current. A changing magnetic flux is imposed through the center of the 'doughnut hole' until an engineering limit on the flux is reached. This works well for experiments, where pulsed operation is acceptable; however, it is not very attractive for future commercial power generation. Over the past two decades, RF and neutral beam techniques have been developed with a great deal of success, but both have limitations. A recently proposed innovation for tokamaks is to use DC helicity injection to drive the toroidal current (Jensen, 1984 and Jarboe, 1988). The helicity injection itself is similar to the injection discussed in Chapter 4, but the intended result is quite different. Here the injected current creates an *unstable* current profile, and MHD fluctuations are expected to relax the configuration into one that resembles a tokamak.

This concept is very similar to the spheromak, where DC helicity injection alone sustains the discharge (Jarboe, 1994). The Taylor hypothesis (Taylor, 1974; also see Chapter 1) has been used as a justification for expectations of complete relaxation to a tokamak-like configuration. However, unlike RFPs and spheromaks, tokamaks have a large toroidal field which is stabilizing by design. Ordinary, inductively-driven tokamaks run with peaked current profiles, and the same hypothesis can be applied to argue that these profiles should relax. They don't. Therefore, the question of how much relaxation can be expected when DC injection is applied on a large toroidal field needs to be addressed. In addition, magnetic fluctuations have the same deleterious effect on energy confinement in tokamaks that they do in RFPs. An assessment of the extent of this effect requires a Lundquist number scaling to extrapolate beyond present-day experiments.

DC helicity injection has been explored experimentally on the Current Drive Experiment (CDX; Ono, 1987 and Darrow, 1990), the Continuous Current Tokamak (CCT; Darrow, 1990), and the Helicity Injected Tokamak (HIT; Nelson, 1994). The CDX and CCT configurations use a toroidally local cathode that is mounted near the surface of the chamber. The cathode emits an electron beam in one toroidal direction, and a vertical magnetic field deflects the beam toward the center of the chamber. Probe measurements indicate that the current is peaked within a poloidal cross-section of 3 cm minor radius (Ono, 1987). The discharge is adjacent to the cathode and does not occupy the entire 10 cm minor radius chamber. In HIT, a magnetized coaxial plasma gun is used as a source of plasma and for toroidally symmetric helicity injection. Profile information—reconstructed from surface probe data by an equilibrium code—indicates substantial relaxation (Nelson, 1994). According to this reconstruction, the discharge fills the chamber and generates closed poloidal flux contours.

With the usual limitations on Lundquist number and geometry, the DEBS code is a suitable tool for a numerical investigation of this concept. Except for the modifications to the boundary conditions discussed in Chapter 2 and below, the helicity injection is simulated in the same fashion as it is in the RFP simulations. One may set the mean axial electric field to zero to produce a discharge with no 'loop voltage,' and current is therefore induced by DC injection alone. When the profile becomes unstable, MHD fluctuations grow, interact and affect the mean current distribution. This entire process is modeled self-consistently with DEBS.

It is convenient to classify the simulations by the level of applied electric field. In the weak-drive limit, the parallel current profile is flat, and there are no MHD modes and no flux surfaces. This amounts to the generation of a magnetically-guided, diffuse electron beam. This limit is relatively uninteresting, but it demonstrates the

sustainment of axial current without 'loop voltage.' When the applied electric field is large, the induced current distorts the poloidal field, which in turn distorts the current path. This produces hollow current profiles that are unstable to resistive MHD modes.

The following section is devoted to the modeled geometry, the significance of the boundary conditions, the resistivity profile, and numerical resolution. General results are discussed in Section 5.2, which is organized into a subsection for the weak-drive limit and a subsection for strong drive and relaxation. Section 5.3 discusses the significance of several parameters that have been varied to determine the sensitivity of the relaxation process. Finally, information on the Lundquist number scaling of the relaxation and fluctuation level is presented in Section 5.4.

5.1 Geometry and Simulation-related Information

As mentioned in Chapter 2, I have used the pressureless version of DEBS for these simulations. The periodic cylinder domain again implies geometric limitations; there are no toroidal effects, and complicated injector systems must be simplified. The configuration that has been used for all but one simulation is shown in Fig. 5.1. The applied vacuum fields, $\mathbf{E_V}$ and $\mathbf{B_V}$ of Eq. 1.3, are vertical and axially symmetric. It is possible to use vacuum fields that are not uniform, as is done in the RFP simulations in Chapter 4. However, the vertical field configuration is the simplest possible configuration that has the same magnetic field topology as the HIT experiment. It therefore represents the concept in a generic fashion, and it is easy to analyze. The one exception to the simple arrangement uses the vertical $\mathbf{E_V}$ with the vacuum magnetic field distribution from a line of current outside the cylinder. This case is discussed in Section 5.3.2.

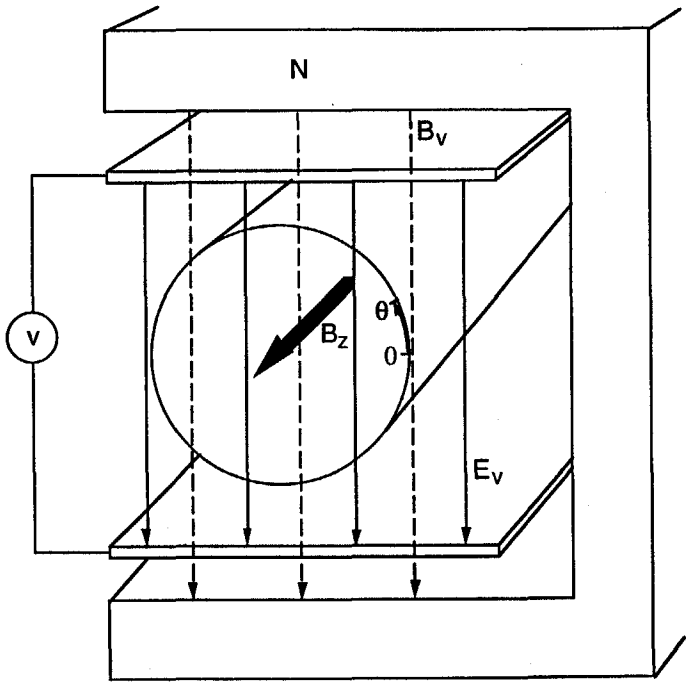

Figure 5.1 Schematic of the applied fields for DC injection (poloidal slice illustrated). Only the region within the periodic cylinder contains plasma and is in the problem domain. The orientation of θ=0 is shown for the I_{inj} definition.

The **ExB** drift velocity is used as a boundary condition on **V**, and the simulations do not model the region where plasma is accelerated. In HIT there is a magnetized plasma gun that is adjacent to the 'confinement' region, where the main discharge forms (Nelson, 1994). The gun ionizes gas and sustains a perpendicular current to accelerate the plasma into the 'confinement' region. If one were to set the velocity to zero at the boundary of the simulations, the applied

potential would drive a perpendicular current like the HIT gun. This would accelerate plasma away from the boundary, but it would also create a large divergence in **V**. If the number density were evolved with a source term from ionization, the process would be modeled self-consistently. To concentrate on the physics of the relaxation, the drift velocity is used, and the numerical domain is strictly within the 'confinement' region. When $\mathbf{B}_V$ is set to zero, there is no helicity injection, and applying the potential produces a drift across the entire domain without inducing current.

The choice of the velocity boundary condition is also related to the choice of resistivity profile. Hollow current profiles develop when large electrostatic potentials are applied, and they are sensitive to the edge resistivity. Though it may be unrealistic, a flat resistivity profile is used for all but one simulation. The intention is to learn general information concerning the nature of the MHD activity, and a simple configuration provides the most general results. The RFP simulations in the previous chapters are not as sensitive to the velocity boundary conditions. Current profiles peak on axis, and any perpendicular currents near the wall are small because the edge resistivity is realistically large.

The simulations that have been completed for the nonlinear S-scaling in Section 5.4.1 have $|n|\leq 5$ axial modes and $0\leq m\leq 10$ azimuthal modes resolved. This covers the dominant resonant modes and the important nonlinearly coupled modes. Comparisons in Section 5.3 are obtained with a reduced resolution of $|n|\leq 1$ and $0\leq m\leq 5$ or $0\leq m\leq 10$. This reduction has a moderate impact and does not change the salient features of the solutions—details are given in Section 5.4.1. As with the RFP simulations, the number of radial grid points needed for numerical stability depends on S. However, steep current gradients are generated by the tokamak injection and require better resolution than RFP simulations at the same

value of S. Hyper-dissipation terms are not applied, and 509 radial cells are used for the largest Lundquist number case, $S=2\times10^4$.

5.2 General Results

The helicity injection simulations are initialized with a large uniform axial magnetic field, a vertical magnetic field, and small random perturbations in the vector potential. The normal component of magnetic field at the surface determines $\mathbf{B}_V$ and is fixed for all time. The electrostatic potential is initially zero, and its level is increased over the first 0.1 or 0.2 τ_r. After this ramp phase, the potential is held constant to sustain the injected current against resistive loss. The current enters the domain on the top of the cylinder in Fig. 5.1 and leaves when it reaches the bottom. It is driven by the component of $\mathbf{E}_V$ that is parallel to the magnetic field, as sketched in Fig. 5.2. This also injects helicity through the $2\int \mathbf{E}_V \cdot \mathbf{B}_V d\mathbf{x}$ term of Eq. 1.3. The current density vectors are primarily axial, but there is no net axial electric field or 'loop voltage,' because the axial component of $\mathbf{V}\times\mathbf{B}$ cancels ηJ_Z. If the applied potential is reduced, the current decays.

5.2.1 Weak-drive Results

When the applied potential is small, the magnetic field remains essentially unaltered from vacuum conditions, and current simply follows the field lines. Results from a weakly driven simulation show a λ profile that is rather flat (Fig. 5.3a), and the axially-symmetric poloidal flux contours are only slightly distorted from their vacuum state (Fig. 5.3b). When the electrostatic field is nearly zero, the magnetic fields are identical to the vacuum fields—the induced current is too small to produce any distortion. In this limit, the parallel current has the uniform value of $E_V B_V/\eta B^2$, when the resistivity is uniform.

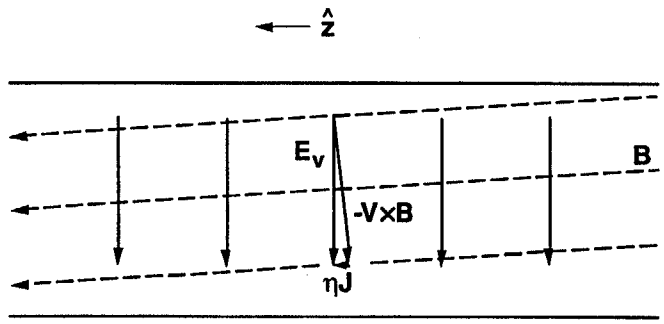

Figure 5.2 Sketch of the electric and magnetic fields upon application of the potential. The net axial electric field is zero.

A commonly used performance parameter for tokamak injection is the ratio of axial current to injected current. For the geometry shown in Fig. 5.1, the two currents are

$$I_z = \int_0^{2\pi}\int_0^{a} J_z r dr d\theta \quad \text{and}$$

$$I_{inj} = -\int_0^{\pi}\int_0^{2\pi R} J_r dz a d\theta \,,$$

respectively, with the indicated orientation of θ=0. In the weak-drive limit, the ratio is determined by the magnitude of the vertical magnetic field: $I_z/I_{inj} = aB_z/4RB_v$. For the simulation parameters, where the aspect ratio (R/a) is 6 and B_V=0.0125 (normalized to the initial B_Z), the ratio is 3.33 in the limit, while the simulation result is 3.23.

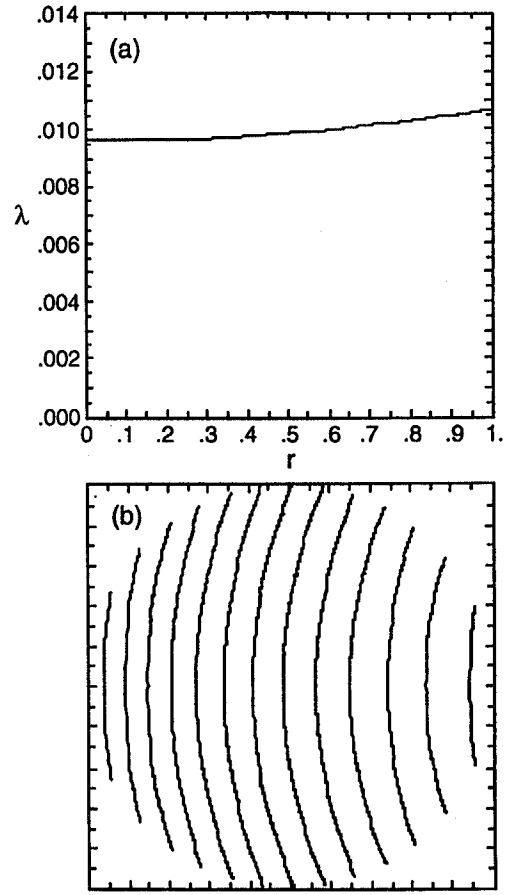

Figure 5.3 Weak-drive steady-state results of (a) parallel current and (b) axially-symmetric poloidal flux contours from an S=5000, R/a=6 simulation. The magnitude of E_V is 0.8. If there were no magnetic field distortion, λ would be 0.010.

5.2.2 Strong-drive and Relaxation

When the applied electrostatic potential is increased to a large level, the induced axial current generates poloidal magnetic field that is larger than the vertical field. This forces the poloidal flux toward the surface of the cylinder. The evolution is clearly shown in frames (a)-(c) of Fig. 5.4, a time sequence of axially-symmetric poloidal flux contours from a simulation with a large final potential. The distortion of the poloidal flux is accompanied by a distortion of the current path, and the λ profile becomes quite hollow when the full potential is applied. The solid λ trace in Fig. 5.5 shows the unrelaxed state corresponding to the flux plot of Fig. 5.4c. Resistive MHD modes are unstable at this point but have not grown to an appreciable level. The modes subsequently saturate and relax the λ profile to the dashed trace in Fig. 5.5. Relaxation also produces the closed flux contours in Fig. 5.4d. The change in the λ profile is small, but the amplification of poloidal flux is more than 30%.

The path length of the injected current changes during the evolution of the configuration. As the poloidal field increases, the current density vectors become less axial and more poloidal. This reduces the I_z/I_{inj} ratio, as illustrated in the first 0.25 τ_r of Fig. 5.6 for the same simulation shown Figs. 5.4 and 5.5. The very early times are noisy when the injected current is small, and Alfven waves—generated by the application of the potential—are wiggling the fields. [The temporal resolution is better than it appears; the ratio is plotted every 50 time-steps.] Relaxation occurs between t=1.25 and t=1.55, and this increases the I_z/I_{inj} ratio slightly, but the post-relaxation value is much smaller than the weak-drive limit. At late times, the configuration settles into a true steady-state. This is an artifact of the $|n|\leq 1$ modal resolution, which is addressed later.

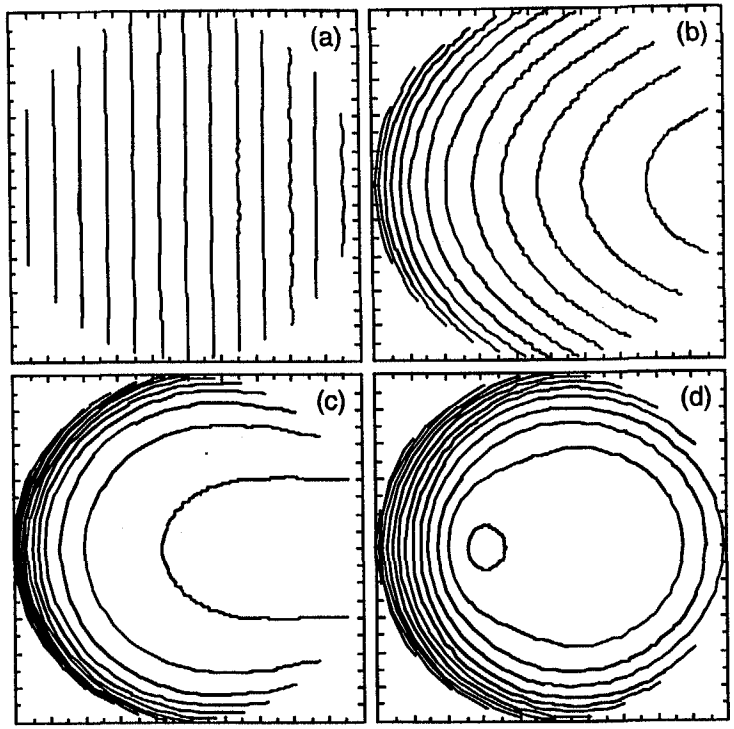

Figure 5.4 Temporal evolution of the axially-symmetric poloidal flux contours from a strongly-driven S=5000, R/a=6 simulation. The four plots show the (a) initial conditions prior to the application of electrostatic potential, (b) the point of half potential, (c) full potential with growing instabilities, and (d) the final relaxed state with saturated fluctuations.

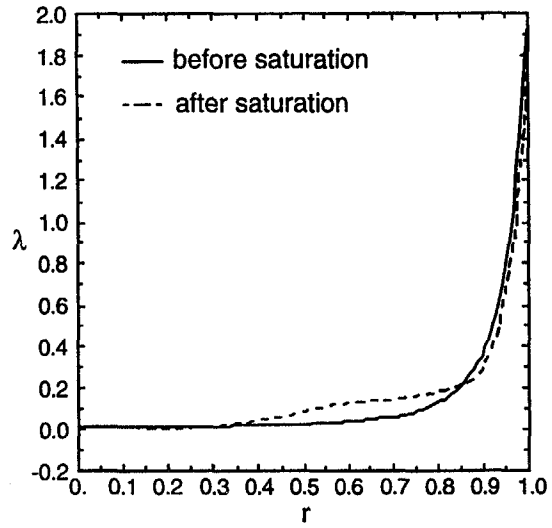

Figure 5.5 Parallel current profiles before and after the saturation of the fluctuations. This comparison shows the modest level of relaxation.

The MHD modes induce a net Poynting flux, and relaxation of the current profile occurs via the dynamo electric field, $\mathbf{E_f}=-\langle \mathbf{v}\times\mathbf{b}\rangle$. The $\mathbf{E_f}\cdot\langle \mathbf{J}\rangle$ distribution from the resonant n=1 modes (Fig. 5.7a) is positive in the exterior and negative in the interior. [To be consistent with most literature on tokamaks, resonant modes are labeled with n>0, as if the Fourier representation was $\sum f_{m,n}(r)e^{i(m\theta-nz/R)}$.] This represents an MHD dynamo that is driving interior current at the expense of exterior current. It is comparable to the MHD dynamo in the reversed-field pinch (see Chapter 3), but the $\mathbf{E_f}\cdot\langle \mathbf{J}\rangle$ distribution is flipped. Here, the electromagnetic energy transport from the resonant modes is inward. Fig. 5.7b shows a comparison of the $\langle \mathbf{e}\times\mathbf{b}\rangle_r$ Poynting flux from the resonant n=1 modes and that from the applied n=0 fields. The poloidal field distortion excludes the n=0 power from the interior, while

the resonant modes provide more penetration. The Poynting flux from a given resonant mode is not confined to its tearing layer; however, it is radially localized. Since the λ gradient is large near the wall, there is little drive for the fluctuations in the center of the cylinder. On the axis itself, only m=1 modes can have nonzero poloidal components of **v** and **b** to drive $\langle J_z\rangle$. None of the cases examined here have been driven so hard that an m=1 mode is resonant anywhere except near the wall. If a hollow current profile forced the safety factor below unity near the axis, the field configuration would bear more resemblance to a spheromak than a tokamak.

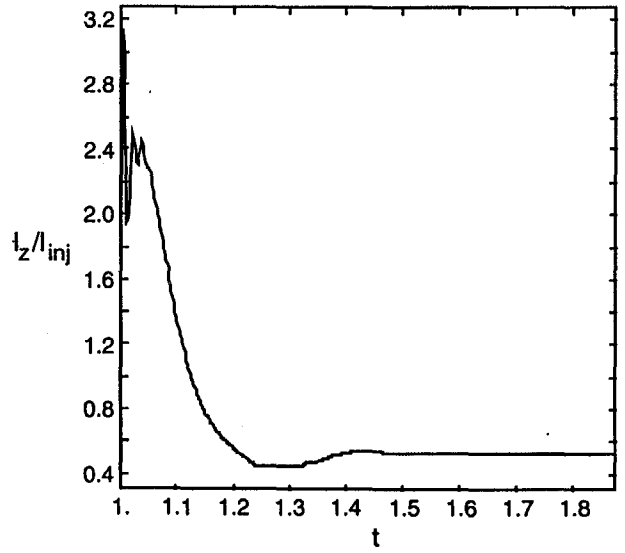

Figure 5.6 Time history of the ratio of axial current to injected current for the strongly-driven S=5000, R/a=6 simulation. The sequence of contours in Fig 5.4 represent the times 1.0, 1.125, 1.25 and 1.875. There is no applied potential during the first diffusion time, when B_v is established.

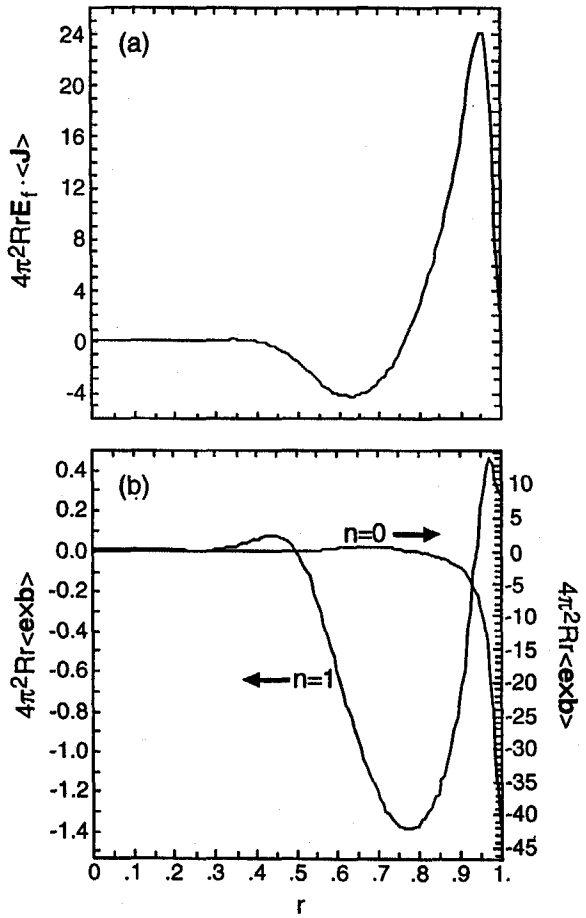

Figure 5.7 Relaxed-state distributions of (a) dynamo power density from n=1 modes and (b) radial Poynting fluxes induced by the applied fields (n=0 modes) and the resonant fluctuations (n=1 modes) overlaid with different y-axis scales.

The relaxation obviously falls short of producing a Taylor state. The fluctuations transport only about 3% of the injected power, and this is small relative to the 10% redistribution in the RFP (see Sect. 3.1), which also exhibits incomplete relaxation. Unlike the RFP, these 'tokamak' configurations have large axial fields, or equivalently, λ is small. This is stabilizing according to Eqs. 2.18 and 2.19; decreasing λ^2 reduces negative curvature in the linear eigenfunctions, which decreases Δ'.

Relaxation also comes with a price—the magnetic fluctuation level. The volume average of the fluctuation level is on the order of 1% of the axial field. The spectrum is broad and peaked at the n=1 mode which is resonant nearest the wall. This can be observed in Figs. 5.8 and 5.9, the magnetic energy spectrum and safety factor profile from the $S=2\times10^4$ case, where full modal resolution is used. The level of fluctuations is large enough to make the field lines stochastic in the region where the dynamo drives current. A comparison of poloidal flux contours with a field-line puncture plot, shown in Fig. 5.10, demonstrates that the flux surfaces formed by relaxation are not truly closed. Thus, energy and particle confinement would suffer from fast parallel transport mechanisms like the normal RFP configuration.

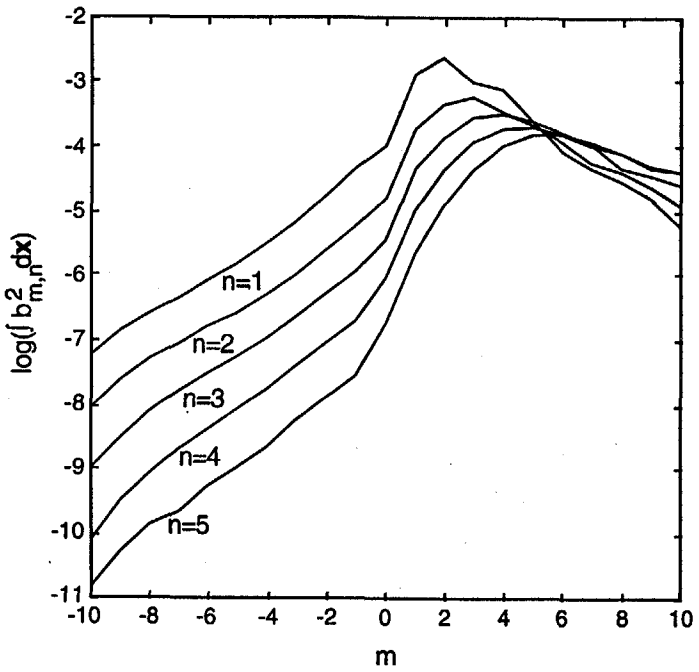

Figure 5.8 Magnetic energy spectra for the n≠0 modes from a fully resolved $S=2\times10^4$, R/a=6 simulation. There are temporal fluctuations, so spectra are averaged over 0.2 τ_r, and standard deviations are roughly 50% for all modes. The m>0, n<0 modes are denoted by their conjugate indices.

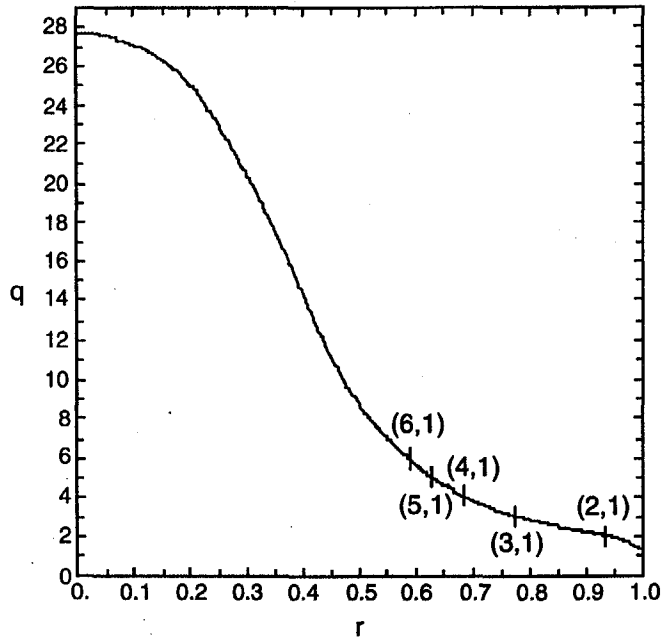

Figure 5.9 Safety factor ($q=r\langle B_z\rangle/R\langle B_\theta\rangle$) profile from the $S=2\times10^4$, R/a=6 simulation. The unusual shape is generated self-consistently by the DC helicity injection, and resonance surface locations are indicated for the largest modes. [This trace is actually the inverse of the time average of $R\langle B_\theta\rangle/r\langle B_z\rangle$. Fluctuations occasionally force $\langle B_\theta\rangle$ to zero near the axis.]

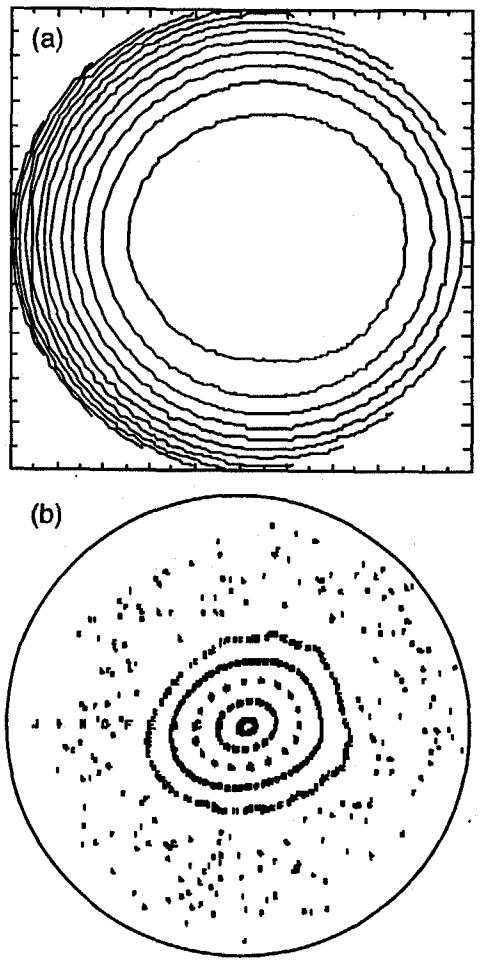

Figure 5.10 Comparison of (a) axially symmetric flux contours and (b) a field-line puncture plot for the $S=2\times10^4$, R/a=6 simulation.

5.3 Parameter Scans

The simulations with large applied potentials from the previous section show the two key features of the tokamak injection concept, axial current without loop voltage and poloidal flux amplification. What they do not show is a tokamak-like current profile, which—along with the safety factor profile—would be flat with the uniform resistivity and cylindrical geometry. I have tried to improve the performance, i.e., generate a flatter λ profile while retaining the closed flux contours, by varying the magnitudes of the applied fields, E_V and B_V. They are the externally controlled parameters for a given configuration, and results of the variations are discussed in Section 5.3.1. Other parameters such as viscosity, the resistivity profile, and aspect ratio are considered in Section 5.3.2, where the objective is to determine the sensitivity of the relaxation process and not optimization.

5.3.1 Applied Field Magnitudes

A series of simulations with S=5000, R/a=6 and only $|n|\leq1$ modes resolved has been conducted to explore the effects of varying the vertical field strength and the applied voltage. The results listed in Table 5.1 indicate the following trends: First, I_Z predictably increases with either E_V or with B_V. Second, both the fluctuation level ($|n|\neq0$ modes only to exclude the applied perturbations) and the poloidal flux amplification increase with E_V. Third, I_Z/I_{inj} decreases with increasing E_V or B_V—the increasing dynamo does not fully compensate the effect of the increasing poloidal field. Since the I_Z/I_{inj} ratio depends on both the applied fields and the dynamo, it provides a measure of relaxation only among cases where the applied fields are the same. However, the absolute (as opposed to %) flux generation always measures the level of dynamo-driven current.

Table 5.1 Helicity injection simulation results with S=5000 and $|n| \le 1$ modes resolved. The base parameters are ν=1, uniform resistivity, vertical applied fields, R/a=6, and constant axial flux; exceptions are noted for cases G-L. The helicity injection rate is $S_K = 2\int \mathbf{E_V} \cdot \mathbf{B_V} dx$.

case	E_V	B_V	S_K	I_{inj}	I_Z	I_Z/I_{inj}	flux amp.	rms(b) all n / n≠0
A	20	0.00833	39.5	0.80	0.52	0.65	< 1%	1.9% / 0.23%
B	25	0.00833	49.3	1.25	0.64	0.51	< 1%	2.1% / 0.25%
C	20	0.0125	59.2	1.49	0.78	0.52	32%	2.6% / 1.3%
D	30	0.0125	88.8	3.49	1.15	0.33	51%	3.0% / 1.4%
E	15	0.01875	66.6	1.89	0.86	0.46	22%	3.3% / 1.4%
F	20	0.01875	88.8	3.36	1.16	0.35	36%	3.6% / 1.6%
G[a]	15	0.01875	66.6	1.87	0.87	0.47	21%	3.3% / 1.4%
H[b]	30	0.0125	88.8	0.48	0.43	0.89	<< 1%	2.1% / 2.6×10^{-5}%
I[c]	30	0.0125[c]	73.8	1.77	0.96	0.54	< 1%	2.4% / 0.6%
J[d]	20	0.0125	19.7	0.58	0.77	1.33	< 1%	2.8% / 0.6%
K[e]	20	0.0125	98.7	2.49	0.78	0.31	30%	2.5% / 0.9%
L[f]	20	0.0125	59.2	1.45	0.77	0.53	32%	2.6% / 1.3%

[a]Viscosity is reduced by 4.

[b]Resistivity is a function of radius, $\eta(r) = \left(1+r^2\right)^2$.

[c]$B_V(a)$ is from an axial line current located at r=1.3a. The resulting poloidal flux through the cylinder is equivalent that in case C.

[d]R/a=2.

[e]R/a=10.

[f]Axial flux is allowed to change.

Although the flux amplification increases with E_V (and to some extent, with B_V), increasing the applied voltage does not enhance the flattening of the λ profile. The profiles for cases C and D are compared in Fig. 5.11. The parallel current in the relaxed region is larger for case D, but the spike of current at the wall is much larger, so the entire profile is actually more hollow. Also, the relaxed region is not pushed further in towards the axis. Increasing B_V makes the λ profile more hollow as well (see Fig. 5.12), but this does extend the relaxed region towards the axis. The difference lies in the effect of the applied fields on the resonance surfaces of the unstable modes. Increasing either E_V or B_V tends to decrease the safety factor at the wall. When E_V is increased, the evolution discussed in Section 5.2.2 is extended, moving the injected current path closer to the wall. The resonance surfaces of the largest modes do not move inward. In contrast, increasing B_V tends to move the current path and the resonance surfaces away from the wall.

These results shows that it is not possible to adjust the externally controllable parameters to generate current profiles that are closer to tokamak profiles. The current profile must be quite hollow to generate dynamo activity with the large axial field. After this threshold is crossed, further increases in the applied fields lead to more MHD dynamo, but the resulting current profile is increasingly more hollow, not less.

The distinction between changes in E_V and B_V leads to a more general conclusion: The final state can not depend on the helicity injection rate alone. The rate of helicity injection is $2\int \mathbf{E_V} \cdot \mathbf{B_V} dx$, and it is directly proportional to the product of E_V and B_V for the cases with vertical fields. Cases D and F in Table 5.1, for example, have the same helicity injection rate, but the resulting current profiles in Figs. 5.11 and 5.12 are not the same.

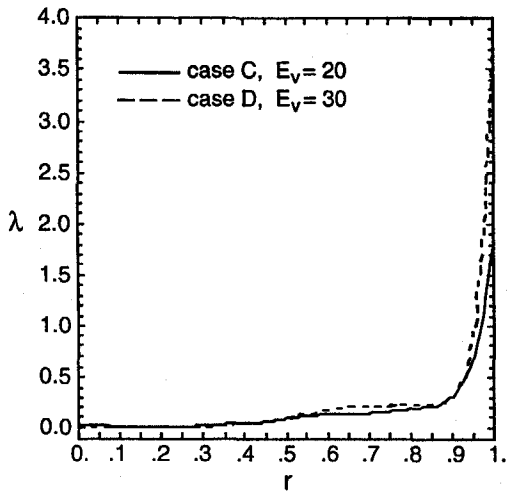

Figure 5.11. λ profiles from simulations with different applied potentials.

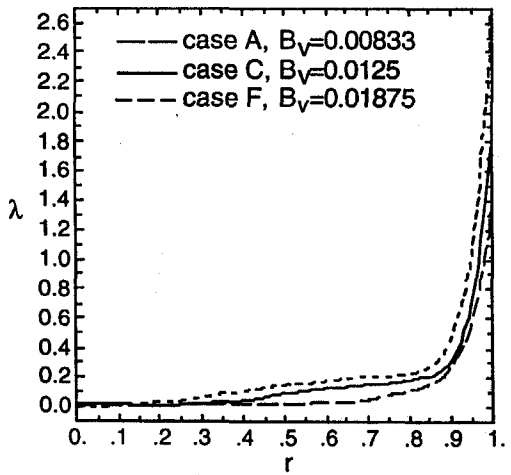

Figure 5.12. λ profiles from simulations with different vertical field magnitudes.

5.3.2 Other Parameters

Additional simulations have been performed to assess the significance of parameters other than the magnitudes of the applied fields. In case G of Table 5.1, the viscosity has been reduced by a factor of four from the value used for all other simulations (the standard value is unity). In all other respects, case G is the same as case E, and it is clear that the viscosity is small enough that it has little impact on the results. Case H is the only exception to the flat resistivity prescript. The normalized profile is $\left(1+r^2\right)^2$, and the effect is substantial. The large resistivity at the wall inhibits the formation of an unstable current profile, so the dynamo is not observed at the voltage level applied.

The distribution of the vacuum poloidal field over the surface of the cylinder has also been considered. Case I is the exception to the vacuum magnetic field configuration that is illustrated in Fig. 5.1. For this case the surface distribution of B_r is that from a line of current, parallel to the cylinder axis and located in the plane of zero potential at r=1.3 (outside the cylinder wall). The total poloidal flux passing through the cylinder is equivalent to the B_V=0.0125 cases with the vertical field configuration. The E_V distribution is unchanged. This produces a current profile that is less hollow than case D. The dynamo is relatively weak, but it exhibits the same kind of behavior as it does in the other cases.

Another geometric parameter that affects the relaxation is the aspect ratio. For a given mean field profile, R/a affects the magnitude of the safety factor at all radii, so it determines which modes are resonant. Case J, and another similar simulation with $S=10^4$, have a reduced aspect ratio of R/a=2. The dominant n=1 modes have poloidal mode numbers that are roughly three times larger than in the comparable case C. The linear significance of this can be inferred from Eq. 2.19. For $m\neq 0$, the substitutions, $m \rightarrow 1$ and $k = n/R \rightarrow n/mR$ can be made in all terms except the first

without changing the equation. As the aspect ratio is changed, different modes become resonant, so n/mR remains unchanged. Therefore, only the first term is affected. It may be written as

$$m^2\left(\frac{1}{r^2}+\frac{n^2}{m^2R^2}\right).$$

This term does not depend on the equilibrium configuration, and it is always positive. Decreasing the aspect ratio increases m for the resonant modes, so this term becomes larger. Considering Eq. 2.18, the effect is to increase the positive curvature of the eigenfunctions, which is stabilizing. This is consistent with the Newcomb theorem that shows the |m|=1 modes are the least stable among m≠0, when considering all real k for a given equilibrium (Newcomb, 1960).

In addition, nonlinear coupling between the (m=1, n=0) source of power (the vertical applied fields) and the low m, n=1 modes is inhibited, because modes with m<4 are not resonant. In the simulations with R/a=6, the low m, n=1 modes are enhanced by this nonlinear coupling and thereby generate more dynamo current. [The importance of nonlinear coupling suggests that poloidal coupling from toroidal effects may also play an important role, especially in low aspect ratio cases. Such effects are beyond the scope of this study.]

It is therefore not surprising that the fluctuation level and relaxation are much smaller in case J than in case C. Another simulation with R/a=10 (case K) has been run to determine if the trend continues for aspect ratios larger than the usual R/a=6. The (1,1) mode is resonant in this case, but the poloidal flux amplification is virtually the same as in case C, so increasing R/a does not always produce more relaxation.

A final special case considers the effect of allowing the axial flux in the cylinder to change at a rate determined by an external inductance. In case L, $\langle E_\theta \rangle$ at the wall, which is proportional to a 'gap' voltage for an imaginary conducting shell that is cut in the axial direction, is allowed to be nonzero. Its value varies with the rate of change of poloidal shell current, which is $2\pi R\langle B_Z(r=1)\rangle$. Otherwise, the conditions are again the same as in case C. There results a small amount of paramagnetism (0.6%) from a pinching effect with little impact on the relaxation.

These special cases show that while geometric and resistivity-related effects are important, the general behavior remains consistent with the configuration discussed in Sections 5.2.2 and 5.3.1 (vertical applied fields and flat resistivity profile). I have therefore concentrated on that basic configuration and expect that the applied-field trends in Section 5.3.2 and the S-scaling in Section 5.4 may be generalized to other configurations.

5.4 Lundquist Number Scaling

To investigate the resistivity dependence of the fluctuation level and relaxation, I have performed computations over a limited range of S (2.5×10^3 to 2×10^4). This range is close to contemporary experiments (e.g. in HIT, S~10^5), but it is far from reactor conditions, so scaling information is relevant. Computations at larger S are possible, but temporal and spatial resolution requirements are prohibitive at present. Numerical results from the full nonlinear system are presented in Section 5.4.1. The interpretation of these results is facilitated by quasilinear simulations (Section 5.4.2) and a heuristic scaling (Section 5.4.3).

5.4.1 Nonlinear Computations

The series of simulations that form the S-scan use the parameters of case C in Table 5.1. The applied electric field and the viscosity are given the same values at each S, but the normalization factors scale like η, so the actual values decrease with increasing S. To produce accurate fluctuation levels, full modal resolution ($0 \le m \le 10$, $|n| \le 5$) is used. The results of this scan show that both the relaxation and the magnetic fluctuation level *increase* with S over this range (see Table 5.2). The change in relaxation is evident from the I_z/I_{inj} ratios—the applied fields are the same for all cases. It is also illustrated by the comparison of λ profiles in Fig. 5.13. The spike of current at the wall is reduced and the bump from relaxation is increased as S is increased.

Table 5.2. S-scaling from simulations with $|n| \le 5$ modes resolved. All cases use the usual conditions of vertical applied fields, $E_V=20$, $B_V=0.0125$, and $R/a=6$. Results are averaged over 0.2 τ_r after saturation.

case	S	I_{inj}	I_z	I_z/I_{inj}	flux amp.	rms(b) all n / n≠0
M	2,500	1.86	0.77	0.42	< 1%	2.81% / 0.16%
N	5,000	1.47	0.76	0.51	22%	2.71% / 1.23%
O	10,000	1.37	0.79	0.58	33%	2.50% / 1.33%
P	20,000	1.26	0.79	0.63	42%	2.39% / 1.39%

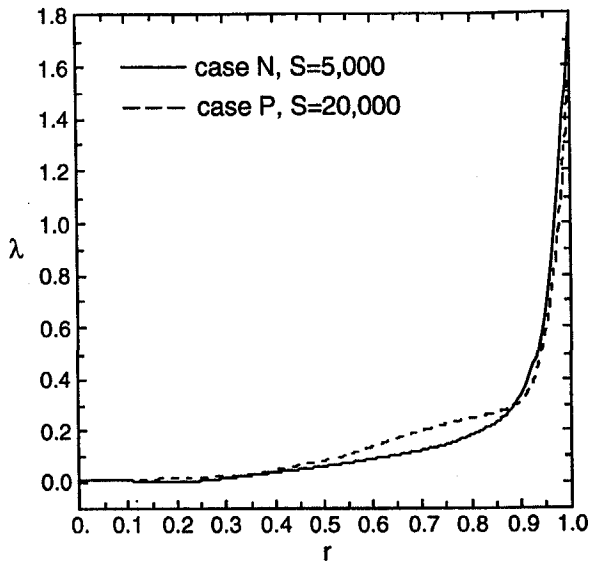

Figure 5.13. λ profiles from fully resolved simulations with different S. Each profile is a time average over approximately 0.2 τ_r. This comparison shows that relaxation increases with S.

These simulations also show the significance of the $|n|>1$ modes. The flux amplification is smaller in case N than it is in case C of Table 5.1, where these modes are not resolved. For the fully resolved cases, some fraction of the power sustains a nonlinear cascade to $n>1$ modes. These modes generate dynamo activity, like the $n=1$ modes, but they tend to produce a larger ohmic dissipation rate. In addition, the cases with $|n|>1$ modes do not settle into a true steady-state. The resonant modes fluctuate on a time-scale between the Alfven time and the

diffusion time, and quasi-steady conditions are sustained after relaxation. The information in Table 5.2 is therefore averaged over a period that is long in comparison with the temporal fluctuations.

5.4.2 Quasilinear Computations

A set of computations without nonlinear interactions has been completed to examine the resistivity dependence resulting from the quasilinear (self-interaction) terms alone. These cases have been run with a modified version of DEBS that solves Eqs. 3.5-3.8. The simulations have S ranging from 5×10^3 to 2×10^4, and other parameters are the same as those used for the nonlinear S-scan. The results in Table 5.3 show that the trends of increasing fluctuation level and relaxation are similar to those produced by the full nonlinear simulations. However, there are only three significant Fourier modes: the mean field, the (1,0) applied vertical field, and one resonant n=1 mode. The final state is free of temporal fluctuations.

Table 5.3. Results of the quasilinear cases. The parameters are the same as those used for the S-scan, but only $0\le m\le5$ and $|n|\le1$ modes are resolved.

case	S	I_{inj}	I_z	I_z/I_{inj}	flux amp.	rms(b) all n / n≠0
R	5,000	1.64	0.77	0.47	<< 1%	3.21% / 0.66%
T	10,000	1.58	0.78	0.49	1.2%	3.06% / 0.94%
U	20,000	1.40	0.77	0.55	9.1%	3.03% / 1.55%

In the absence of nonlinear coupling, the resistivity dependence may be interpreted through a simple power balance for the n=1 mode. The radial Poynting flux from this mode vanishes at the wall, so Poynting's theorem gives $\int(\mathbf{e}_{n=1}\cdot\mathbf{j}^*_{n=1}+\text{c.c.})d\mathbf{x}=0$ in steady state. The mean flow is small, so the quasilinear electric field from Eq. 3.6 reduces to $-\mathbf{v}_{n=1}\times<\mathbf{B}>+\eta\mathbf{j}_{n=1}$. [At this point, it is convenient to use MKS units, so 'S' is dropped and η is not normalized.] Then, a quasilinear force balance, $\mathbf{j}^*_{n=1}\times<\mathbf{B}>\equiv-<\mathbf{J}>\times\mathbf{b}^*_{n=1}$, is applied to produce

$$\int_{r_s}^{a}\mathbf{E}_f\cdot<\mathbf{J}>\mathrm{rdr}\cong\int_{r_s-\varepsilon}^{r_s+\varepsilon}\eta j^2\mathrm{rdr}-\int_{0}^{r_s}\mathbf{E}_f\cdot<\mathbf{J}>\mathrm{rdr}, \tag{5.1}$$

where $\mathbf{E}_f=-\mathbf{v}_{n=1}\times\mathbf{b}^*_{n=1}+\text{c.c.}$ Ohmic dissipation is significant within the resistive layer ($r_s+\varepsilon<r<r_s-\varepsilon$), and the resonance surface ($r=r_s$) is used to divide the dynamo into two parts. For $r>r_s$, $\mathbf{E}_f$ absorbs power from the mean current—which is sustained by the applied n=0 fields, so the left side represents power input for the mode. For $r<r_s$, the second term on the right side represents power transfer to the current in the interior. This is similar to the situation shown in Fig. 5.7a, where several modes contribute to the $\mathbf{E}_f\cdot<\mathbf{J}>$ distribution. The quasilinear simulations show that when η is reduced (S is increased), the ohmic loss becomes a smaller fraction of the input power. The mode saturates at a larger level, with a larger dynamo current drive, so the relaxation is enhanced.

A comparison of the nonlinear simulations in Table 5.2 with the quasilinear simulations in Table 5.3 shows that nonlinear effects are important. The nonlinear simulations produce much more poloidal flux amplification, though the fluctuation levels are not necessarily larger. Nonetheless, the quasilinear terms provide the resonant modes with most of their input power, and the current profile flattening

results from quasilinear terms. I therefore expect that the quasilinear scaling is driving the full nonlinear scaling in this range of S.

5.4.3 Heuristic Scaling

Equation 5.1 may be converted into a heuristic scaling for the quasilinear fluctuation level. This serves two purposes. First, it illustrates the different resistivity dependencies of the terms in Eq. 5.1, which lead to the scaling of the fluctuation level and dynamo-driven current. Second, it may be used to extrapolate results beyond the range of S that has been simulated.

Upon saturation, the radial profiles of the perturbed velocity and magnetic field remain close to their linear forms, the eigenfunctions discussed in Section 2.2. Furthermore, the eigenfunctions are independent of resistivity. I therefore assume that changes in the radial profiles are not significant in the outer region integrals in Eq. 5.1, and take

$$\mathbf{b}_{n=1} = b(\eta)\bar{\mathbf{b}}(r) \text{ and } \mathbf{v}_{n=1} = v(\eta)\bar{\mathbf{v}}(r) ,$$

where $\bar{\mathbf{b}}(r)$ and $\bar{\mathbf{v}}(r)$ are the fixed vector profiles.

In the same spirit, J_o and J_i represent the mean axial current density outside and inside r_s, respectively. The former is essentially fixed by the applied fields, but the latter is sustained by the dynamo electric field, $\eta J_i \sim vb$. The magnitudes v and b are related through Faraday's law in the ideal regions, and

$$\frac{\partial \mathbf{b}}{\partial t} = \nabla \times (\mathbf{v} \times \langle \mathbf{B} \rangle) \text{ becomes } \gamma b \sim v$$

using a linear growth rate. As discussed in Section 2.2, the growth rate scales as a fractional power of resistivity, $\gamma \sim \eta^v$, so the dynamo electric field is proportional to $\eta^v b^2$. Ohmic loss for the mode, the first term on the right side of Eq. 5.1, is proportional to $\varepsilon(\eta j^2)$, where $j \sim b/\varepsilon$ from Faraday's law. For this range of S, I use the resistive skin depth as the width of the tearing layer, $\varepsilon \sim (\eta/\gamma)^{1/2}$. Incorporating these simplifications and scalings in Eq. 5.1 produces

$$C\eta^v b^2 = D\eta^{(v+1)/2} b^2 + \eta^{2v-1} b^4 , \tag{5.2}$$

where C and D are positive constants.

The simplified power balance, Eq. 5.2, can be rearranged into a relation for the fluctuation level as a function of S,

$$b^2 \sim CS^{-(1-v)} - DS^{-3(1-v)/2} . \tag{5.3}$$

The domain of S, which is proportional to η^{-1}, has a lower bound so that $b^2 > 0$. This restriction represents the point where the plasma is so diffusive that tearing modes do not exist. At low S, the fluctuation level increases with S, which is consistent with the simulation results. At high S, Eq. 5.3 suggests that the ohmic contribution, the second term on the right, becomes negligible and that the fluctuation level *decreases* with increasing S. Since J_i is proportional to $b^2 S^{1-v}$,

$$J_i \sim C - DS^{-(1-v)/2} , \tag{5.4}$$

which is a monotonic, increasing function of S. This is also consistent with the increasing relaxation observed in the simulations.

If the important nonlinear effects are ignored, the heuristic scaling predicts a scenario that is more favorable at high S than at low S, where the simulations have been run. However, the increasing relaxation represented by Eq. 5.4 is only weakly dependent on S, and there is an asymptotic limit. It is therefore unlikely that the current profile will relax to anything close to the Taylor state or anything close to a tokamak.

References

B. Coppi, J. M. Greene, and J. L. Johnson, "Resistive Instabilities in a Diffuse Linear Pinch," Nucl. Fusion **6**, 101 (1966).

D. S. Darrow, M. Ono, C. B. Forest, G. J. Greene, Y. S. Hwang, H. K. Park, R. J. Taylor, P. A. Pribyl, J. D. Evans, K. F. Lai, and J. R. Liberati, "Properties of DC Helicity Injected Tokamak Plasmas," Phys. Fluids B **2**, 1415 (1990).

T. R. Jarboe, "Review of Spheromak Research," Plasma Phys. Control. Fusion **36**, 945 (1994).

T. R. Jarboe, "Formation and Steady-state Sustainment of a Tokamak by Coaxial Helicity Injection," Fusion Tech. **15**, 7 (1988).

T. H. Jensen and M. S. Chu, "Current Drive and Helicity Injection," Phys. Fluids **27**, 2881 (1984).

B. A. Nelson, T. R. Jarboe, D. J. Orvis, L. A. McCullough, J. Xie, C. Zhang, and L. Zhou, "Formation and Sustainment of a 150 kA Tokamak by Coaxial Helicity Injection," Phys. Rev. Lett. **72**, 3666 (1994).

W. A. Newcomb, "Hydromagnetic Stability of a Diffuse Linear Pinch," Ann. Phys. **10**, 232 (1960).

M. Ono, G. J. Greene, D. Darrow, C. Forest, H. Park, and T. H. Stix, "Steady-state Tokamak Discharge via DC Helicity Injection," Phys. Rev. Lett. **59**, 2165 (1987).

J. B. Taylor, "Relaxation of Toroidal Plasma and Generation of Reverse Magnetic Fields," Phys. Rev. Lett. **33**, 1139 (1974).

6. SUMMARY AND CONCLUSIONS

In this dissertation, I have reported on a number of topics that are important for understanding and improving the RFP configuration. The concept of using DC helicity injection as a sole means of sustaining the tokamak has also been investigated. Most of the results have been obtained with the nonlinear, three-dimensional DEBS code (Schnack, 1987) that solves the MHD equations for initial value problems in the geometry of a periodic cylinder. Information regarding the linear stability properties of RFP configurations with auxiliary current drive has been determined with a new code, RESTER. It uses Robinson's approach for solving the eigenvalue problem posed by the analytic theory of resistive tearing modes (Robinson, 1978).

To facilitate the computation of RFPs at large Lundquist number, I have developed and implemented hyper-dissipation terms in the pressureless version of DEBS. The damping from these terms is proportional to the fourth power of wavenumber, and it can be used to suppress scale lengths that are not physically important to the global results. This allows a reduction of radial resolution, which reduces the CPU time and memory requirements for a set of physical parameters. I have found that the radial resolution may be halved, relative to normal DEBS simulations, while retaining fluctuation level accuracy to within 3%.

For finite-pressure simulations, the anisotropic thermal conduction algorithm has been improved with the implementation of a new semi-implicit operator. Computing thermal conduction in MHD simulations of high temperature plasmas is challenging, because the time-scale for parallel conduction is much smaller than the time-scale of MHD activity, and the anisotropy makes standard implicit methods impractical. The new semi-implicit algorithm has several attractive features. It is numerically stable for time steps that are orders of magnitude larger than the

explicit stability limit, and it accurately conducts heat along magnetic field lines without inducing artificial perpendicular conduction. In addition, the DEBS implementation requires only 30% more CPU time than finite-pressure simulations run without thermal conduction.

Nonlinear simulation results from basic RFP configurations address power flow through the system, including electromagnetic and thermal energy transport associated with the MHD fluctuations. The electromagnetic energy transport is an average Poynting flux that is induced by fluctuating electric and magnetic fields, and it reflects approximately 10% of the power delivered by the inductive electric field. It is an inherent part of the MHD dynamo and connects the plasma interior, where the mean current loses power to the fluctuations, with the exterior, where it gains power from them.

Most of the power drives mean current directly and becomes thermal energy via ohmic dissipation. Simulations with finite pressure and anisotropic thermal conduction show that the MHD fluctuations allow radial transport through the correlation of fluctuating parallel heat flow and the radial component of magnetic perturbations, $\langle q_{(B)} b_r \rangle \langle B \rangle^{-1}$. This is consistent with experimental measurements on MST which show the correlation accounts for energy transport within r/a=0.85 (Fiksel, 1994). The thermal conductivities used in the simulations are not formally valid in the stochastic RFP magnetic field, and the effective thermal diffusivity over-predicts the appropriate analytic relation for test particle diffusion (Rechester, 1978). However, the simulated transport has the proper dependence on the magnetic fluctuation level, so the model is useful for making relative predictions of confinement under different conditions.

The significance of plasma pressure for sustaining fluctuations is also assessed with the simulations. I have compared the powers, $S(\beta_0/2)\int \langle \mathbf{v} \cdot \nabla p \rangle d\mathbf{x}$ and

$\int \mathbf{E}_f \cdot \langle \mathbf{J} \rangle d\mathbf{x}$, which represent the pressure-gradient drive and the current-gradient drive, respectively. The powers sustaining different azimuthal mode numbers are separated, and for the m=1 modes, the current-gradient drive dominates as expected. However, the m=0 modes do not allow a significant amount of transport in the simulations, so there is a large pressure gradient at their resonance surface. The two powers are equally important in sustaining these modes.

A Lundquist number scaling over a limited range of S has also been completed using the hyper-dissipation terms in the pressureless system. The result is the weak dependence, $rms(b) \sim S^{-.18}$, but the dependence may be stronger in the large-S limit. In the range investigated, $2.5 \times 10^3 \leq S \leq 4 \times 10^4$, the linear modes are only approaching their asymptotic behavior (Li, 1995), and the m=0 energies increase with S. Based on changes in the parallel current profile, I expect the m=0 modes will decrease with S at larger values, which will strengthen the total scaling. Another numerical study conducted with a different code predicts a slightly stronger dependence of $S^{-.22}$ (Cappello, 1993), so the two investigations yield approximately the same result.

The S-scan run with DEBS also shows the emergence of periodic 'sawteeth' from pressureless MHD activity. That oscillations become more regular with increasing S has been previously observed (Cappello, 1994), but here the effect is more dramatic. The m=0 modes play an important role in organizing the temporal behavior. They are small until nonlinearly driven to a large amplitude by internally resonant m=1 modes. Coupling that aids the dynamo drive of poloidal current is restricted until the m=0 modes are large, then stored fluctuation energy is suddenly released in the form of reversed magnetic field, which suppresses the modes and restarts the cycle.

Although RFP fluctuations provide valuable insight into tearing modes, fluctuation-induced transport and MHD turbulence, they are harmful to energy confinement. DC helicity injection (Ho, 1991) and RF current drive (Shiina, and Uchimoto, 1994) have been previously proposed as means of modifying the parallel current profile to reduce the fluctuations. I have examined these ideas with linear and nonlinear calculations. To model the RF approach and examine a generic form of helicity injection, the MHD equations are modified to include an auxiliary drive mechanism. A linear parameter study shows that a balance between the applied axial electric field and the auxiliary drive is necessary to stabilize internally resonant modes. Current profile modification is most effective when current near the axis is reduced by using a smaller axial electric field in addition to applying the auxiliary drive at large radii. This distributes the resonance surfaces of the stabilized modes across most of the radial domain, so a large fraction of the discharge is relatively free of fluctuations.

Nonlinear simulations with auxiliary current drive confirm the implications of the linear calculations. When the largest, internally resonant modes are predicted to be linearly stable, the nonlinear simulations show a large reduction in fluctuation level. The internal modes remain in existence due to nonlinear coupling from exterior modes, but their energies are typically smaller by two orders of magnitude. However, when the largest modes resonant near the origin are not stabilized, nonlinear coupling sustains the stabilized modes at a significant level. In the cases where the internal modes are substantially reduced, the saturation level of destabilized exterior modes is no larger than in the normal RFP configurations. These modes are normally stable and are driven by nonlinear coupling with the internal modes. With profile modification, the quasi-linear drive is increased, but nonlinear coupling is reduced.

With finite pressure and thermal conduction, the simulations provide quantitative information on energy confinement improvement resulting from auxiliary drive. An R/a=1.25 simulation shows that the effective thermal diffusivity at some interior location is reduced proportionately with the energy in the locally resonant fluctuations. In this case, χ_e is reduced by two orders of magnitude in the center of the radial domain. The temperature on axis increases, and the energy confinement time triples. The auxiliary drive supplies a substantial fraction of the total power and deposits it near the wall. This power is not well confined in the simulation and prevents a more dramatic improvement in total confinement. Though the interior transport is greatly reduced, it is still dominated by the same fluctuation-induced conduction. With the reduction in the current-gradient drive and the increased central temperature, the pressure-gradient drive becomes equally important for sustaining the internally resonant modes.

DC helicity injection simulations extend the earlier investigation to larger aspect ratios and Lundquist numbers, where nonlinear interactions are more important. I have found that the axisymmetric configuration is no less effective, but when electrodes have toroidal separation, nonlinear coupling with internally resonant modes can negate the stabilizing influence of the current profile modification. A compromise between the stability of the axisymmetric geometry and the practicality of the local configuration led to a segmented version of the axisymmetric system. When the number of electrodes is large, this configuration avoids harmful nonlinear coupling and successfully reduces interior modes by two orders of magnitude in an R/a=3, $S=10^4$ simulation.

The last form of current profile modification examined is the transient PPCD technique developed on MST (Sarff, 1994). This is not a form of helicity injection, so the additional current is not sustained, but it does reduce the fluctuations as it

propagates inward. The reduction results from changes in the dynamo power density, similar to changes induced with the other current drive schemes. The behavior of the magnetic fluctuations in simulation and experiment compare very well. Therefore, the increased confinement time observed in PPCD experiments on MST provides proof that RFP confinement can be improved through current profile modification.

The numerical study of sustaining tokamak configurations with DC helicity injection alone is the first detailed theoretical study of this concept. The geometry is greatly simplified, and other factors such as the resistivity profile are not optimized. However, the simple configuration modeled with DEBS reproduces the fundamental MHD aspects of injection and relaxation. The results show the two important features of 1) sustained axial (toroidal) current without 'loop' voltage and 2) poloidal flux amplification. Relaxation occurs through an MHD dynamo that is similar to the RFP dynamo, but in this case the electromagnetic energy transport is inward. The dynamo suppresses edge current driven by the injection and sustains interior current that generates closed poloidal flux contours. However, the relaxation is weak relative to what is observed in RFPs due to the stabilizing influence of the large axial magnetic field. In addition, the magnetic fluctuation level is large enough to make the magnetic field stochastic in the region where the relaxation occurs. A Lundquist number scaling shows that relaxation and the fluctuation level increase with S in the range considered, $2.5\times10^3 \le S \le 2\times10^4$. A heuristic scaling is consistent with both of these properties at small values of S, and at large S, it predicts that the fluctuation level decreases with S while the dynamo-driven current approaches an asymptotic limit.

For all of the different configurations, the MHD model represents a driven-damped system. I have considered times that are at least as long as the total

energy turnover time, and there is significant dissipation on all scale lengths, so relaxation arguments are not appropriate. The helicity rate balance is valid, and it is a necessary condition for maintaining steady-state. However, the simulations show that providing the required amount helicity is not sufficient for producing a desirable configuration. Localized DC injection systems in RFPs can provide plenty of helicity. Though a large fraction of the associated power sustains mean current, some sustains the MHD fluctuations directly. Similarly, different parameter sets for tokamak injection can produce the same rate of helicity injection, yet the resulting configurations are different. These results are not surprising, because different results can be produced by the same amount of inductive helicity injection from applied loop voltage. Therefore, helicity rate balance should not be used to predict results of a configuration without additional analysis.

The optimum modification in the RFP is actually a redistribution of helicity dissipation. Configurations with stable interiors result from reduced inductive helicity injection—to drive less current near the axis—in conjunction with noninductive injection at large radii. This eliminates the primary source of fluctuation power that is normally present in RFPs, and the result is improved energy confinement. The interior becomes similar to that of a stable paramagnetic equilibrium, and reversal is sustained by noninductive injection. I expect that the reversal will continue to be an important feature of these configurations. Though the fluctuations are largely driven by the pressure gradient, nonlinear coupling with resonant m=0 modes will help prevent disruption, as in ordinary RFPs.

RFP experiments may realize greater improvement in confinement time than the MHD result discussed in Section 4.2.2. The simulation starts at a relatively large value of β_p, so the pressure-gradient drive of fluctuations quickly becomes important. Also, the finite pressure simulations have relatively low temperatures,

and perpendicular conduction readily transports heat near the wall. This will not be so important in experiments, because the edge temperature is much hotter. In addition, current driven by RF waves and realistic DC injection is carried by fast electrons. They are relatively free of collisions, so the power required from the injection system in the simulations represents an upper bound. The total energy confinement improvement may therefore be closer to what has been observed in the interior of the simulation, which is nearly an order of magnitude.

The tokamak helicity injection simulations are not so encouraging. Although key features of the concept are verified, the amount of relaxation is insufficient to produce anything but very hollow discharges. Several parameters have not been optimized, and better parallel current profiles may be possible. However, the results do reflect the extent of topological change that can be expected from resistive MHD activity. In addition, the fluctuation level is large enough to make the magnetic field stochastic, so the system would suffer from parallel transport mechanisms like normal RFPs. Therefore, it is unlikely that DC helicity injection can sustain tokamak configurations with good confinement properties.

References

S. Cappello and D. Biskamp, "MHD studies of Stationary Turbulent Dynamics in a Reversed-field Pinch," in *Proceedings of the 20th European Physical Society Conference on Controlled Fusion and Plasma Physics,* Lisbon, II-487 (1993).

S. Cappello and D. Biskamp, "MHD studies of Stationary Turbulent Dynamics in a Reversed-field Pinch," in *Proceedings of the 1994 International Conference on Plasma Physics,* Foz do Iguacu, 149 (1994).

G. Fiksel, S. C. Prager, W. Shen, and M. Stoneking, "Measurement of Magnetic Fluctuation Induced Energy Transport," Phys. Rev. Lett. **72**, 1028 (1994).

J. M. Finn and W. M. Manheimer, "Spheromak Tilting Instability in Cylindrical Geometry," Phys. Fluids **24**, 1336 (1981).

Y. L. Ho, "Numerical Simulation of Fluctuation Suppression via DC Helicity Injection in a Reversed-field Pinch," Nucl. Fusion **31**, 341 (1991).

J. Li and D. Liu, "Tearing Mode in RFP Configurations," Alfven Laboratory Report ISSN 1102-2051, Stockholm, Sweden (1995).

A. B. Rechester and M. N. Rosenbluth, "Electron Heat Transport in a Tokamak with Destroyed Magnetic Surfaces," Phys. Rev. Lett. **40**, 38 (1978).

D. C. Robinson, "Tearing-mode-stable Diffuse-pinch Configurations," Nucl. Fusion **18**, 939 (1978).

J. Sarff, S. A. Hokin, H. Ji, S. C. Prager, and C. R. Sovinec, "Fluctuation and Transport Reduction in a Reversed Field Pinch by Inductive Poloidal Current Drive," Phys. Rev. Lett. **72**, 3670 (1994).

D. D. Schnack, D. C. Barnes, Z. Mikic, D. S. Harned, and E. J. Caramana, "Semi-implicit Magnetohydrodynamic Calculations," J. Comput. Phys. **70**, 330 (1987).

S. Shiina, K. Saito, Y. Kondoh, H. Ishii, T. Shimada, Y. Hirano, "Current Density Profile Control in Reversed Field Pinch Plasma by RF Current Drive," in *Proceedings of the 19th European Physical Society Conference on Controlled Fusion and Plasma Physics,* II-917, (Innsbruck, 1992).

E. Uchimoto, M. Cekic, R. W. Harvey, C. Litwin, S. C. Prager, J. S. Sarff, and C. R. Sovinec, "Lower-hybrid Poloidal Current Drive for Fluctuation Reduction in a Reversed-field Pinch," Phys. Plasmas **1**, 3517 (1994).

EXTERNAL DISTRIBUTION IN ADDITION TO UC-20

S.N. Rasband, Brigham Young University
R.A. Moyer, General Atomics
J.B. Taylor, Institute for Fusion Studies, The University of Texas at Austin
E. Uchimoto, University of Montana
F.W. Perkins, PPPL
O. Ishihara, Texas Technical University
M.A. Abdou, University of California, Los Angeles
R.W. Conn, University of California, Los Angeles
P.E. Vandenplas, Association Euratom-Etat Belge, Belgium
Centro Brasileiro de Pesquisas Firicas, Brazil
P. Sakanaka, Institute de Fisica-Unicamp, Brazil
Mme. Monique Bex, GANIL, France
J. Radet, CEN/CADARACHE, France
University of Ioannina, Greece
R. Andreani, Associazione EURATOM-ENEA sulla Fusione, Italy
Biblioteca, Istituto Gas Ionizzati, EURATON-ENEA-CNR Association, Italy
Plasma section, Energy Fundamentals Division Electrotechnical Laboratory, Japan
Y. Kondoh, Gunma University, Kiryu, Gunma, Japan
H. Toyama, University of Tokyo, Japan
Z. Yoshida. University of Tokyo, Japan
FOM-Instituut voor Plasmafysica "Rijnhuizen," The Netherlands
Z. Ning, Academia Sinica, Peoples Republic of China
P. Yang, Shandong University, Peoples Republic of China
S. Zhu, University of Science & Technology of China, People's Republic of China
I.N. Bogatu, Institute of Atomic Physics, Romania
M.J. Alport, University of Natal, Durban, South Africa
R. Storer, The Flinders University of South Australia, South Australia
B. Lehnert, Royal Institute of Technology, Sweden
Librarian, CRPP, Ecole Polytechnique Federale de Lausanne, Switzerland
B. Alper, Culham Laboratory, UK
A. Newton, UK

2 for Chicago Operations Office
5 for individuals in Washington Offices

INTERNAL DISTRIBUTION IN ADDITION TO UC-20
80 for local group and file